PHAROS: *P*luri-detector, *H*igh-resolution, *A*nalyser of *R*adiometric properties *O*f *S*oil cores

by

Richard Pitout

Submitted in the fulfilment of the academic
requirements for the degree of
Master of Science in the
School of Pure & Applied Physics,
University of Natal,
Durban

December 2001

For my father – who still encourages me every day.

Abstract

The core-logger has been designed for the high-resolution radiometric analysis of soil cores using multiple detectors. This device allows for the automation of the measuring process and eliminates the need to dissect the cores. The design is aimed at measuring soil-cores with a 10cm radius and a length of 1m and allows for up to 4 detectors to be mounted on the measuring platform. Currently a combination of Bismuth-Germanate (BGO) and Caesium-Iodide (CsI) detectors are used.

The core logger required a good spatial resolution of ~1cm. This has been difficult to obtain and has required extensive investigation. The shielding configurations were varied and the effect of background radiation was looked at in detail to determine an optimal construction. A secondary objective has been the complete measurement of a single core in 24 hours. This has also been difficult to achieve because the low activity of natural radiation in the core samples needs longer measuring times. The BGO detectors were used as a more efficient detector (than, e.g. CsI) which helped to reduce the required measuring time.

Measured spectra have been analysed to determine the activity concentrations of the specific radionuclides of interest: ^{232}Th, ^{238}U, ^{40}K and ^{137}Cs. These activity profiles of the measured cores provide information that can then be used to radiometrically fingerprint the sample to determine soil characteristics such as grain size and mineral content. However, because the actual resolution of the system (~3cm) is greater than the typical core slice (~2cm), the radiometric information in a specific core-slice contains contributions from its adjacent slices. This folding or convolution of the measured spectra can be undone using a deconvolution method, which was examined and commented on.

Preface

The work described in this dissertation was carried out in the Nuclear Geophysics Group, Kernfysisch Versneller Instituut, Rijksuniversiteit Groningen, the Netherlands from May 1999 to June 2000 under the supervision of Dr RJ de Meijer; and in the Applied Physics Group, School of Pure & Applied Physics, University of Natal, Durban from August 2000 to December 2001 under the supervision of Professor MJ Alport.

These studies represent the original work of the author and have not otherwise been submitted in any form for any degree or diploma to any tertiary institution. Where use was made of the work of others it has been duly acknowledged in the text.

Table of Contents

Foreword

The research in this project was commissioned by Rijkwaterstaat National Institute for Inland Water Management and Waste Water Treatment (RIZA) under contract RIZA RI 2784, project co-ordinator ir M. van Wijngaarden.

The Nuclear Geophysics Division of the Kernfysisch Versneller Instituut, Rijksuniversiteit Groningen (NGD/KVI) focuses on the development of nuclear physics based techniques and methods for application in other sciences, industry and society. The emphasis of these techniques is directed towards applications in Earth Sciences. In the last decade a highly sensitive gamma-ray detector system, MEDUSA, was developed for high resolution surveys of underwater bottoms of rivers, estuaries and coasts. In recent years a methodology was developed that enables the characterisation of sediment by the concentration of (natural) radionuclides (radiometric fingerprinting). This development has lead to the successful mapping of sediment, not only underwater but also on land. Moreover the high sensitivity allows application in bore holes with a much higher resolution than previously feasible.

In this project the MEDUSA methodology was applied to a new field: analysis of soil-core samples. Presently systems analysing drill cores usually have a resolution of about 10 to 15 cm. Higher resolution would mean a considerable reduction in count rate and hence much longer measuring times. In certain fields of sedimentology, (sub)-centimetre resolution is desirable. One of the applications requiring such resolution is the determination of sedimentation rates which are of the order of millimetres per year and where effects to be studied are on a time scale of decades.

On request by RIZA, the "fresh-water" branch of Rijkswaterstaat in the Netherlands, NGD/KVI designed a high-resolution, radiometric core analyser. The analyser has an initial resolution of about 2cm and has the possibility of being equipped with four MEDUSA-type detector systems, although it currently has two MEDUSA type detector systems and one separate Caesium Iodide system. At the beginning of 1999 the required equipment was ordered and the work started on 1 May, 1999. The first

part of the project consisted of designing and assembling the set-up, including testing and examining detectors. From August until November 1999 the set-up was calibrated in terms of efficiency and edge effects with a detailed examination of the minimum achievable spatial resolution. This was done using ideal point-like sources and the Caesium Iodide detector system. Having completed the initial analysis, between November 1999 and February 2000 the assessment was extended to include the two MEDUSA-type detectors. Testing these detectors required the adaptation of existing MEDUSA software, as well as the construction of test cores with known activity concentrations. The test cores were measured and standard spectra were constructed, which could then be used in the measurement of real data. After the analysis and assessment of the test data, the first series of measurements were due to begin in June 2000. Immediately prior to this the first unknown field cores were analysed in terms of sediment composition and sedimentation rates. It was hoped that the sedimentation rates could be deduced from episodic events of ^{137}Cs like the atmospheric bomb tests, Chernobyl and the continuous regular releases of ^{137}Cs and ^{60}Co by the nuclear power stations along the rivers Rhine in Germany and Meuse in France and Belgium.

This project has therefore been a mixture of engineering, computer sciences and nuclear physics. It involved a close collaboration with the earth scientist who was waiting to use the new instrument. It used partly known technologies which were extended in a new direction.

The project was undertaken in the context of an MSc degree in The School of Pure & Applied Physics at the University of Natal, Durban campus, and required a degree of independent work in engineering, nuclear physics and computer science.

Chapter 1 :
Introduction

The work on PHAROS was undertaken in the context of a BSc (MSc) degree in the School of Pure & Applied Physics at the University of Natal, Durban, South Africa, under the supervision of Prof. Mike Alport. The project required development and research time to be spent at the Kernfysisch Versneller Instituut (KVI) at the Rijksuniversiteit van Groningen as a part of the Nuclear Geophysics Division (NGD), under the supervision of Dr RJ de Meijer. As an independent project at the KVI, the development required a periodic submission of progress reports. It must be noted here that these reports form the bulk of the individual chapters in this document and their chronology is reflected in the chapter ordering. The scope of the MSc will cover initial design and prototyping of PHAROS, as well as an investigation of the analysis techniques.

The core-logger is designed as a multiple detector system capable of analysing soil-cores with a high-resolution and within a short time. The logger will integrate several components. It needs a mechanical feed that allows the sample to be loaded and moved; a detector array for scanning the sample for gamma radiation; and software for driving the mechanics, data capture and data analysis.

Typically soil-cores are housed in PVC tubing 1m in length with a diameter of 10cm. The system measures the radionuclide content of the sample using gamma-detection techniques. The radionuclides of primary interest being ^{232}Th, ^{238}U, ^{40}K and ^{137}Cs. This concentration information is then used in radiometric fingerprinting to determine soil characteristics such as grain size and mineral content. The system has application in several fields, a good example being the examination of sedimentation rates. Traditionally these profiling measurements were undertaken by hand, requiring the cores to be sliced into 1cm segments with each one measured separately. The aim of PHAROS is to automate this process, providing a similar spatial resolution of ~1cm and decreasing the measurement time per core.

The development progress is described in stages. Chapter 2 looks at the initial design stages and set-up decisions. A shielding arrangement was constructed and various slit configurations were investigated using a point-like ^{137}Cs source and a Caesium-Iodide (CsI) detector. This also led to a preliminary investigation of the background contribution to the signal and an indication as to an achievable resolution.

Chapter 3 looks at the advancement of the mechanical design and implementation. The different components of the system are considered in terms of feasibility and efficiency. Problem areas identified are the movement of the core through the system and the stability of the software controlling the components.

Chapter 4 introduces the multiple detector configuration. The addition of two Bismuth-Germanate (BGO) detectors introduced calibration difficulties and required a more detailed examination of the composition of the background contribution. Analysis techniques are compared and a more detailed description of the Full-Spectrum Analysis (FSA) is given. This includes an examination of the calibration (or standard) cores and standard spectra. Finally, the system is tested on unknown cores and a comparison is made with real data.

Chapter 5 comprises an investigation into refining the analysis techniques by including deconvolution (or unfolding) of the measured signals. A soil-core can be thought of as a distribution of point-sources. Each point-source contributes separately to the measured signal. Ideally this signal can then be unfolded to determine the exact contribution of each point individually. Chapter 5 is therefore a brief investigation of a simple model and establishes a proof-of-principle. The investigation excludes detailed examination of error-corrections and more complex models that would include energy dependence.

Chapter 2 :

Tests of lead-shielding and collimation for PHAROS.

2.1 Introduction

After an initial planning stage it was necessary to construct the prototype core-logger. For the construction to be completed successfully, the function of the core-logger needed to be well understood, and this included the operation of all the components. This chapter focuses on one of those components – the Caesium-Iodide (CsI) detector. It must be noted that this was not the only detector considered for the system and the optimal configuration would possibly require a Bismuth Germanium (BGO) detector. This chapter will focus on the CsI, and subsequent chapters will look at different systems.

This chapter outlines the study of the detector with respect to its use in the core-logger. It was necessary to test the resolution of the detector, check its calibration and the effect of the lead/slit configuration. This was completed using a simple, point-like source that is well-defined (in the sense that it produces a single well-known photo-peak in the desired energy range). Understanding the behaviour in these 'ideal' conditions helped in the task of interpreting more complex data.

The investigation followed several distinct steps. The first was a preliminary, or qualitative, examination to gain a feel for the system. The detector was used to measure spectra in various configurations, with the resulting data analysis contributing to an understanding of the behaviour of the system and of the nuclear processes in general.

2.1.1 The core-logger frame

The frame was designed to support all the components. It had to be strong enough to hold up to 4 different detectors and their required shielding. It also had to allow for a core to be inserted into the system and passed through the centre of the detector

platform. This required a motor to drive the stepping mechanism and hence a mounting bracket on the frame for the motor. A sketch of the core-logger frame is given in (Figure 2-1).

The top platform of the frame was used to support the detectors, and the core-sample passed through the hole in the centre of the frame, between the detectors on the top level. It was passed in from below the bottom platform and the stepping mechanism pulled the core through the frame past the detectors.

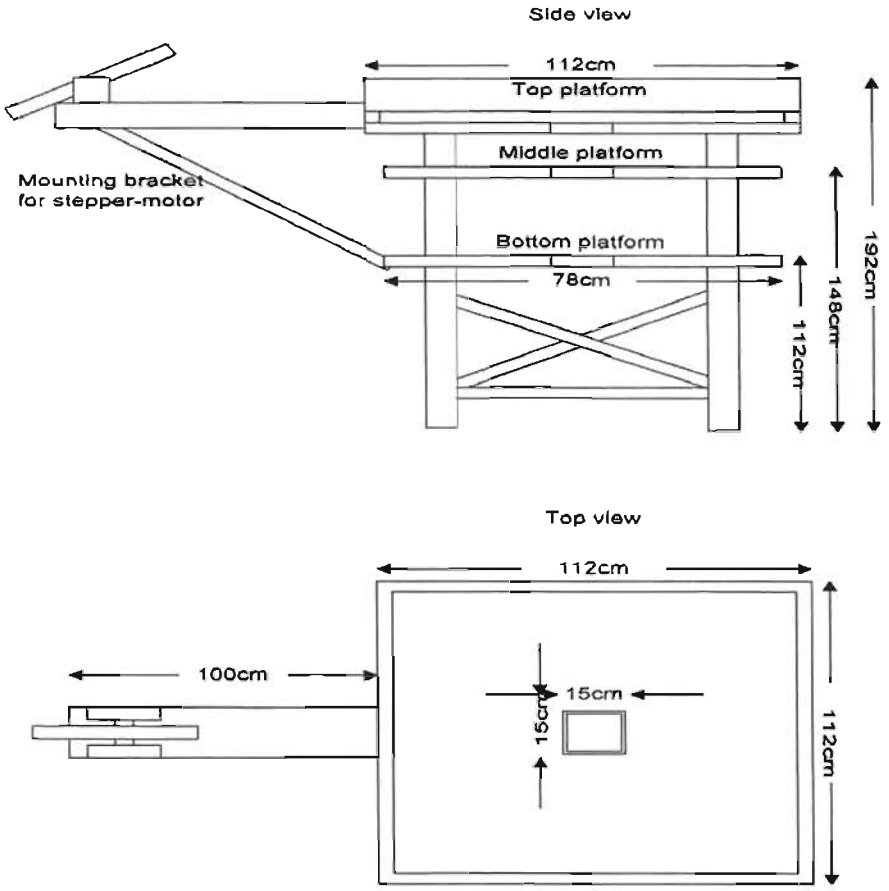

Figure 2-1: Frame design of the core-logger system

2.2 Physics background

A brief review of the physics of radiation and its interactions with matter follows. This information was taken from [7] and [8].

2.2.1 Overview of radiation

Ionising radiation most generally refers to the spontaneous emission of particles and/or energy from excited or unstable nuclei. Nuclei may undergo a variety of processes resulting in radiation emission. These processes can be categorised into two main groups: radioactivity and nuclear reactions. In a nuclear reaction process, a nucleus interacts with one or more other nuclei with subsequent emission of radiation as one of the end products. For a radioactive transformation, a single nucleus may spontaneously disintegrate into a different species of nuclei, or simply to a lower energy level of the same species.

There are two types of radiation: corpuscular and electromagnetic. Corpuscular radiation concerns emissions involving α-particles, β-electrons and positrons, internal conversion electrons, neutrons and protons, amongst others. Electromagnetic radiation emissions consist of *x*-rays and γ-rays. The goal of this project is to examine the γ-radiation emitted from the samples, and therefore all discussions will be limited to electromagnetic radiation only.

γ-Rays are a form of energy known as photons, except they have a much smaller wavelength than light. They have no rest mass and no charge. (Rest mass is defined as the mass of a particle that is not moving.)

Sources of gamma radiation

A common form of γ-ray emission occurs after a β-decay has taken place leaving the daughter nucleus in an excited state, i.e. a state above the state with the lowest energy (ground state). This is an unstable state and the daughter nucleus will then release energy in the form of γ-radiation to move to a lower energy state.

Example of gamma emission

In Figure 2-2 we see the simple decay scheme of a ^{137}Cs nucleus. This is an example of γ emission following a β^- decay. In 6.5% of these decays the ^{137}Cs nucleus undergoes a transition to the ground state of ^{137}Ba. The remaining 93.5% of the time the β^- decay leaves ^{137}Ba in an excited state 0.662MeV above the ground level. This

excited particle will emit its surplus energy through γ emission and ends up in the ground state.

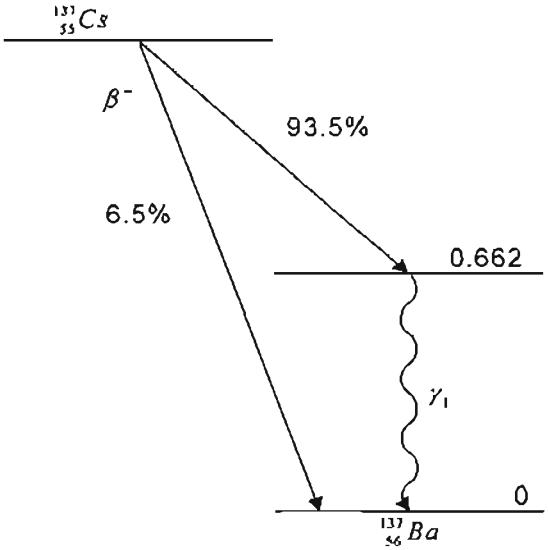

Figure 2-2: Decay scheme of ^{137}Cs.

This represents a typical γ-ray emission following β^- decay, as occurs with most of the common β induced γ sources.

Interactions of gamma radiation

There are 3 primary mechanisms through which γ-rays interact with matter [7].

i. *Photoelectric absorption.*

In this process an incident γ-ray photon undergoes one or more interactions with the absorber atom(s) when all the energy of the γ-ray is transferred into the emission of *photoelectrons*. The emitted photoelectron appears with energy given by $E_{e^-} = h\nu - E_b$ where E_b is the binding energy of the photoelectron in its original shell. This process is enhanced for absorber materials with high Z, and the cross section depends on Z and γ-ray energy as $\sim \frac{Z^n}{E_\gamma^3}$. Here n varies between 4 and 5 over the gamma ray region of interest.

ii. *Compton scattering.*

In Compton scattering the incident γ-ray is not fully absorbed, but collides with a loosely bound electron in the absorber and is deflected by an angle θ with respect to its original direction. In the collision, part of the energy of the γ-ray is

transferred to the electron (assumed to be initially at rest) which then becomes the *recoil electron*. The energy transferred can vary between 0 and a large fraction of the incident γ-ray energy – the actual value depends on the angle of scattering and is given by $E_\gamma - E'_\gamma$ with

$$E'_\gamma = \frac{E_\gamma}{1 + \frac{E_\gamma}{m_0 c^2}(1 - \cos\theta)}. \qquad (2.1)$$

Here E'_γ is the energy of the scattered photon, θ is the scattering angle and m_0c^2 is the rest mass energy of the electron (0.511MeV). The angular distribution is given by the *Klein-Nishina formula* [7] for the differential scattering cross section $d\sigma/d\Omega$

$$\frac{d\sigma}{d\Omega} = r_0^2\left[\frac{1}{1+\alpha(1-\cos\theta)}\right]^3\left[\frac{1+\cos^2\theta}{2}\right]\left[1+\frac{\alpha^2(1-\cos\theta)^2}{(1+\cos^2\theta)[1+\alpha(1-\cos\theta)]}\right], \qquad (2.2)$$

where r_0 is the classical electron radius and $\alpha = E_\gamma/m_0c^2$. The cross section (in m^2kg^{-1}) depends on the electron density and hence on the density ρ of the incident material. Note that per unit mass of the incident material Compton scattering is independent of Z

iii. *Pair production.*

Pair production occurs when the γ-ray photon interacts (typically with the nucleus of an atom) and is replaced by an electron-positron pair. Therefore, in principle the initial γ-ray must have an energy of at least twice the rest mass of a single electron (0.511MeV). In practice it is generally necessary for the γ-ray to have a much higher energy than this. The energy balance is given by $E_\gamma = T_+ + mc^2 + T_- + mc^2$, where T_+ and T_- are the energies of the positron and electron. This interaction must take place in the vicinity of a massive atom in order to conserve momentum, although this recoil energy is negligible in comparison to the other terms. There is no exact formula for the cross section of this interaction, but its magnitude varies approximately as Z^2 of the absorber atom.

Pair production requires energy in excess of 1.02MeV (rest mass of the e^-, e^+ pair) and the cross-section for this process becomes significant for $E_\gamma > 3MeV$. For the present study the natural radiation has $E_\gamma < 3MeV$ and pair production will be ignored in all following discussions. Photoelectric absorption and Compton scattering are the dominant processes in the γ-ray detection at lower energy levels.

2.2.2 Measurement instrumentation

2.2.2.1 Detectors

Detectors in general

This subsection will give a general overview of how detectors function. The goal is to give the reader a basic understanding before considering greater detail.

Consider a *single* incident quantum of radiation. Once the incident radiation enters the detector it undergoes an interaction (which particular interaction is unimportant at this point). This interaction time is very short, and a pulse of electrical charge Q is generated. This charge is collected through the imposition of an electric field – causing a flow of charged particles. The current generated by this flow is collected and can be converted into an electrical pulse. The magnitude and duration of each current pulse varies according to the interaction causing it and gives an indication of the energy of the incident radiation.

Moving away from the simplified model it is necessary to consider some of the complications. First note that although the interaction time and charge collection time may be very small (~ns), they still represent a finite response time where the detector is concerned. In a situation where a high count rate is possible, it is likely that the current flowing in the detector at an instant in time is due to several distinct interactions. This implies that the interactions will be individually indistinguishable and hence that there is a limit to the minimum time by which two interactions should be separated for the detector to correctly identify them. This minimum time is known as the *dead time* of the detector. This dead time is utilised in summing the contributions of the many partial interactions of e.g. photons in the detector material,

resulting in one output pulse. This can be contrasted with the concept of *electronic dead time*, which arises through the inability of the electronic hardware to count every pulse the detector outputs (when the count rate is sufficiently high). Electronic dead time is the dominant contributor and events detected separately by the detector may still be summed by the electronics. A further effect to consider here is that of coincident or cascade summing, in which the nucleus emits two or more gammas within the time resolution of either the detector or the electronics. This effect is always present, even at very low count rates.

Each interaction within the detector will theoretically give rise to an output pulse. *Detector efficiency* is a measure of the *radiation stopping* likelihood (i.e. the probability of the incident radiation interacting within the detector) of the detector. Detector efficiency is subject to several parameters, such as the physical volume of the detection material, material density, its size and shape relative to the incident radiation and the interaction probability of the radiation particles. For γ-radiation this interaction probability is quite low and gamma's may travel large distances between interactions so it is therefore likely that the detector will have an efficiency less than 100%.

Detector types

Given the nature of γ-ray interactions, for a given γ-ray spectrum, optimum photopeak efficiency is obtained for a large detector volume with high-density and high Z-value. There are predominantly three detector types [5]:

- semi-conductors – these generally have a high energy resolution with a moderate Z value and a moderate density, for example hyper-pure germanium detectors (HPGe) with $Z_{Ge} = 32$ and $\rho_{Ge} = 5.3 g/cm^3$;
- "inorganic" scintillation detectors, eg. NaI, CsI and BGO, which tend to have good energy resolution and moderate to high densities ($\rho_{NaI} = 3.7 g/cm^3$, $\rho_{CsI} = 4.5 g/cm^3$ and $\rho_{BGO} = 7.1 g/cm^3$) and high Z values;
- "organic" scintillation detectors (or plastics) which have low density ($\rho \approx 1 g/cm^3$) and low Z.

The choice of detector type will depend on the application. The detectors described above are listed in order of decreasing resolution. The HPGe will show a sharp peak with low continuum, whereas plastic detectors show continuum with very little features. Scintillation detectors offer a trade-off between these extremes, being more efficient than the semi-conductors and offering better peak resolution than plastics.

The radiation relevant to this study has a low count rate and typically $E_\gamma < 3MeV$. This requires detectors with a high efficiency, especially considering the region of interest of a typical core measurement, i.e. 1cm thick disc with a 10cm diameter – a relatively small volume of material. The energy range of the gammas of interest also means that the dominant processes will be the photoelectric effect and Compton scattering (as mentioned previously). The low Z of plastic detectors nullifies their usefulness. Part of the optimisation process will involve maximising the peak-to-Compton ratio – i.e. minimising Compton scattering. Semi-conductors have a moderate Z value and provide a high energy resolution. However their lower Z value (Z_{Ge}=32 versus Z_{Bi}=83 for BGO detectors; and Z_I=53 for NaI detectors) means their efficiency is inferior to that of inorganic scintillation detectors. Since the cross section of the photo-electric effect scales with Z^4, this will play a significant role when considering the low count rates of natural radiation.

Therefore scintillation detectors are well suited to the task at hand, with their relatively high Z and reasonable energy resolution. BGO detectors will have a good efficiency with a reasonable resolution, and NaI and CsI detectors will provide a reasonable efficiency with better resolution. Furthermore, given that Cs is a much heavier atom than Na, the interactions are more likely to occur (probability proportional to Z) so a CsI detector is expected to be suitable for the project.

2.2.2.2 Energy spectra

A γ-ray energy spectrum represents a frequency histogram obtained when observing a radiating source. For each channel, representing an energy interval in the observed range, a count history is built up for a typical period of observation.

In Figure 2-3 we see the energy spectrum obtained from a CsI detector exposed to a ^{137}Cs source. Apart from the photopeak (I) we also notice a *Compton Continuum* (II).

The photopeak will be positioned at E_γ = 662keV and is due to the number of incident γ-rays that interact with the crystal through the photoelectric effect. The Compton continuum is due to scattered γ-rays that transfer part of their energy to the detector through multiple scattering. The continuum represents all the incident radiation that experienced Compton scattering but which has not fully been "captured". Hence the Compton continuum covers a range of energies less than that of the photopeak.

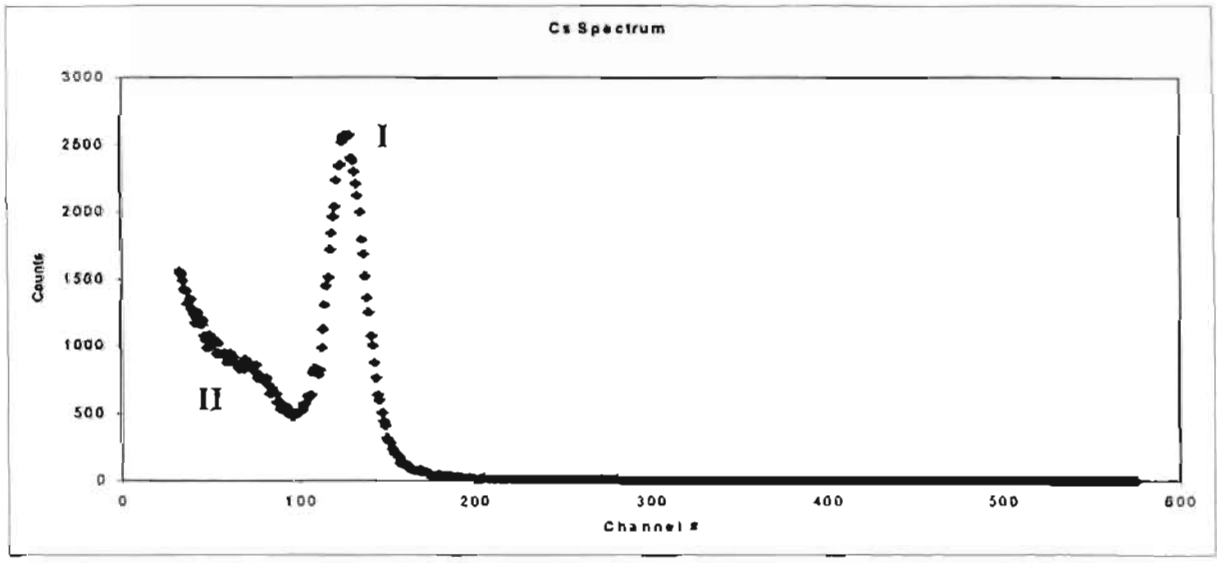

Figure 2-3: ^{137}Cs Spectrum recorded with the CsI detector described in this chapter.

There are several properties that can now be determined from such a spectrum – that of initial primary interest being the Energy Resolution. *Energy Resolution* is defined as ΔE/E where ΔE is the *full-width-half-maximum* (FWHM) and E is the energy of the peak. The FWHM is a measure of the ability of the detector to resolve a peak at that energy E. Also since the number of counts is conserved, large ΔE implies a low peak to Compton ratio. Good energy resolution (i.e. small ΔE) is a desirable property of a detector, and is dependent on the energy of a peak. i.e. if there were two photopeaks close together, a poor resolution (large ΔE) would result in wide overlapping peaks being plotted and resembling a single peak – whereas a good resolution (small ΔE) means that each peak would be narrow and hence both could be identified.

2.3 Initial Tests

2.3.1 Overview

Properties such as energy resolution, peak drift, output signal gain and degradation, etc, were analysed in a qualitative way to characterise the detector and its associated electronics.

2.3.2 Experimental Set-up

Some preliminary qualitative tests were run with the detector, without lead shielding, to gain insight into properties of both the CsI detector, and the electronics coupling it with the capture PC. This was done primarily using a ^{137}Cs source (with a photopeak at E_γ=662 keV). A sketch of the detector and crystal geometry is provided (Figure 2-4), and the sides of the detector are labelled in the figure for future reference.

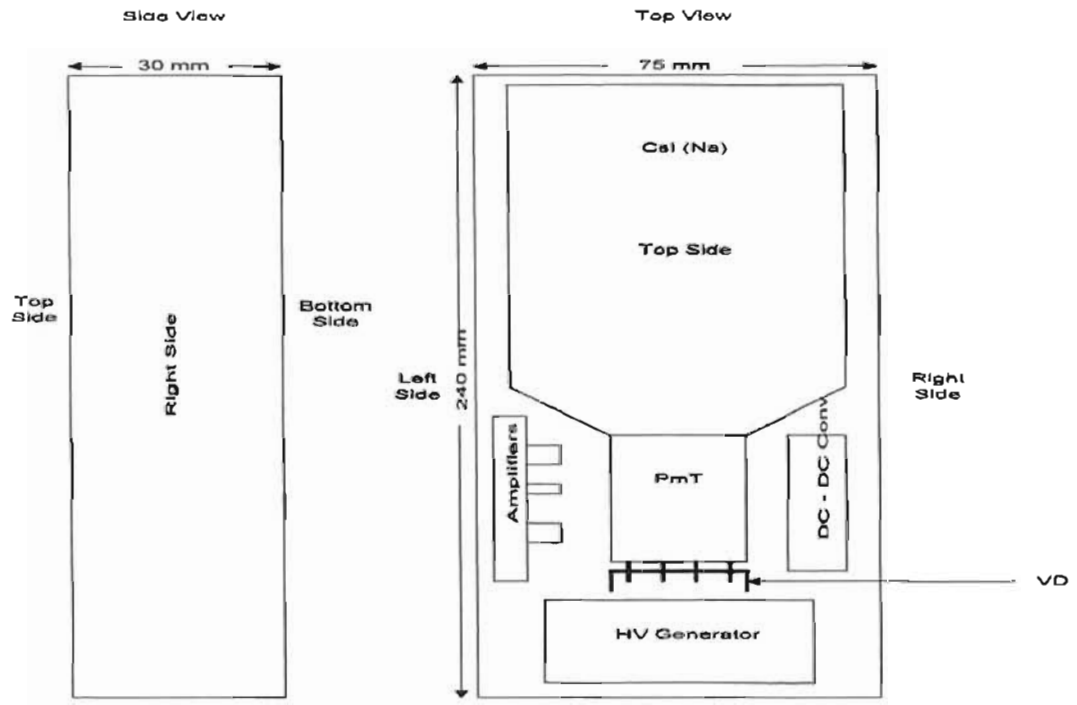

Figure 2-4: Detector and crystal dimensions.

Figure 2-4 shows a cross-section of the detector setup consisting of a CsI scintillation crystal mounted on a photo-multiplier tube (PMT). At the base of the PMT a voltage

divider (VD) is present that distributes the high voltage over the dinodes of the PMT and feeds the PMT signal to the amplifiers. The high voltage is generated by the high–voltage (HV) generator powered by the DC-DC converter. This converter also feeds the amplifiers that shape and amplify the signals provided by the PMT. The PMT converts the light flashes produced by gamma radiation in the scintillation crystal into electrical pulses.

The detector used is a product of Scionix Holland BV :

- Type: R65*30B160/1-HV-E3-C
  Caesium Iodide (Na)
- Serial #: SSH575
- Energy Resolution (for ^{137}Cs): 9.2% (at 23^0 C)

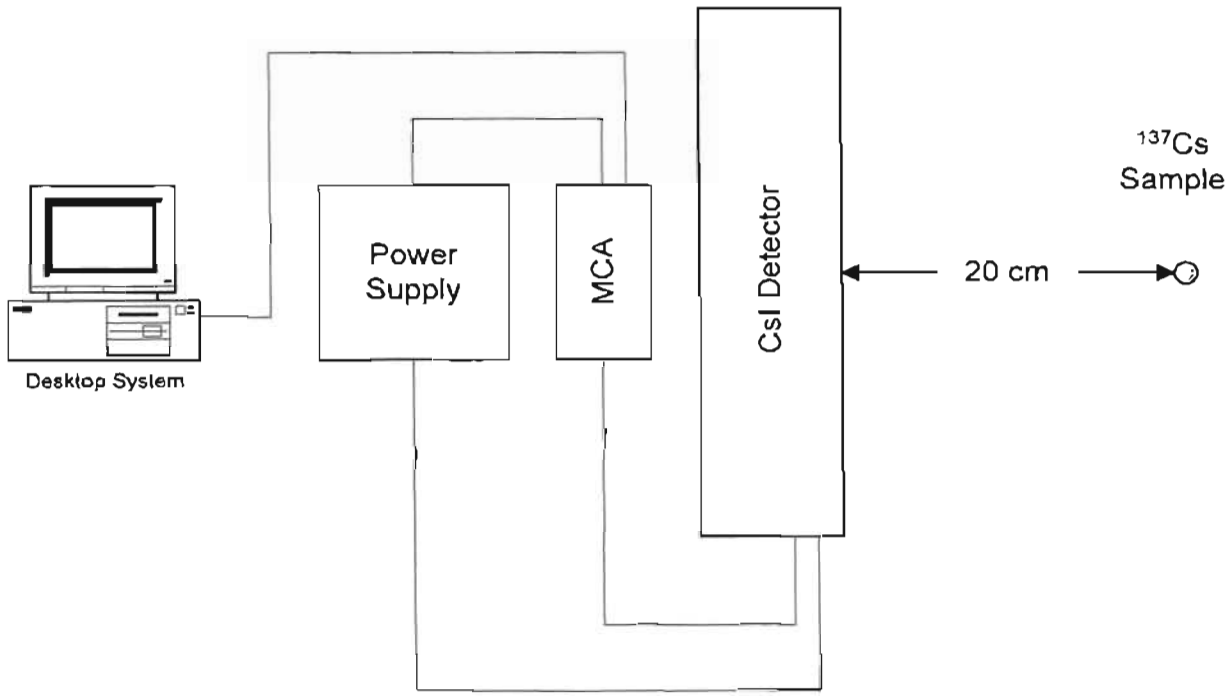

Figure 2-5 : Set-up of system for initial tests

The initial apparatus is shown in Figure 2-5. From the diagram we see that the source is placed approximately 20cm from the detector with the right side of the detector facing the Cs-source. The power supply used is a Nuclear Instrumentation Module (NIM) crate, in which the Multi-Channel Analyser (MCA) is housed and from which the detector draws a stable power supply of +12V. The MCA is interfaced with the computer via a National Instruments GPIB card.

Table 2-1: Component manufacturer, model and serial number.

Component	Manufacturer	Model	Serial #
NIM Crate	ORTEC	402D	BK512
MCA	Oxford Tennelec	PCA M	578
Multiplexer	Oxford Nucleus	DMR II	9112-1701
GPIB Card	Texas Instruments	PCII (ISA)	

An MCA performs the essential functions of gathering and storing data and producing output data in either a raw or analysed format. The MCA consists of an analogue-to-digital converter (ADC) for incoming data, some control logic necessary for routing input and output, as well as possibly a display module. In its simplest form the MCA merely acts as an interface for the PC – receiving analogue input data and converting it to digital form. The MCA is connection to the computer via a National Instruments GPIB card. The GPIB interface is a well-defined standard that allows the user to programmatically control any devices attached to it, and the card allows a fast data transfer between the PC and the MCA device.

2.3.3 Results and Discussion

Initially, measurements were run for approximately 60 seconds, and then the energy resolution ($\Delta E/E$) calculated from the full-width-half-maximum (FWHM) and peak values. The initial measurements using the ^{137}Cs sample gave $\Delta E/E \approx 20\%$.

It was noted that this resolution was worse than the 9.2% that can be expected for this particular detector (according to the specifications of Scionix), making it necessary to determine the reason for this reduced resolution.

This calculation was repeated several times with the detector and source in different positions to see if there would be any major effect on the resolution. For each measurement a different face of the detector was exposed to the source, with a fixed distance of approximately 20cm between them. Simultaneously the output signal was viewed on an oscilloscope, and all the connections were tested. In this way it was eventually found that the low input impedance of the multiplexer was causing a

voltage drop in the detector output signal. The multiplexer was then removed and measurements were repeated and a resolution of about 17% was found. This value is still not within the detector's specified resolution.

To test whether the detector was still functioning according to specifications it was connected to an MCA and PC system that was used in a previous study [10]. Subsequently the multiplexer and MCA were connected to a known stable detector system.

From these tests it emerged that the detector, multiplexer and MCA were functioning correctly and hence the deterioration of the energy resolution was caused by the new set up, possibly triggered by the low impedance of the output signal of the detector. One way to rectify this would be to amplify the signal from the detector with a linear amplifier. This should then give the multiplexer input a larger dynamic range and offset the voltage drop experienced.

To test this, a linear amplifier was connected to the system and several measurements are carried out. The new energy resolution of the system was now ~11.3%, which is approximately consistent with the specifications. Moreover, after these initial tests a more detailed investigation of the properties of the system could be started.

2.4 Energy Calibration

2.4.1 Overview

Having configured the CsI detector to give an acceptable energy resolution, the next step was to calibrate the channels. This allowed the determination of the relationship between the channel number of the MCA and the actual energy of the incident radiation.

2.4.2 Experimental Set-up

Energy calibration was conducted using a ^{137}Cs source, uranium ore, potassium and a monazite source. The detector was placed with its left side exposed to the source, and the source 20cm away as shown in Figure 2-6. The detector and source are placed on the frame as illustrated in Figure 2-7

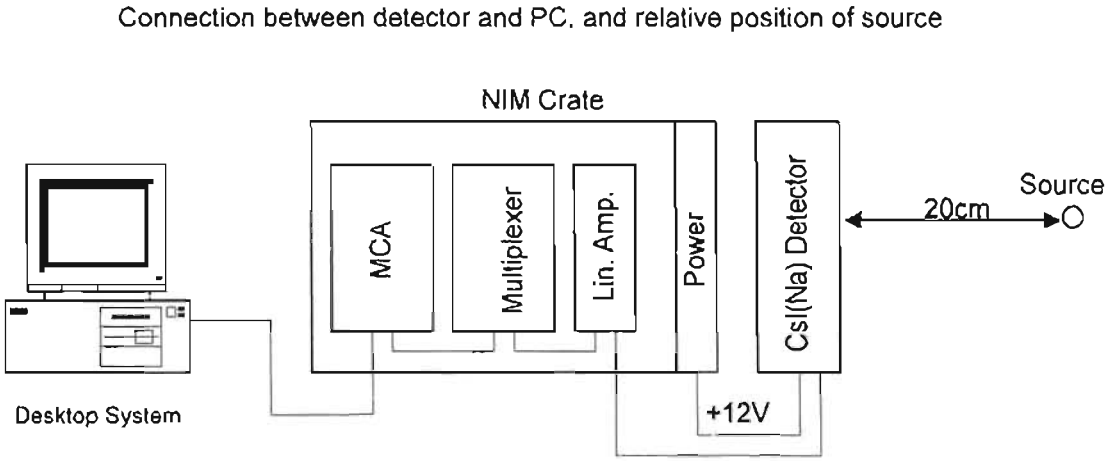

Figure 2-6 : Schematic layout of detector connection to PC with relative position of source.

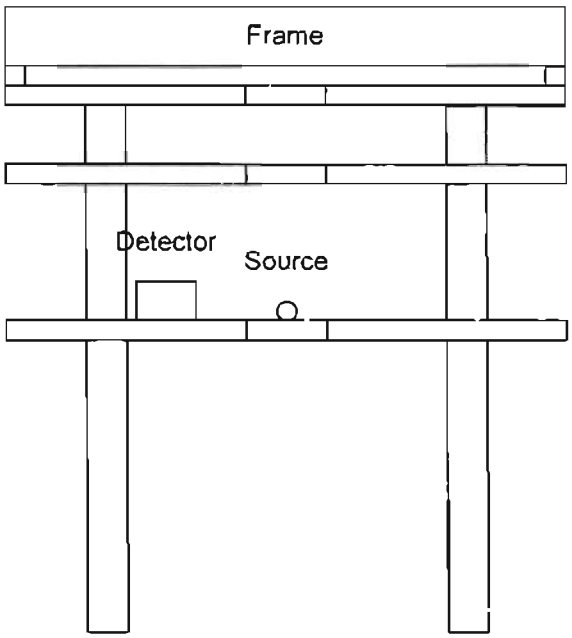

Figure 2-7 : Schematic representation of the position of the source and detector on the core-logger frame.

2.4.3 Results and Discussion

Several sources were used for the calibration. A Caesium source (^{137}Cs), Uranium ore (^{238}U), Potassium (^{40}K) and a monazite sample (^{232}Th). The same Cs source was used throughout this investigation. The U and K sources consisted of raw ore and the monazite was a mineral sample. The measured spectra for these sources can be found in Appendix I. Each spectrum was analysed to obtain the centroids for each peak. The analysis was performed using the Oxford software developed specifically for use with the multiplexer and did not incorporate background subtraction or any peak shaping. As can be seen from Table 2-2 this still gives an adequate number of points to make an energy calibration.

The relation between channel number and γ-ray energy is obtained assuming a linear regression analysis $y = ax + b$, in which x is the channel number and y is the γ-ray energy in keV. Figure 2-8 presents the data points and the best fit analysis.

Table 2-2: Calibration data. The first column represents the known energy of a peak, and the Channel # is the position of the centroid in the spectrum data obtained. The source listed is not the actual source of any particular line, but is the parent of the decay chain from which the lines originate. The spectra obtained are included in Appendix I.

Source	E_γ (keV)	Channel #
^{232}Th	583	591
^{238}U	609	604
^{137}Cs	662	655
^{232}Th	911	940
^{238}U	1120	1149
^{40}K	1460	1501
^{238}U	1764	1801
^{238}U	2204	2284
^{232}Th	2614	2730

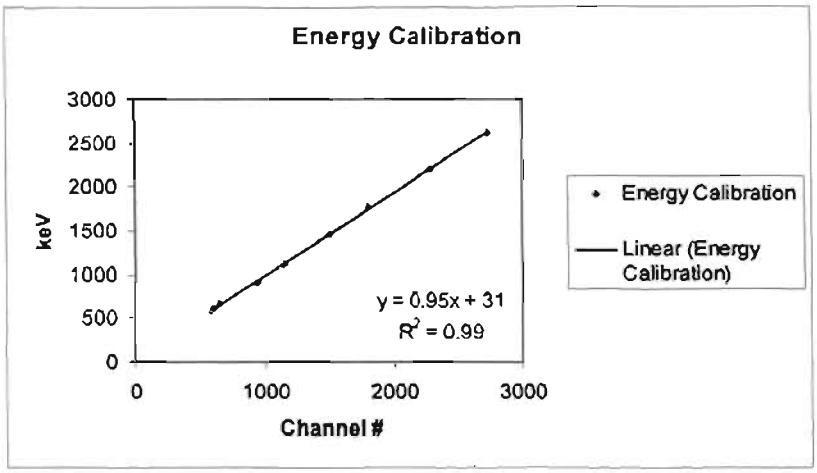

Figure 2-8: Plot of the energy of the calibration source versus the channel number.

The optimal fit was found for a = 0.95 ± 0.05 keV, b = 31 ± 2 keV, where the linear relation now becomes : $y = 0.95x + 30.90$, with the uncertainties quoted above. The regression coefficient R^2 yielded a value very close to unity, which indicated a high degree of confidence in the linear relationship between the peak energy and the channel #.

The intercept (b = 31keV) in the linear relation above gives the offset for Channel # = 0. It was now possible to use this offset in the calculation of energy resolution.

2.4.4 Gain Drift

Gain drift causes the centroid of the peak to shift, and may be influenced by factors such as temperature change. To examine this possibility it would be necessary at some later stage to re-calibrate the detector and to monitor the possibility of peak shift over a period of time. At this point however, it can be noted that the measurements were taken over a short period, and thus drift effects would be negligible. At some later stage in the investigation of this detector it will be necessary to return to this topic and examine it thoroughly. For the time being, however, it was assumed that the drift could be ignored.

2.5 Background measurements

2.5.1 Overview

The background is that spectrum measured by the detector for a period of time without a specific source being present. The source of the background spectrum is a combination of all objects around the detector that may radiate energy, as well as cosmic rays, building materials, etc. Its effect is undesirable, and in general one endeavours to reduce the background and subtract it from the spectra. This section describes the lead brick shield used to reduce the unwanted background radiation. The effectiveness and effect of these lead bricks will be evaluated.

2.5.2 Experimental Set-up

The measurements were done in several stages, starting with an unshielded detector. After this a lead shield was built up around the detector, in increments of 5cm, to 15cm. This increment of 5cm was set by the minimum thickness of the two available sizes of lead bricks which had dimensions of $20\times10\times5cm^3$ and $10\times10\times5cm^3$.

Once again the detector was placed on the second platform on the core-logger frame (as illustrated in Figure 2-7) and was connected to the PC via the MCA NIM module (as illustrated in Figure 2-6).

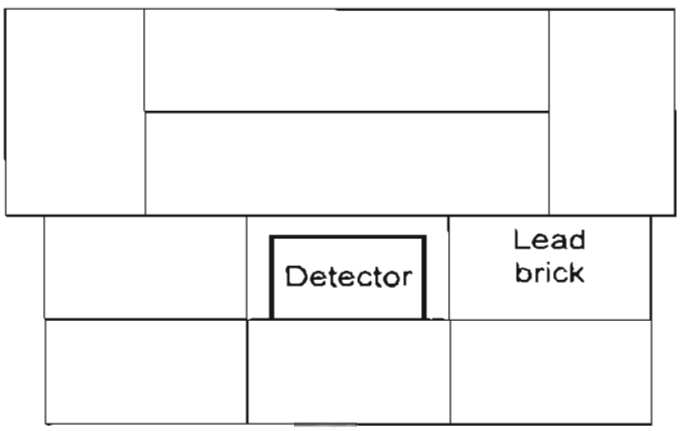

Figure 2-9 : Example of 10cm lead shield configuration.

To test a single layer of lead shielding, the detector was entirely encased in a structure composed of lead bricks. Figure 2-9 illustrates the shielding of the detector. It must be noted that this 10cm thickness is the *minimum* thickness of the shield at any point around the detector, and may in some places be more, but never less.

2.5.3 Results and Discussion

The majority of the background measurements were each performed over 2 hours to better observe the effects of varying ambient conditions, such as temperature. No effects of temperature change or diurnal variations were observed. Table 2-3 therefore presents time-averaged values for various windows of the energy spectrum and several thicknesses of lead shielding. In addition a cut-off was set at 173keV to exclude noise.

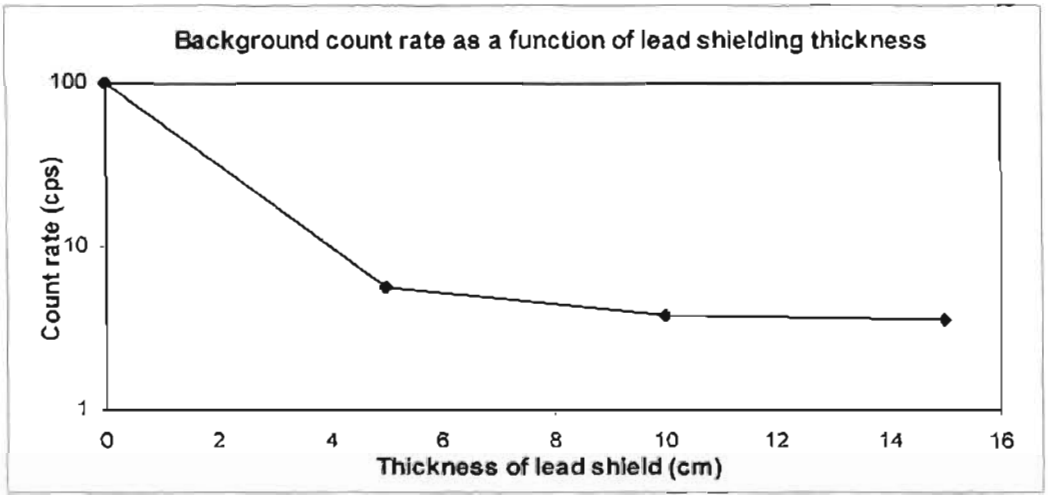

Figure 2-10: Total count rate of the background as a function of lead shielding thickness.

Looking at the total count rate (in Table 2-3, Figure 2-10) we see that it has decreased from the initial 99.18 to 3.63 cps with 15cm of lead. The effect of the lead decreases as a function of thickness, and increasing the lead thickness from 10cm to 15cm makes very little difference to the overall count rate (count rate decreases from 3.73 cps to 3.63 cps which is ~3% of the total) . This is indicated in Figure 2-11 where the ratios are plotted. Note especially how the fractional decrease tends towards 1, which

implies that a limit will be reached in the benefit gained by each successive layer of lead.

Table 2-3 : Count rates per Energy Window for various lead shielding

E Window (keV)	Lead shielding			
	0cm	5cm	10cm	15cm
173 – 534	67.0 ± 0.08	3.03 ± 0.02	2.460 ± 0.005	2.430 ± 0.011
534 – 753	14.0 ± 0.04	0.700 ± 0.010	0.410 ± 0.002	0.390 ± 0.004
753 – 1276	10.6 ± 0.03	0.800 ± 0.011	0.330 ± 0.002	0.300 ± 0.003
1276 – 1637	4.14 ± 0.02	0.340 ± 0.007	0.1400 ± 0.0013	0.120 ± 0.002
1637 – 2417	2.13 ± 0.02	0.290 ± 0.007	0.1300 ± 0.0012	0.120 ± 0.002
2417 – 2835	0.590 ± 0.008	0.090 ± 0.004	0.040 ± 0.0010	0.0400 ± 0.0013
2835 – 3500	0.200 ± 0.005	0.080 ± 0.003	0.050 ± 0.0010	0.0500 ± 0.0015
3500 – 3923	0.500 ± 0.007	0.250 ± 0.006	0.190 ± 0.0015	0.180 ± 0.003
Total Count Rate (cps)	99.18 ± 0.10	5.60 ± 0.02	3.760 ± 0.007	3.631 ± 0.013

It should also be noted that the lead blocks themselves will also add to the background measured by the detector. Radioactive impurities in the metal may produce detectable radiation, one example being the radioisotope ^{210}Pb which emits β^- and introduces *Brehmsstrahlung*. (Brehmsstrahlung is the process whereby decelerating particles emit radiation. As the particle's velocity changes it will emit the lost energy in the form of γ-radiation.) This emitted β^- has a maximum energy of 0.064MeV and as such will have no noticeable effect on the energy ranges we are considering since the cut-off is at 173keV. However, the daughter nucleus ^{210}Bi in turn has a half-life of 5 days and a β^- decay with a maximum energy 1.163MeV. This decay series may exist for other elements deriving from Pb isotopes, or their parents, etc. It is difficult to determine with certainty what other impurities are present in the lead blocks without a more detailed study of the lead itself using detectors with a much higher resolution.

Thus, it is possible for the lead shielding itself to function as a radioactive source. This will limit the lowest level of detectable activity.

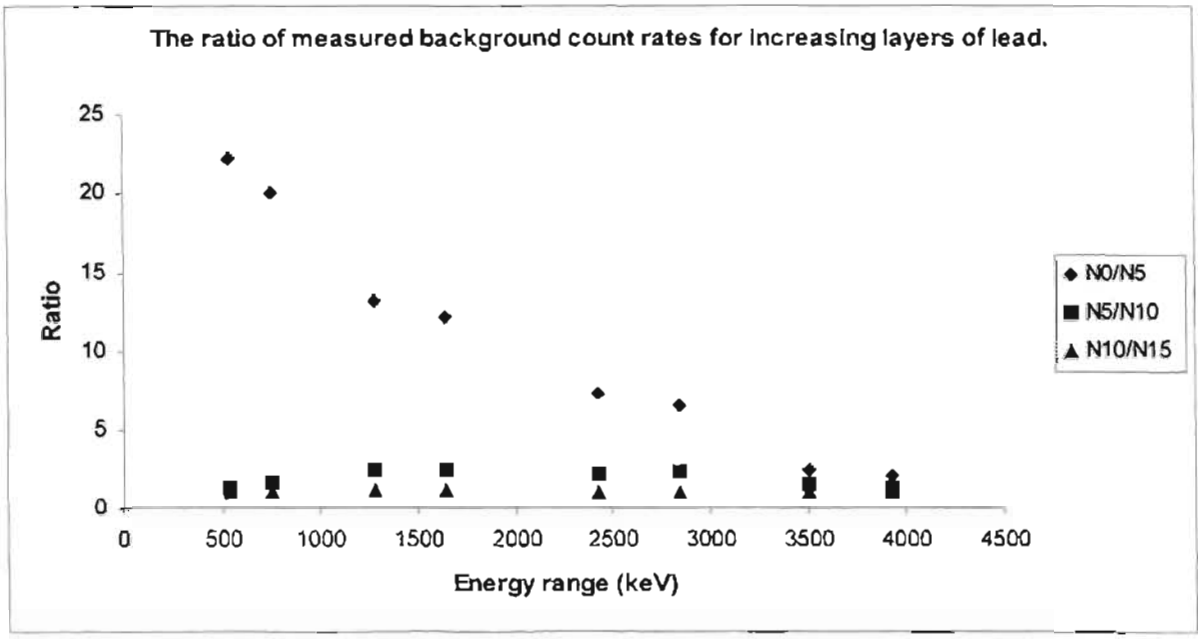

Figure 2-11: The ratios of the background count rates for increasing lead layers as a function of energy.

Figure 2-11 illustrates the relationship between the attenuation factor and the energy of the incident radiation for successive layers of lead. Initially the reduction factors were large (17 times reduction for 5cm of lead shielding) but become minimal as we increase the thickness of the shielding layer. The difference between the 10cm and 15cm layers is small enough to decide against using a 15cm layer permanently. The 10cm layer is not as heavy (for manipulation purposes and will not exert excessive strain on the supporting structures) and provides almost the same shielding as 15cm. This also demonstrates the energy dependence of the shielding. The initial reductions for the low energy ranges were substantial – between 22.12 (for 173keV to 534keV range) to 12.18 (for 1276keV to 1637keV range). For higher energies the initial decreases were smaller (7.34 for range 1637keV – 2417keV down to 2.08 for energy range 3500 – 3923).

From the figure it can be seen that after 10cm the lower energy ranges are almost completely unaffected by additional layers of lead. However, the high energies are still attenuated as the lead thickness increases from 10cm to 15cm.

As a function of lead thickness, x, the count rate will fall off as $\sim e^{-\mu x}$ where μ, the attenuation coefficient, is energy dependent. The general trend displayed in Figure 2-11 is reasonable but there are some features that remain unresolved. The N_5/N_{10} data shows a shoulder at ~1250keV before decreasing again towards the higher energies. The N_{10}/N_{15} line shows a similar increase and also at ~3500keV. According to the relationship, $I \sim e^{-\mu x}$, the count rate should fall off exponentially with x. However, for increasing lead thickness, the lead itself could be contributing to the detected radiation. This will be considered in the following section.

For the natural radiation that will be studied by the core-logger this may cause difficulties. The energy levels and activity of the natural radiation may be comparable to the background measured here, so it is important to fully understand the composition of the background spectrum and its sources. If possible the background function should be modelled and the response function of the detector calculated.

2.5.4 Background contribution

The absorption and scattering of γ-radiation in matter results in a decrease in radiation intensity, energy and change in angular distribution. In first approximation the reduction in the total intensity can be written as

$$I(d) = I_0 e^{-\mu d}, \tag{2.3}$$

where I_0 is the initial intensity in terms of the total count rate of the detector (cps), d is the thickness of the material and μ is the (energy dependent) linear attenuation coefficient. For the purposes of this background measurement the function needs to be corrected for the contribution of the lead blocks themselves. This contribution will also be a function of d, denoted $I_{Pb}(d)$, and (5.4.1) becomes

$$I(d) = I_0 e^{-\mu d} + I_{Pb}(d). \tag{2.4}$$

Using the data obtained for the total count rate N as a function of d, there are 4 points (see Figure 2-10) that can be used to solve the above equation for the attenuation coefficient μ. Using the equations

$$I(5) = I_0 e^{-5\mu} + I_{Pb}(5), \tag{2.5a}$$

$$I(10) = I_0 e^{-10\mu} + I_{Pb}(10), \text{ and} \tag{2.5b}$$

$$I(15) = I_0 e^{-15\mu} + I_{Pb}(15) \tag{2.5c}$$

we can solve (5.4.3b) for $I_{Pb}(10)$ by rearranging to get

$$I_{Pb}(10) = I(10) - I_0 e^{-10\mu}. \tag{2.6}$$

To solve this set of equations it is necessary to make an assumption about the form of I_{Pb}. The first approximation would be that of a linear function, but it is easily seen that this will be unreasonable. Solving it gives $e^{-10\mu} = -6.6$, which yields an imaginary solution.

As a second approximation it was assumed that the contribution from the lead equals that of the first 5cm plus an attenuated contribution of the second layer. This led to an equation of the form

$$I_{Pb}(10) = I_{Pb}(5)(1 + e^{-5\mu}). \tag{2.7}$$

Substituting (2.7) into (2.5b) it is possible to solve for $I_{Pb}(5)$ and $I_{Pb}(10)$ and hence for μ, leading to $\mu = 0.797\text{cm}^{-1}$. A more useful value, however, is the mass attenuation coefficient which is given by μ/ρ. The linear coefficient is dependent on the density of the material hence its use is fairly limited. On the other hand, for a given gamma energy, the mass attenuation coefficient is independent of the density and hence state of the material. For this reason it is more widely used. For lead $\rho = 11.34\text{g/cm}^3$, and $\mu/\rho = 0.07\text{cm/g}^2$.

Table 2-4: Mass attenuation co-efficient for $_{82}$Pb for energies from 0.15MeV to 3MeV. Data are taken from JH Hubbel and SM Seltzer [11].

E (MeV)	μ/ρ (cm/g^2)	E (MeV)	μ/ρ (cm/g^2)
0.150	1.06	0.800	0.0464
0.200	0.587	1.00	0.0365
0.300	0.246	1.25	0.0299
0.400	0.137	1.50	0.0264
0.500	0.0913	2.00	0.0236
0.600	0.0682	3.00	0.0232

The contribution from the lead to the background measurement is likely to stem from the β-decay of ^{210}Bi, with a maximum energy of 1.163MeV. The process that gives

rise to this is given by $n \rightarrow p + e^{-} + \bar{\nu}$. Here the proton remains bound to the lattice and in general the neutrino goes undetected. The energy of the β^{-} can then vary between zero and the maximum (1.163MeV). This range is due to the fact that the process involves three bodies which need to conserve total energy and momentum. The energy spectrum of the β^{-} has a continuous Gaussian shape with an average energy ~ $1/3\beta_{max}$. For our purposes, where the Brehmsstrahlung radiation was of importance, absorption weights the distribution and we expected that the effective energy would be approximately half the maximum, i.e. ~ 600keV.

The experimental, μ/ρ = 0.07cm/g^2 is in good agreement with the value of 0.0682cm/g^2 given in the literature for an energy of 600keV.

In conclusion it must be stated that, as mentioned earlier in the text, understanding the effect of the background radiation is imperative when the radiation activity is comparable to the background activity.

2.6 Slit calibration

2.6.1 Overview

As described in the foreword, the primary objective of the core logger system was to automate the radiometric examination of core-samples with a spatial resolution of about 1 cm. This resolution requirement was obtained by constructing a slit in the lead shield placed around the detector. The lead shield would then protect the detector from general background and most of the radiation coming from the examined core – except for a disc with a thickness of about 1cm. By carefully designing the slit, it was possible to obtain the optimal configuration that allowed a measurable 1cm spatial resolution. The initial approach was to construct a simple slit using a suitable arrangement of the lead bricks.

2.6.2 Experimental set-up

The detector/source positioning was similar to that shown in Figure 2-7, except that the components were now moved to the top platform of the frame.

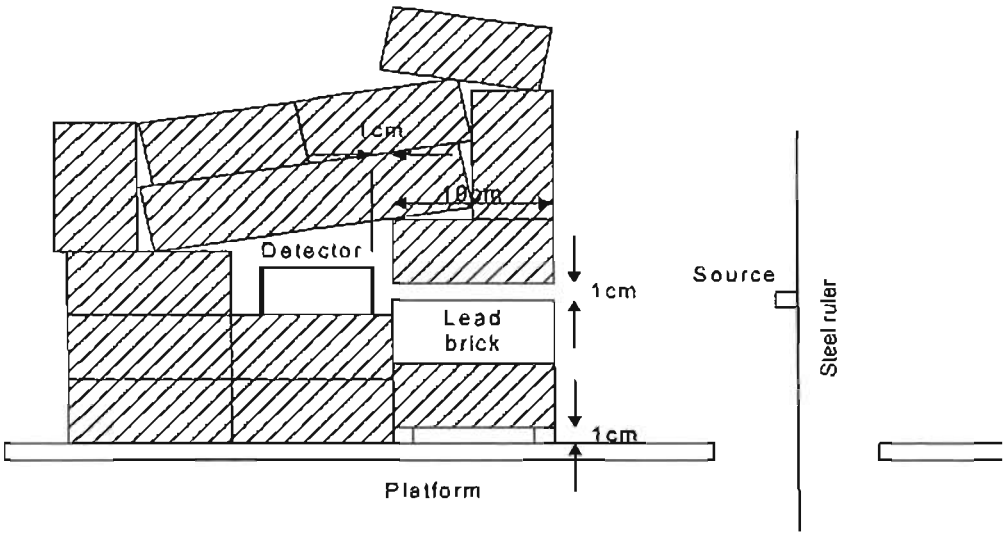

Figure 2-12: Cross section of the detector setup in the lead shield containing a 1cm slit. The ^{137}Cs source was attached to a steel ruler.

From Figure 2-12 it can be seen that the detector was effectively placed within a lead castle of 10cm thickness. The source was placed approximately 18cm from the detector positioned above the hole in the core-logger frame. By a suitable arrangement of the bricks, a slit was formed in the wall facing the source. The dimensions of the slit are 20cm×10cm×1cm. This is the first approximation to obtain the 1cm spatial resolution, although the slit may need to be narrower.

The initial tests were carried out using a point source with a thickness of about 1mm and a spot diameter of roughly 1mm.

2.6.3 The effect of the slit on background measurements

A necessary prerequisite to making any measurement using the source was to check the effect of the slit on the observed background count. Hence background measurements were repeated and the spectra recorded. Furthermore, up until this point the set-up had been situated on the second level platform of the core-logger frame structure. Before investigating the resolution and behaviour of the slit the

entire set-up was moved to the top level and the background measurement repeated. This was to test whether the location of the system would have any effect on the background, but as suspected it did not.

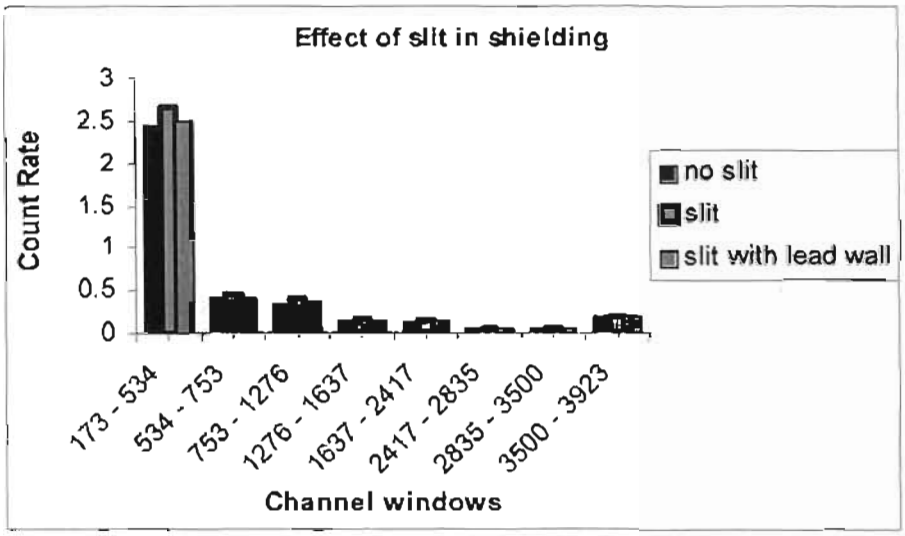

Figure 2-13: The effect of the slit on the background measurement.

Given the thickness of the lead shield and the depth of the slit, it was safe to assume that the increase in background count rate of the system with the slit in place was primarily due to a fairly directional room background radiation penetrating the slit. To test this assumption a 10cm thick lead wall was built up 15cm opposite the slit. The results are shown in Figure 2-13.

We can see from Figure 2-13 the count rate rose slightly when the slit was open, yielding an overall count rate of 4.13cps ± 0.02cps, whilst with the slit closed this value was 3.77cps ± 0.01cps. When the lead wall was placed in front of the open slit the count rate was 3.86cps ± 0.02cps, which is a good indication that the directional radiation had now been shielded. This meant that the lead shield effectively excluded unwanted radiation and admitted only that which was within the required spatial resolution.

2.6.4 Spatial resolution of 10mm slit using a point-like source

The next objective was to investigate quantitatively the spatial resolution of the system using a point like ^{137}Cs source. The source was placed in front of the slit and then moved vertically in increments of 2mm and 50mm.

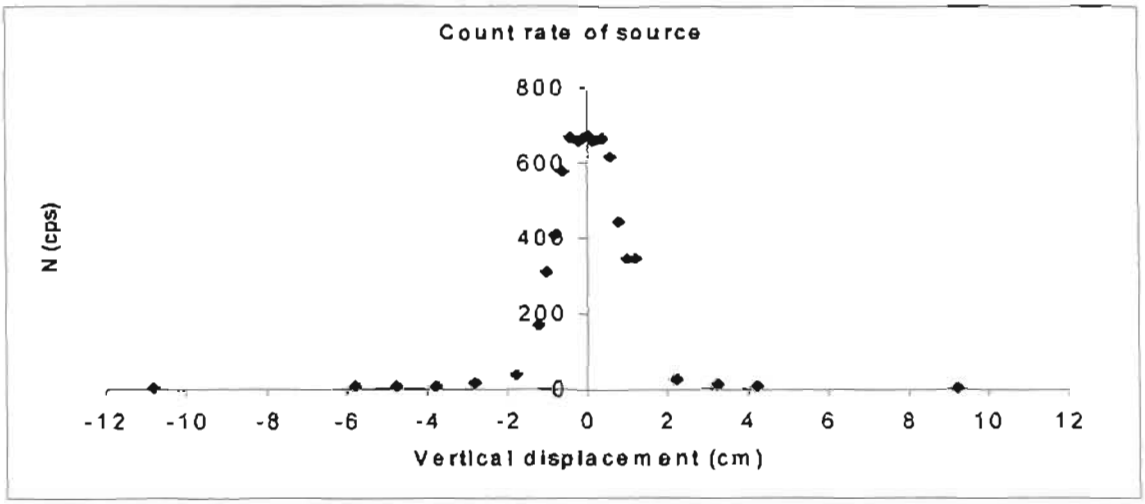

Figure 2-14: Total count rate as a function of source position with the source located 7.5cm from the slit.

The measuring time depended on the count rate at each position. A displacement of 0cm represented the position where the source was directly opposite the centre of the slit, with negative displacements being below the slit. The source was fixed to a steel ruler, and the ruler, together with the attached source, was then moved vertically. The initial vertical profile was obtained with the source at a horizontal distance of 7.5cm from the front side of the slit. A measurement was initially performed with the ruler in place with no source attached to confirm that it had no measurable effect on the background.

Figure 2-14 shows the total count rate as function of the source position. Initially profiles were obtained using large step sizes of 1 – 5cm. After examining those results it was decided that a more detailed measurement (i.e. smaller step size) was needed between slit edges. This could account for the minor shoulder at ~1cm as a result both of a slight shift in the entire energy range (the measurements were taken at different times) and inaccuracies in the displacement reading. Using the ruler in this

manner allows for a ±0.5mm inaccuracy in measured displacement, and this may account for the "shift" in the values taken at different times.

Table 2-5: Total count rate N (and count per energy window) of the CsI detector as a function of the vertical position of a ^{137}Cs source placed 7.5cm from the slit.

Disp (cm)	173 – 634 (keV)	634 – 753 (keV)	753 – 1276 (keV)	1276 – 1637 (keV)	1637 – 2417	2417 – 2835	2835 – 3500	3500 – 3923	N (cps) ± ΔN
-10.8	3.320 ± 0.020	0.450 ± 0.008	0.35 ± 0.011	0.140 ± 0.007	0.140 ± 0.012	0.040 ± 0.007	0.060 ± 0.020	0.15 ± 0.04	4.69 ± 0.02
-5.8	4.92 ± 0.03	0.9 ± 0.011	0.36 ± 0.011	0.150 ± 0.007	0.140 ± 0.012	0.040 ± 0.007	0.060 ± 0.020	0.2 ± 0.04	6.76 ± 0.03
-4.8	5.70 ± 0.020	1.230 ± 0.010	0.340 ± 0.009	0.150 ± 0.006	0.140 ± 0.009	0.030 ± 0.005	0.060 ± 0.018	0 19 ± 0.03	7.83 ± 0.04
-3.8	7.030 ± 0.020	2.08 ± 0.0131	0.350 ±0.009	0.160 ± 0.006	0.140 ± 0.009	0.040 ± 0.005	0.060 ± 0.018	0.19 ± 0.03	10.02 ± 0.05
-2.8	10.270 ± 0.020	4.40 ± 0.015	0.950 ± 0.011	0.150 ± 0.004	0.130 ± 0.007	0.050 ± 0.004	0.060 ± 0.014	0.19 ± 0.03	15.60 ± 0.08
-1.8	21.70 ± 0.03	16.68 ± 0.03	0.740 ± 0.010	0.140 ± 0.004	0.140 ± 0.007	0.040 ± 0.004	0.060 ± 0.014	0.19 ± 0.03	39.63 ± 0.12
-1.2	67.31 ± 0.03	97.73 ± 0.04	4.060 ± 0.013	0.170 ± 0.003	0.120 ± 0.004	0.050 ± 0.003	0.060 ± 0.008	0.220 ± 0.016	169.5 ± 0.4
-1.0	111.95 ± 0.04	188.38 ± 0.06	8.620 ± 0.019	0.180 ± 0.003	0.140 ± 0.004	0.040 ± 0.002	0.080 ± 0.010	0.180 ± 0.014	309.2 ± 0.6
-0.8	143.20 ± 0.05	254.77 ± 0.07	12.420 ± 0.020	0.260 ± 0.003	0.140 ± 0.004	0.030 ± 0.002	0.060 ± 0.008	0.210 ± 0.016	410.6 ± 0.7
-0.6	196.68 ± 0.06	362.37 ± 0.08	17.68 ± 0.03	0.310 ± 0.004	0.140 ± 0.004	0.050 ± 0.003	0.070 ± 0.009	0.220 ± 0.016	576.8 ± 0.8
-0.4	230.46 ± 0.06	418.07 ± 0.08	20.18 ± 0.03	0.330 ± 0.004	0.140 ± 0.004	0.050 ± 0.003	0.080 ± 0.009	0.200 ± 0.015	668.7 ± 0.9
-0.2	226.68 ± 0.06	411.28 ± 0.08	19.63 ± 0.03	0.330 ± 0.004	0.150 ± 0.004	0.040 ± 0.002	0.070 ± 0.009	0.220 ± 0.016	657.6 ± 0.9
0	233.62 ± 0.06	418.81 ± 0.08	19.33 ± 0.03	0.330 ± 0.004	0.150 ± 0.004	0.050 ± 0.003	0.070 ± 0.009	0.230 ± 0.016	671.8 ± 0.9
0.2	232.51 ± 0.06	409.48 ± 0.08	18.28 ± 0.03	0.340 ± 0.004	0.170 ± 0.005	0.040 ± 0.002	0.060 ± 0.008	0.200 ± 0.015	660.3 ± 0.9
0.4	232.96 ± 0.06	412.2 ± 0.08	18.11 ± 0.03	0.340 ± 0.004	0.150 ± 0.004	0.0400 ± 0.0020	0.050 ± 0.008	0.190 ± 0.015	663.3 ± 0.9
0.6	218.85 ± 0.06	381.36 ± 0.08	16.17 ± 0.03	0.320 ± 0.004	0.140 ± 0.004	0.050 ± 0.003	0.060 ± 0.008	0.210 ± 0.015	616.5 ± 0.8
0.8	166.21 ± 0.05	267.52 ± 0.07	9.60 ± 0.020	0.220 ± 0.003	0.140 ± 0.004	0.030 ± 0.002	0.070 ± 0.009	0.220 ± 0.016	443.5 ± 0.7
1.0	137.81 ± 0.05	201.12 ± 0.06	6.250 ± 0.016	0.190 ± 0.003	0.140 ± 0.004	0.040 ± 0.0020	0.070 ± 0.009	0.190 ± 0.015	345.4 ± 0.6
1.2	135.65 ± 0.08	200.450 ± 0.010	6.47 ± 0.03	0.180 ± 0.005	0.130 ± 0.007	0.050 ± 0.004	0.060 ± 0.015	0.20 ± 0.03	342.8 ± 0.4
2.2	14.92 ± 0.04	7.96 ± 0.03	0.420 ± 0.011	0.150 ± 0.006	0.140 ± 0.010	0.040 ± 0.006	0.060 ± 0.020	0.19 ± 0.04	23.84 ± 0.06
3.2	8.56 ± 0.03	4.020 ± 0.020	0.380 ± 0.012	0.140 ± 0.007	0.130 ± 0.012	0.040 ± 0.007	0.060 ± 0.020	0.19 ± 0.04	12.60 ± 0.04
4.2	3.470 ± 0.020	4.80 ± 0.03	0.370 ± 0.011	0.150 ± 0.007	0.130 ± 0.011	0.040 ± 0.007	0.060 ± 0.020	0.19 ± 0.04	9.19 ± 0.04
9.2	2.29 ± 0.017	1.77 ± 0.015	0.350 ± 0.011	0.150 ± 0.007	0.140 ± 0.012	0.040 ± 0.007	0.06 ± 0.03	0.19 ± 0.04	4 98 ± 0.04

Table 2-5 presents the count rate of the source as function of the source position. The table includes the overall count rate and the count rate in each energy window. From this it is evident that the source does not affect the high energy ranges since the count rate in these windows is approximately equal to the background values and remains unaffected by the movement of the source. It is interesting to note that the source does seem to have an effect on energy ranges up to roughly 1200keV despite its maximum energy being 662keV. This effect is a result of *electronic pileup* and is related to *electronic deadtime*. Pileup occurs when interactions take place in too short

a time interval for the detector or the electronics to distinguish them as separate events. The sum of the energies of the incident γ-rays is then mistakenly assumed to be the energy of a single particle. This causes energy ranges above the photopeak energy of 662keV to be affected. Similarly the lower energy ranges can be affected by Compton scattered particles that are then absorbed while still inside the detector. For example, a single γ-ray may be scattered when it enters the detector material, and the scattered gamma is then detected coincidentally with a second gamma entering the detector. It can also be seen that the lower energy ranges behave in a similar manner to the overall count rate as indicated.

It is also possible to compare this to the background measurements made in §2.5; particularly Table 2-3. This comparison demonstrates clearly that the source has had no effect on the higher energy levels (>1200keV) since the count rates recorded here are comparable to those in Figure 2-13. Comparing further, it is obvious that at most energy ranges the values reach background levels, except for those falling within the energy peak.

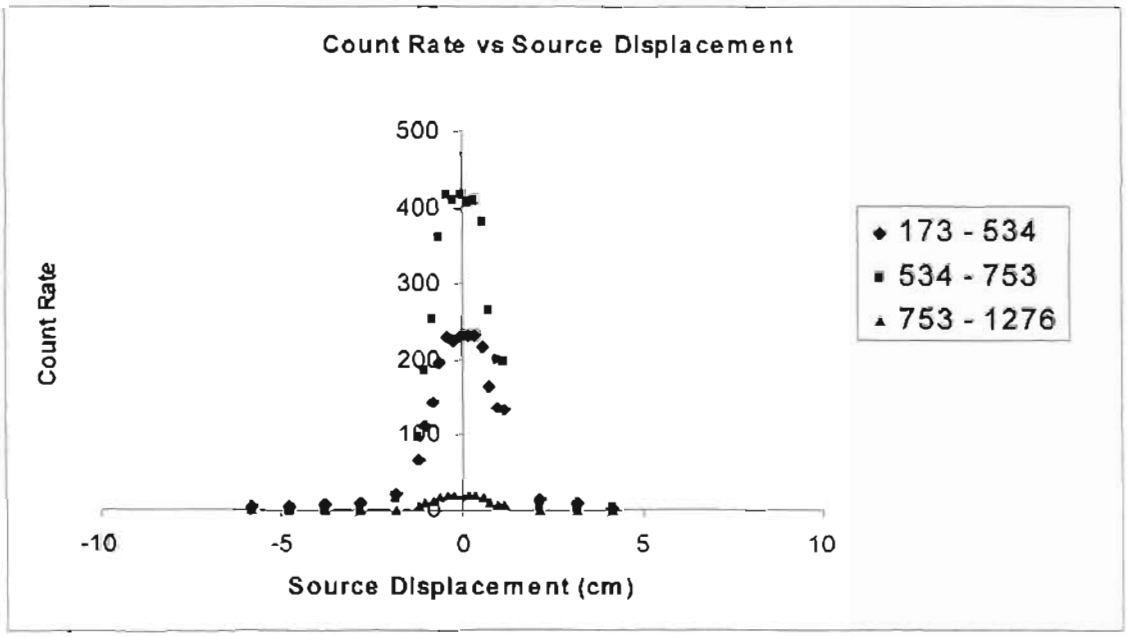

Figure 2-15: Count rate and source displacement for several energy windows for a 10mm slit.

Figure 2-15 shows the count rates (for the three energy windows of interest) as function of source position. From Figure 2-15 it is clear that the source only has a noticeable effect on energies up to ~700keV. The small shoulder at a displacement of

~2cm seen in Figure 2-14 is again present. From Figure 2-14 and Figure 2-15 above it is evident that the slit provides a sharp cut-off at the edges, i.e. the count rate falls off rapidly as the source is moved out of the line-of-sight of the detector.

From Figure 2-14 and Figure 2-15 it is possible to make an estimation of the spatial resolution of this slit configuration by calculating the FWHM of the count rate peak. Working with the overall count rate the FWHM is approximately 2cm. It is not possible to give a more precise value due to the presence of the shoulder.

2.6.5 Spatial resolution of a 6mm slit using a point-like source

Given the overall estimate of 2cm for the spatial resolution it was necessary to consider a different slit configuration since the 10mm slit did not satisfy the project specification. All the measurements were then repeated with a narrower, 6mm slit. Only displacements ~1cm either side of the centre of the slit were measured.

Figure 2-16 below presents the total count rate N as a function of source position for the 6mm slit. From Figure 2-16 the FWHM can be calculated, giving an estimate for the spatial resolution of the 6mm slit of ~ 0.7 cm, which is within the required range.

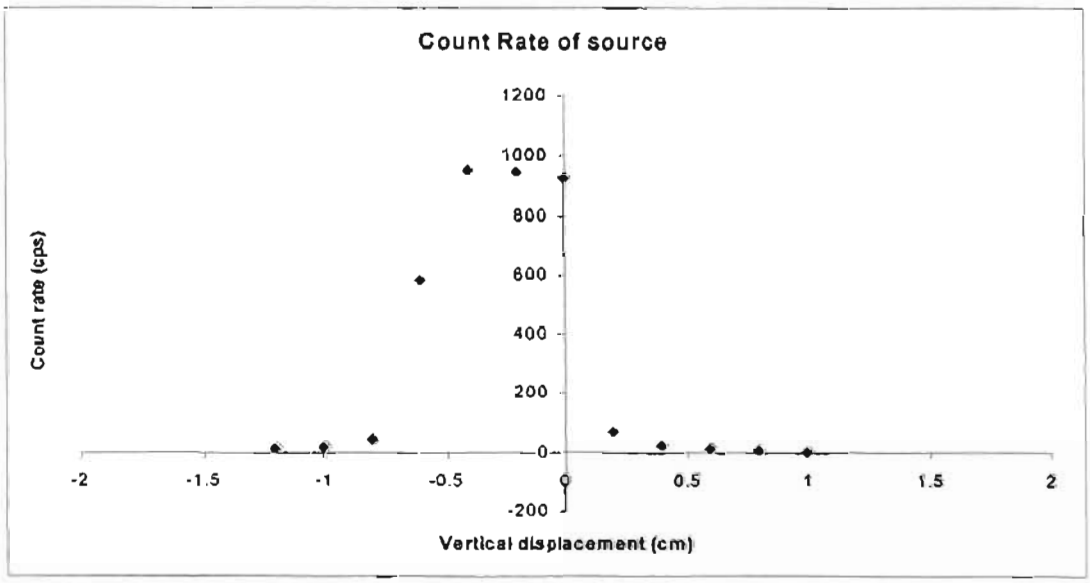

Figure 2-16: Total count rate as a function of vertical position. Slit width = 6mm, distance to slit = 0cm.

However, this measurement was made close to the slit, and the resolution will degrade as the source is moved further away. The extent of this degradation was not clear at this point but is investigated further in the next section.

The improved steepness of the slit edge is also noticeable here, although more data will be necessary in order to examine this quantitatively. In addition, it can be noticed that the centre of the peak is offset from the assumed centre of the detector by a distance of 2mm. This may be due to several factors, the first being that the detector setup was not completely symmetrical, i.e. the detector was not completely centred in the lead shield and the slit was not directly in the centre of the detector. Furthermore the scale was taken from the 10mm case to facilitate comparison, and the change in slit size (hence resulting in a shift of the centre) was not accounted for.

Table 2-6: Distance to slit = 0cm. Slit width = 6mm. This shows the count rate for several energy windows.

	Count rate in E window (cps)		
Displ (cm)	173 – 534 keV	534 – 753 keV	753 – 1276 keV
-1.2	9 ± 4	3.2 ± 1.2	0.1 ± 0.9
-1	13 ± 4	6 ± 3	0.1 ± 0.9
-0.8	26 ± 6	19 ± 5	0.4 ± 1.1
-0.6	203 ± 14	364 ± 19	15.8 ± 1.1
-0.4	336 ± 19	590 ± 20	27 ± 4
-0.2	339 ± 19	585 ± 20	26 ± 5
0	336 ± 19	570 ± 20	24 ± 5
0.2	38 ± 7	29 ± 6	1 ± 5
0.4	17 ± 5	8 ± 3	0.1 ± 1.1
0.6	10 ± 4	3.2 ± 2.0	0.1 ± 0.9
0.8	7 ± 3	1.7 ± 1.6	0.1 ± 0.9
1	5 ± 3	1.0 ± 1.4	0.1 ± 0.9

Table 2-6 shows the count rate recorded at different displacements. Note that the overall count has been split into energy windows. The first is chosen from 173keV – 534 keV to roughly contain the Compton Continuum, noting that he cut-off of 173keV is specified to remove spurious detector noise in the low energy range. The second window is chosen from 534keV – 753keV to contain the photopeak. The upper cut-off of the third window, 1276keV, is chosen to be roughly twice the energy of the main photopeak at 662keV, which is the maximum possible energy should two photons interact with the detector coincidentally.

Looking at the values from Table 2-6 we see that again there is some electronic pileup. The count rates are lower than those for the 10mm slit (compared with Table 10–1 in Appendix II), as expected, since the geometry of the situation dictates that the source now 'sees' less of the detector. From a geometrical point of view one would expect this decrease to be of the order of 60% of the original count rates, since the slit is now 60% of the previous size. From this it can be seen that an improved resolution has been gained at the expense of count rate. The system now detects less radiation from the source, but the count rate of the ^{137}Cs source is high enough for this not to be a problem.

2.6.6 Further slit measurements relating to vertical displacement and horizontal distance of source to detector.

A typical core-sample to be analysed by the logger is stored in a 1m long tube with a 10cm diameter. To accurately analyse 1cm slices of the core it was necessary to understand the effect that the surrounding material would have on the spectrum. The core represents a distributed source, so it cannot be treated in the same manner as a point source. The next step was to consider it to be made up of an infinite collection of point sources and assume their effects to be additive and to obey the principle of superposition. First the effect that the position of a single point source (in this case our point-like ^{137}Cs source) has on the spectra was studied (sections 2.6.4 & 2.6.5). This will help to formulate the idea of a distribution of point sources outlined above.
In this section we describe more detailed measurements of the resolution of the 6mm and 10mm slits by instead taking profiles at a number of different (horizontal) distances behind the slits. Vertical profiles for the 6mm slit were taken at horizontal positions of 0, 7.5 and 15cm whilst vertical profiles for the 10mm slit were taken at horizontal positions of 4cm and 11cm. The measurement times varied depending on the activity of the measured spectrum, since when the source was out of the line of sight of the detector there was very little activity, as opposed to the situation when the detector was in the middle of the slit. Plots and tables of the data obtained are included in the appendices for reference. The reader is referred to the previous section for the data obtained with the source just behind (i.e. horizontal distance of 0cm) the slit.

Initial analysis of the results showed that the spatial resolution obtained for a 10mm slit with the source at a horizontal position of 0cm was ~ 1cm. While this satisfies the project requirements it is not fixed for all positions, it holds only for the measured horizontal position. As the source was moved away from the slit this resolution degraded to ~ 2cm at a horizontal position of 15cm. Immediately it can be seen that this is not desirable. With a 6mm slit this is improved to a resolution of ~ 0.75cm – well below the requirement, but at the expense of count rate. This also held for the source at a horizontal position of 0cm and will degrade as this distance increases. Overall the 6mm slit gave a spatial resolution of just over 1cm – which was within the project specification.

Table 2-7: Comparison of the maximum count rates for the 6mm and 10mm slits. The values are taken from plots and tables that can be found in the appendices.

Distance from slit (cm)	6mm slit plateau (cps)	10mm slit plateau (cps)	6mm/10mm
0	980 ± 30	1500 ± 40	0.6502 ± 0.0011
7.5	420 ± 20	650 ± 30	0.646 ± 0.003
15	210 ± 14	340 ± 18	0.622 ± 0.005

Table 2-7 shows a comparison of the maximum values for the 10mm and 6mm slits as function of source distance from slit. The ratio (6mm/10mm) gives an indication of the effect that the change in geometry has had, i.e. that the cost of this improved resolution is a reduced count rate. For the 6mm slit, count rates are lower than the 10mm slit count rates by a factor of ~ 0.64. This agrees with the 0.6 ratio expected from the change in geometry.

2.6.7 Further investigation of the 6mm slit

Having noted that the 6mm slit gives a much improved resolution, it was decided that further investigation was necessary. Measurements were repeated with smaller step intervals to gain sufficient data for a complete quantitative analysis of the 6mm slit profile. The complete dataset can be found in the appendices. Table 2-8 below shows a subset of this data, giving the total net count rate N, and the net count rates in the relevant energy windows, as a function of source position.

The new investigation produced more data points which produced steeper, better defined profiles (see Figure 2-17 and Figure 2-18). Figure 2-17 and Figure 2-18 below present plots of the data obtained in Table 2-8. Figure 2-17 is a plot of the total count rate N, and Figure 2-18 is a plot of the energy regions 173keV – 534keV (the Compton continuum) and 534keV – 753keV (the photopeak).

Table 2-8: Total net count rate N (and net energy window count rates) versus vertical position of source. Source is at a distance of 7.5cm from the slit.

Vert. disp. (cm)	173keV – 534keV	534keV – 753keV	N (cps)	Vert. disp. (cm)	173keV – 534keV	534keV – 753keV	N (cps)
-10	0.6 ± 2.0	-0.01 ± 0.9	1 ± 3	0.1	148 ± 12	262 ± 16	430 ± 20
-5	1 ± 3	0.3 ± 1.1	2 ± 3	0.2	149 ± 12	260 ± 16	420 ± 20
-4	2 ± 3	0.6 ± 1.2	2 ± 3	0.3	147 ± 12	256 ± 16	420 ± 20
-3	2 ± 3	1.0 ± 1.4	3 ± 3	0.4	138 ± 12	240 ± 16	390 ± 20
-2	1 ± 3	2.1 ± 1.7	6 ± 4	0.5	125 ± 11	208 ± 15	343 ± 19
-1.6	5 ± 3	3.1 ± 2.0	8 ± 4	0.6	94 ± 10	143 ± 12	244 ± 16
-1.4	6 ± 3	4.2 ± 2.0	10 ± 4	0.7	70 ± 9	100 ± 10	174 ± 14
-1.3	7 ± 3	5 ± 3	12 ± 5	0.8	45 ± 7	55 ± 8	103 ± 11
-1.2	8 ± 4	6 ± 3	15 ± 5	0.9	28 ± 6	28 ± 5	56 ± 8
-1.1	11 ± 4	10 ± 3	20 ± 5	1	19 ± 5	17 ± 4	36 ± 7
-1	13 ± 4	13 ± 4	27 ± 6	1.1	12 ± 4	9 ± 3	21 ± 5
-0.9	17 ± 5	20 ± 5	38 ± 7	1.2	9 ± 4	7 ± 3	16 ± 5
-0.8	28 ± 6	38 ± 6	69 ± 9	1.3	8 ± 4	5 ± 3	13 ± 5
-0.7	48 ± 7	80 ± 9	134 ± 12	1.4	6 ± 3	4 ± 2	11 ± 4
-0.6	69 ± 9	125 ± 11	203 ± 15	1.6	5 ± 3	3 ± 2	8 ± 4
-0.5	94 ± 10	170 ± 13	276 ± 17	2	3 ± 3	2 ± 2	5 ± 4
-0.4	116 ± 11	213 ± 15	344 ± 19	3	2 ± 3	0.9 ± 1.3	3 ± 3
-0.3	137 ± 12	250 ± 16	400 ± 20	4	4 ± 3	0.4 ± 1.1	2 ± 3
-0.2	146 ± 12	263 ± 16	430 ± 20	5	1 ± 3	0.3 ± 1.1	1 ± 3
-0.1	145.3 ± 12	263 ± 16	430 ± 20	10	0.3 ± 2.0	0.0 ± 0.9	0 ± 3
0	147.7 ± 12	261 ± 16	430 ± 20				

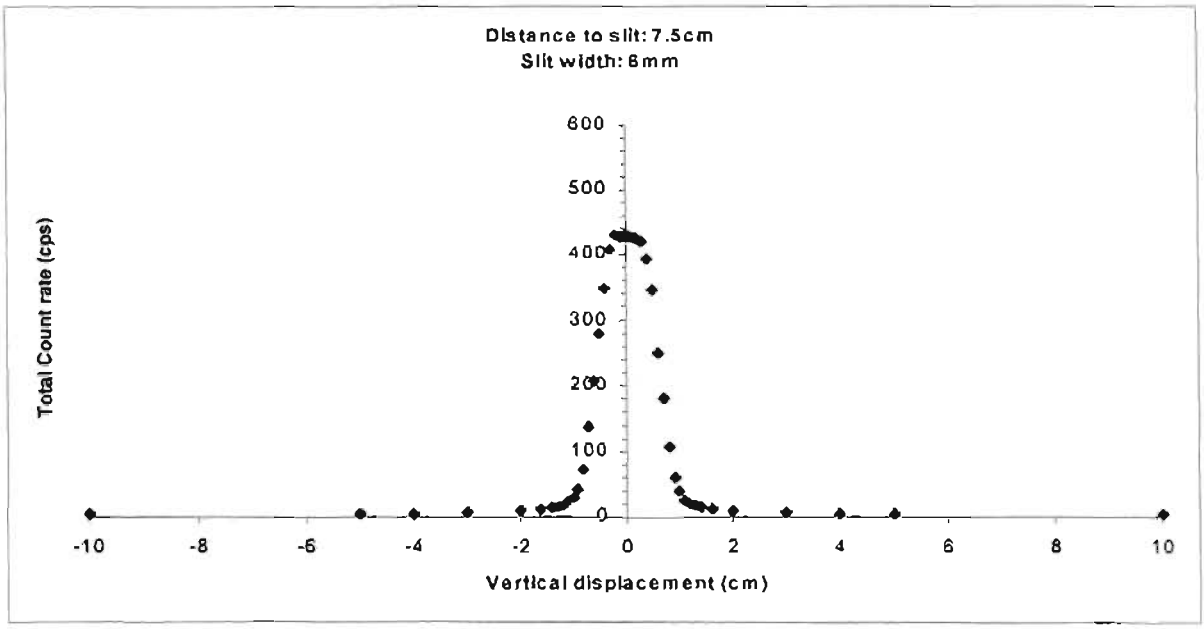

Figure 2-17: Vertical profile of total count rate of 6mm slit with the source at a distance of 7.5cm from the slit.

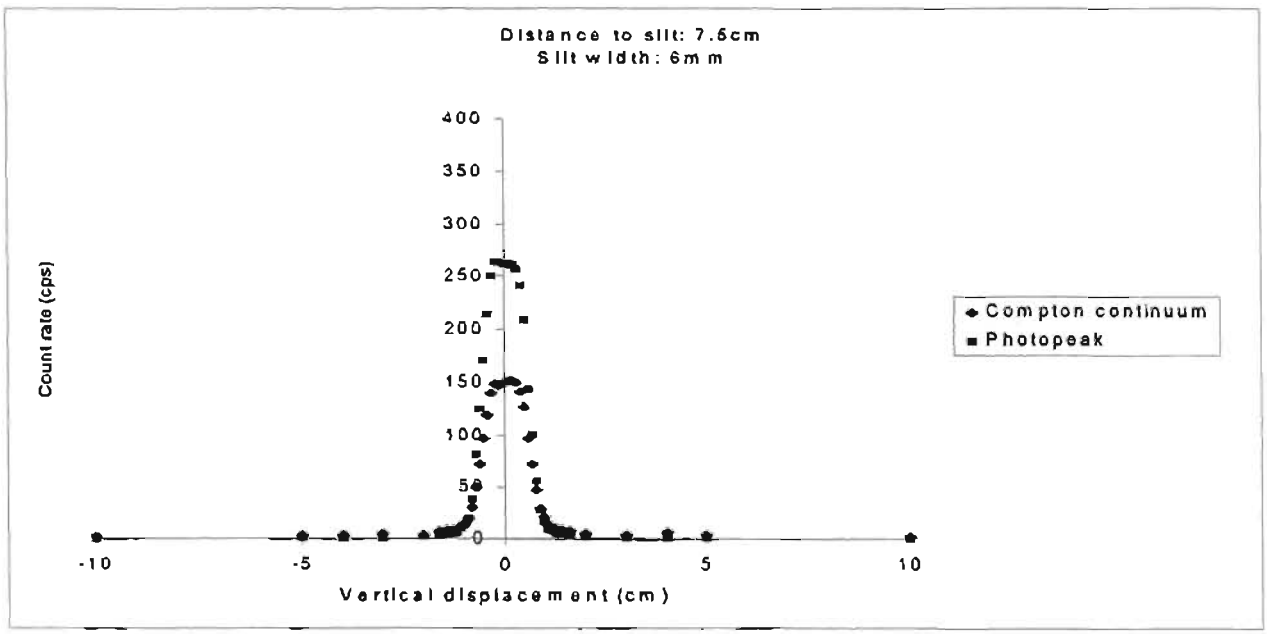

Figure 2-18: Vertical profile count rate for Compton continuum and Photopeak, with the source at a distance of 7.5cm from the slit.

From Figure 2-17 and Figure 2-18 it is possible to once again examine the FWHM of the 6mm slit (see Figure 2-21 below) and the steepness of the slit edges. Steepness (V) can be quantitatively measured if we consider the horizontal distance for the count rate to decrease from 90% to 10% of its maximum value. So

$$V = \frac{1}{(x_{90} - x_{10})}. \qquad (2.8)$$

Since the profile is approximately symmetric, the steepness of only the one side has been calculated. In the above Figure 2-17 for example, the 90% value is roughly 382.5cps and 10% is 42.5cps. Using these points the steepness is $V = 0.58\text{cm}^{-1}$, which represents a factor 2 improvement over $V = 1.38\text{cm}^{-1}$ from Figure 2-14.

Figure 2-19 shows how the steepness of the edges of the slit profile degrade as the source is moved further from the slit.

Thus the 6mm slit had both a steeper profile and a smaller FWHM than the 10mm slit. i.e. the 6mm slit should give a better spatial resolution. It will be shown that the FWHM also increases with distance from the slit.

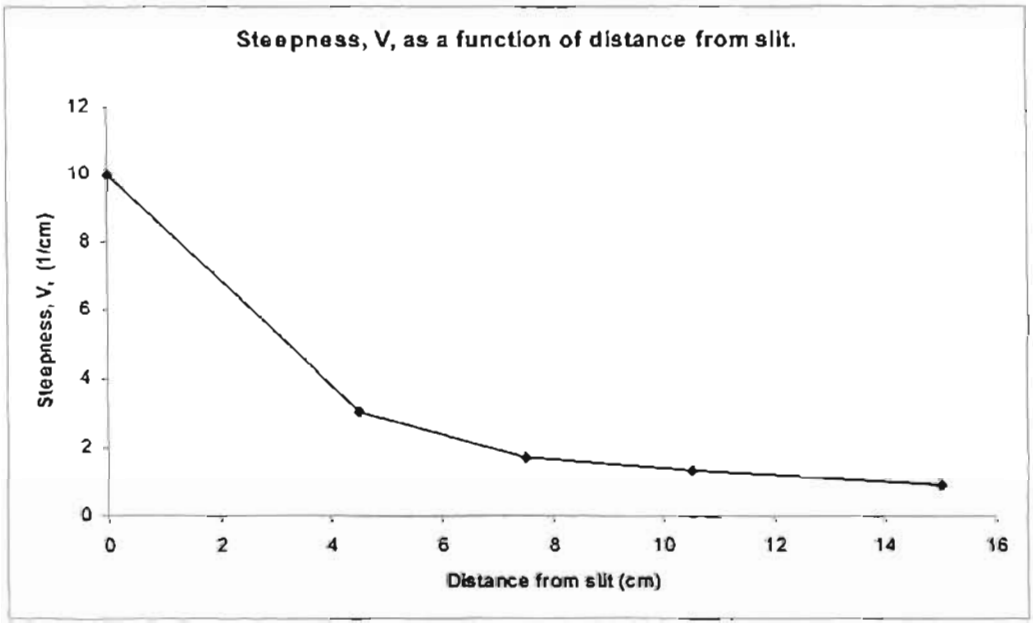

Figure 2-19: Steepness of the edge of the 6mm slit as a function of the distance from source to slit.

In Figure 2-20 the total count rate is plotted as a function of the horizontal distance between the source and the slit. This relationship should have the form $N \approx a \times r^b$, where it is expected that b ≈ -2. Note that the horizontal distances recorded in the tables are measured from the slit. However, an offset of 11cm, which includes the

lead thickness of 10cm and the distance of 1cm between the detector and the shielding, has been included in the plot.

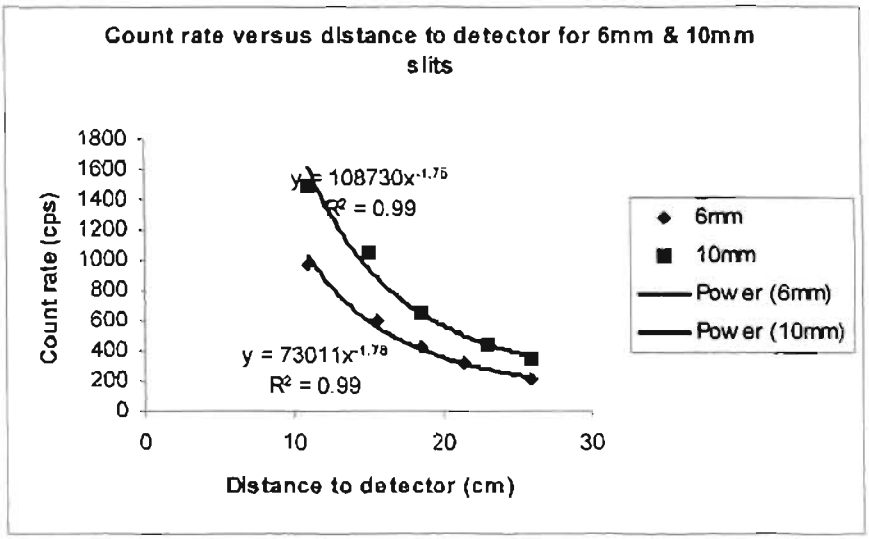

Figure 2-20: Count rate versus distance to detector for 6mm & 10mm slits with regression formulae superimposed on the data points.

Regression analyses on the data shown in Figure 2-20 with a power relationship of the form $N \approx a \times r^b$, yield values of $a = 108730cm \pm 330cm$, $b = -1.75$ for the 10mm slit and $a = 73010cm \pm 270cm$, $b = -1.78$ for the 6mm slit. The R^2 values for both these fits are close to unity, indicating a high level of confidence. The expected value of b ≈ -2 was not obtained though, and this may be accounted for by including a further offset. Given that the inverse square relation more correctly holds for r measured from the centre of the detector, and the fact that the detector face is a distance x from the lead block, then there should be a further offset included in the equation. The form can then be modified to $N \approx a \times (r + x)^b$. An alternative approach would be to fix the value of b at –2 and calculate x given a. Doing this yields a value of $x \approx 2.07$cm. This is an acceptable estimate for the distance between the centre of the crystal and the front face of the detector.

Next consider the FWHM of the slit profile as a function of the distance to the lead block. From Figure 2-17 and Figure 2-18 (and the data plots attached in the appendix) we can calculate the FWHM of the 6mm slit for total count rate N, and the two energy windows of interest, the Compton continuum and the photopeak. The

FWHM of N of the 6mm slit profile, as well as for the separate Compton and photo-peaks, are plotted as a function of horizontal distance from the slit in Figure 2-21.

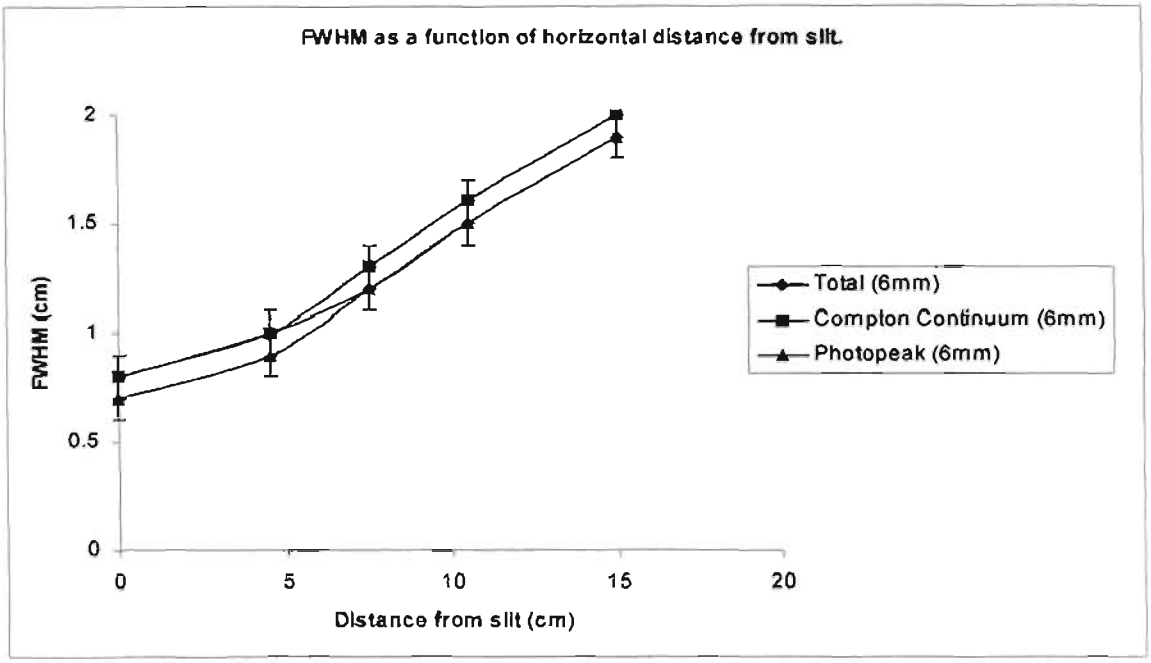

Figure 2-21: FWHM as a function of horizontal distance of source from 6mm slit.

It is interesting to note that the FWHM of the Compton peak is ~0.1cm less than that of the photopeak. As suspected, the FWHM increases with distance from the slit, with an average value of 1.3cm. In practice, the actual spatial resolution will not be equal to the FWHM, but may also be influenced by factors such as absorption in the core. This will be further discussed in subsequent chapters. Note that the resolution will also vary over the core diameter since it is a distribution of sources of varying horizontal positions. The plot also indicates that the Compton continuum is possibly attenuated less than the photopeak or total signal as the source moves further away from the detector.

Table 2-9 seems to support this, showing that the ratio of the maximum count rates in the Compton and photopeaks is approximately decreasing as the horizontal displacement increases. This trend is continued for all the points except the last one, which then increases again. It is not clear whether this point is anomalous and whether this trend actually exists or not. If it does exist the effect is still negligible with a change of approximately 0.12 in the ratio per 4cm horizontal increment.

Table 2-9: Ratio of the maximum values of the Compton continuum and photopeak peaks.

Horiz. Displ. (cm)	0	4.5	7.5	10.5	15
Photopeak	593 ± 20	369 ± 19	248 ± 16	194 ± 14	130 ± 11
Compton	349 ± 18	209 ± 14	140 ± 12	107 ± 10	75 ± 9
Compton/Photopeak	0.589 ± 0.003	0.566 ± 0.004	0.565 ± 0.006	0.552 ± 0.008	0.577 ± 0.012

This section began with a study of the effect of the slit width on the spatial resolution. For a 10mm slit it was found that the resolution was worse than the required specification of the project. A 6mm slit was then implemented which provided the required resolution. A comparison of these results showed that activity levels indeed scaled with the geometry changes (6mm activities being ~60% of the 10mm activity levels).

From the preliminary examination documented above, several aspects provide desirable results. The ratio between the Compton continuum and photopeak levels are approximately constant for the source at varying distances from the slit. The steepness and FWHM of the 6mm slit are superior to that of the 10mm slit, providing an acceptable approximation to that of a 'perfect' slit.

2.7 Conclusion

The goal of these experiments was to determine the functionality of the CsI detector with respect to its role in the core-logger system. This included a complete examination of the properties of the detector, beginning with energy resolution and eventually looking at the spatial resolution of different slit configurations, including background measurements with several layers of lead shielding present.

Background measurements were conducted and a background deconvolution function was obtained with a mass attenuation coefficient of $\mu/\rho=0.07$ (cm^2/g) by varying the lead shielding thickness. It may be necessary to return to this data and refine the calculations to include specific energy dependences. Specifically, the rate of decrease of activity displayed anomalies which are as yet unexplained (§2.5.3). In addition to studying the effect of the background, it was also necessary to determine

an optimal thickness for the lead shielding. From these studies it was concluded that a thickness of 10cm of lead provided adequate shielding while retaining practicality.

The slit investigation included a study of the behaviour of the slit pattern using an 'ideal' point source (^{137}Cs). Two slit widths were considered: 10mm and 6mm. Subsequent to an initial quantitative analysis of the 10mm and 6mm slit, it was decided that the 10mm slit would not satisfy the required spatial resolution of the core logger. Further detailed measurements were then conducted with a 6mm slit. These measurements used a more detailed profile to attain a better estimate of the slit resolution could be obtained.

The spatial resolution of the slit is closely related to its FWHM, which in turn is affected by the steepness of the edges of the profile. From the data obtained it is seen that the 6mm slit provides a profile with steep edges, hence improving the resolution. An ideal slit would provide a square shaped profile, having the same width as the slit itself. There are many factors preventing this from occurring in reality (such as scattering, absorption, reflection, background radiation, etc.) but the 6mm slit gives a good approximation of this ideal behaviour. The spatial resolution degraded as the distance between the source and the slit increased, but the average overall resolution was approximately 1.3cm. Similarly the steepness, defined as $V = \frac{1}{(x_{90} - x_{10})}$ degraded as distance increased, from a value of $\sim 1/4160 cm^{-1}$ to $\sim 1/171 cm^{-1}$.

In conclusion it must be stated that this simple rectangular slit configuration gave reasonable results and provides an acceptable alternative to designing a more complex slit. Using a slit width of 6mm the spatial resolution requirements of the project can be achieved. However this investigation was conducted using a ^{137}Cs source with a recorded activity of ~ 45μCi. In comparison to the activity of the natural radiation sources the core-logger is designed to measure, typically in the region of 33.8nCi, this is a very active source. Final conclusions can only be drawn after a study of the response using low activity sources has been conducted.

Chapter 3 :
Mechanical setup – System design and software

3.1 Introduction

The first phase concerned itself primarily with a feasibility study on some of the conditions required for the successful implementation of the core-logger. The main goal was to determine whether the spatial resolution of 1cm was in fact possible. Using a ^{137}Cs source and a Caesium Iodide (CsI) detector, it was confirmed that an average resolution of 1.3cm was possible, although this varied with distance from the collimating slit. The source had a high activity and was point-like, giving an optimal configuration for testing the resolution of both a 6mm and 10mm slit.

The study with the CsI detector included an examination of the background contribution in determining the initial configuration of the lead castle. A lead castle was constructed using an array of bricks and the effect of varying the thickness of the castle walls on the background was examined. Results from this led to the implementation of a 10cm lead castle, but also raised some questions about the contributing factors to the background spectra.

A secondary part of that chapter described the hardware and the philosophy behind the initial mechanical setup. This chapter describes the changes made to the overall mechanical setup, and the software used to drive the capture process. It should be mentioned that this chapter describes the early mechanical arrangement which may not necessarily be the configuration of the final core-logger.

3.2 Hardware

This section examines each of the components that makes up the entire system, explaining the design considerations. This will help to illustrate the evolution of the system as a whole and demonstrate the inter-dependency of the components. The general set up can be viewed as consisting of five distinct components, namely

- the system frame,
- the transport mechanism,
- the driving mechanism,
- data acquisition sub-system and
- the overall control mechanism.

3.2.1 System frame

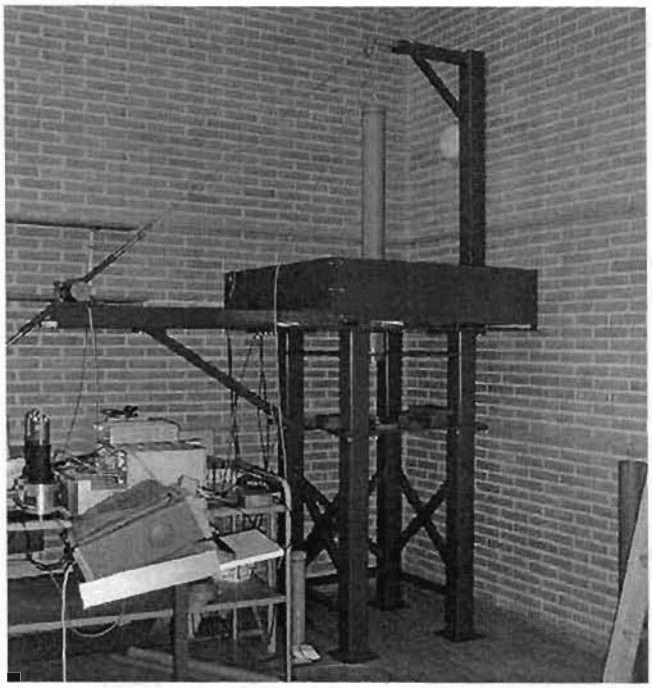

Figure 3-1: Current PHAROS system configuration

The frame was used to support the detectors (and their lead castles) as well as allowing the loading and transport of the cores. Given a specification of four detectors with associated castles, it was important that the frame be strong enough to hold a mass of up to four or five metric tonnes. There should be one platform for placing the detectors, and one for the possible future inclusion of a sub-system for measuring the density of the cores as they are moved through the frame.

Furthermore it should be easily accessible for loading and unloading cores. The transport mechanism runs the entire vertical length of the frame, and it is envisioned that cores will be loaded at the bottom and then hoisted upwards through the centre of the detector array. An important consideration here was the expected length of the measured cores. Certain design decisions required an assumption about this

parameter. In the current configuration, the height of the frame was selected to allow cores of 1m in length. Should the need arise to measure longer cores it would be necessary to re-engineer the frame. This adaptation could consist of an extension of the overhead arm used to hoist the core. Due to the modular nature of the design this should have no effect on the other components.

As can be seen from Figure 2-1 the frame included three levels and an horizontal arm for mounting the driving mechanism (see §3.2.3). There was also an overhead arm, which was used to mount the pulley required for the transport of the soil-cores (see §3.2.2). The top platform was used to hold the detectors and one of the lower levels may be used to set up a core density measurement system. The density meter will consist of a detector on one side of a core and a source on the other. The attenuation of the emitted radiation allows a measurement of the density of the core material. It can also be noted that below the bottom level a gap in the support beams allowed the loading and unloading of cores.

3.2.2 The mounting and transport mechanism

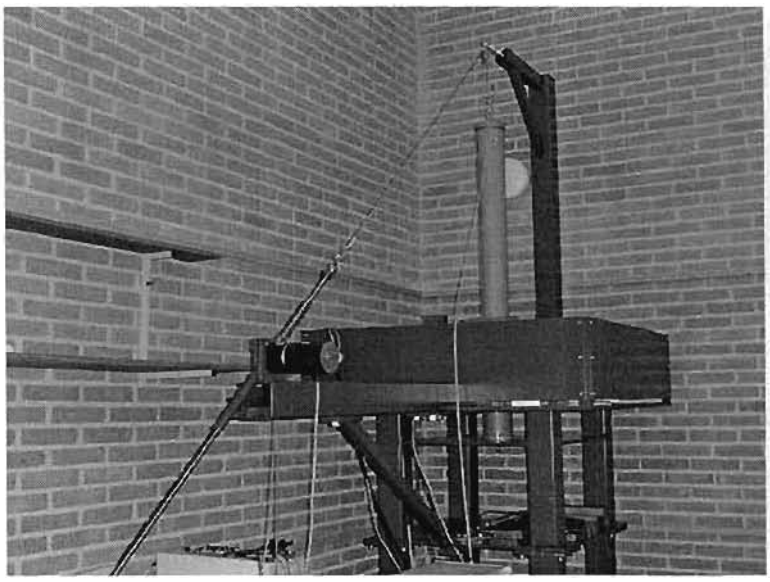

Figure 3-2: Illustration of mounting mechanism. The measured tube is placed inside the PVC tube shown here, and the lid is fastened on.

The primary driving mechanism for the system was a stepper-motor mounted at the end of the arm-beach attached to the frame. Coupled to the stepper-motor is a 2.3m long rack, which is translated by rotating a toothed gear attached to the shaft of the

stepper motor. A wire cable is used to connect the end of the rack to the core as shown in Figure 3-2. The soil sample was housed in a PVC tube which was then placed into a larger PVC tube with a removable lid. This lid was screwed in place once the core had been loaded, and a metal hook provided the means for attaching it to the wire cable.

This arrangement allowed the transportation of the cores through the square holes (15cmx15cm) as shown in Figure 3-3. At each of the holes a further guiding device was required to help keep the core centred and facilitate smooth movement through the frame. Several designs of varying complexity were considered. Eventually it was decided to implement this in the simplest manner by clamping rubber flanges at each hole.

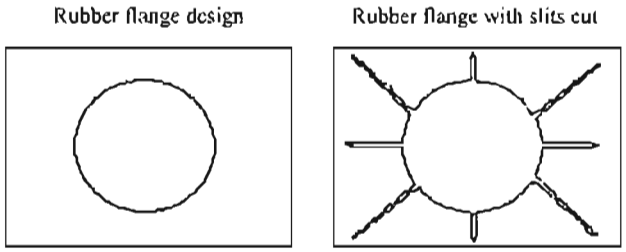

Figure 3-3: Rubber flanges used to guide the sore samples.

The rubber flange contained a circular hole, only slightly larger than the 10cm diameter of the measured cores. This setup proved to be slightly problematic. Initially the flange consisted of a flat piece of rubber with a circle cut into it. This retarded the movement of the core to a large degree resulting in noticeable errors in position. This was, to a certain extent, compensated by cutting slits into the rubber. With this adaptation the flange still guided the core through the centre of the frame, but imposed less friction on the core.

3.2.3 The stepper-motor

It was decided to use a stepper–motor for moving the core since it could be easily controlled via a PC interface. All position measurements were taken relative to an initial starting point, with a calibration factor of ~0.7 steps per mm.

The stepper-motor was controlled via a National Instruments Digital Acquisition (DAQ) PCI-6024E PC card which sent digital TTL pulses to the motor's controller interface card. The DAQ card was mounted in a PCI slot of the system PC and all I/O signals were terminated on an external connector board. (See Table 3-1 for a schematic of the available input/output pins on the connector board.)

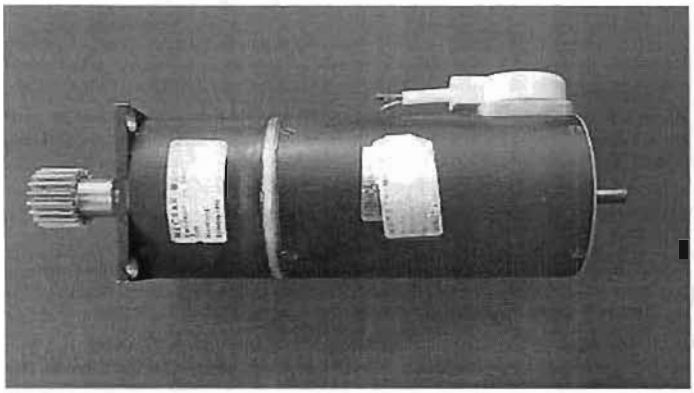

Figure 3-4: Snapshot of the stepper-motor used to drive the transport mechanism.

3.2.4 Data acquisition hardware

The National Instruments NI-DAQ card was used to achieve programmatic control of the stepper motor. This involved connecting the stepper-motor to its controller card and driving the card with TTL pulses from the general counters 0 and 1 on the NI-DAQ card. Given the extensive analogue and digital I/O capabilities of this NI-DAQ card it was originally also believed that it would be possible to use the card for the spectral data acquisition.

Table 3-1 shows the input, output and controller signals available on the card. It has 16 analogue input lines (0,..,15), two analogue output and 8 digital I/O lines. Additionally, the card supplied several timing signals for controlling the ADC conversion and other functions of the card. National Instruments also supplied a comprehensive software library for controlling the card's functions programmatically. Having 16 analogue input lines implied that up to 16 detectors could be monitored by the card concurrently.

Table 3-1: Lists the pinout configuration of the National Instruments NI-DAQ data card.

ACH8	34	68	ACH0
ACH1	33	67	AIGND
AIGND	32	66	ACH9
ACH10	31	65	ACH2
ACH3	30	64	AIGND
AIGND	29	63	ACH11
ACH4	28	62	AISENSE
AIGND	27	61	ACH12
ACH13	26	60	ACH5
ACH6	25	59	AIGND
AIGND	24	58	ACH14
ACH15	23	57	ACH7
DAC0OUT	22	56	AIGND
DAC1OUT	21	55	AOGND
RESERVED	20	54	AOGND
DIO4	19	53	DGND
DGND	18	52	DIO0
DIO1	17	51	DIO5
DIO6	16	50	DGND
DGND	15	49	DIO2
+5V	14	48	DIO7
DGND	13	47	DIO3
DGND	12	46	SCANCLK
PFI0/TRIG1	11	45	EXTSTROBE
PFI1/TRIG2	10	44	DGND
DGND	9	43	PFI2/CONVERT
+5V	8	42	PFI3/GPCTR1_SOURCE
DGND	7	41	PFI4/GPCTR1_GATE
PFI5/UPDATE	6	40	GPCTR1_OUT
PFI6/WFTRIG	5	39	DGND
DGND	4	38	PFI7/STARTSCAN
PFI9/GPCTR0_GATE	3	37	PFI8/GPCTR0_SOURCE
GPCTR0_OUT	2	36	DGND
FREQ_OUT	1	35	DGND

This arrangement was first tested by connecting the analogue output of a single Caesium Iodine (CsI) detector to the card and using a Caesium source (^{137}Cs). Unfortunately it didn't work as planned, and produced a spectrum where the incoming analogue pulses were discretised. This is a result of the manner in which the on-board ADC functions, which could only be triggered at a specific rate. A

sample and hold circuit would be required to capture the peak amplitude of the detector pulses. The NI-DAQ did not provide such a circuit.

It was subsequently decided not to use the NI-DAQ card for the data acquisition since its ADC circuitry did not include peak-hold circuitry. It was decided to revert to a more traditional data Multi-Channel Analyser which was coupled to a 16-input multiplexor, so allowing for multiple detectors.

After first testing this MCA and multiplexer configuration using borrowed equipment, it was decided to purchase a 16-input multichannel buffer (MCB) from EG&G Ortec. The MCB was connected to the acquisition PC via an Ethernet BNC network connection, allowing access from any PC on the same network. The multiplexor allowed up to 16 detectors to be connected which perfectly suited the requirements of the logger given an initial maximum of four detectors. This then allowed for future expansion.

The final set up for the logger using these chosen components is shown in Figure 3-5 below.

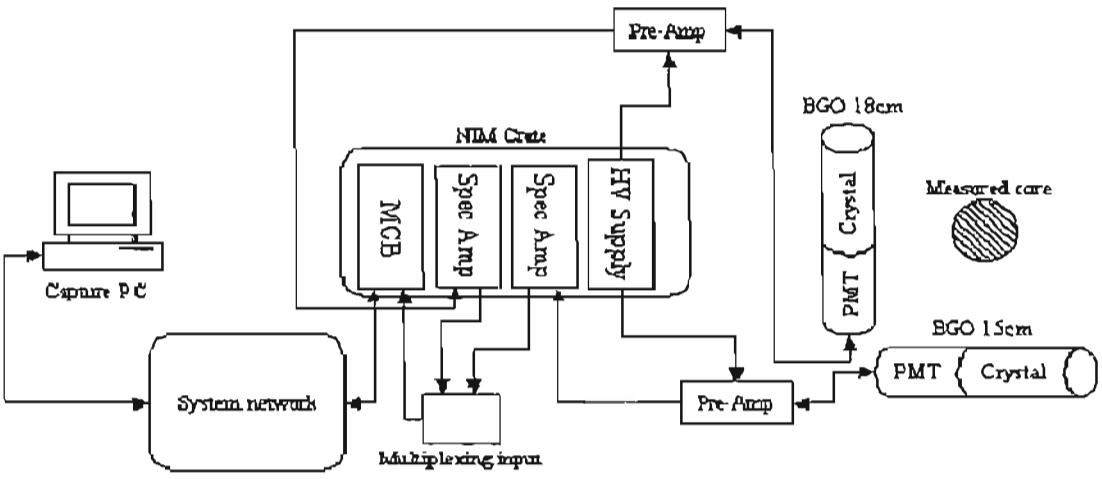

Figure 3-5: Schematic diagram of the set up of the data acquisition hardware.

Figure 3-5 shows schematically the layout of the hardware used. The HV generator supplies a DC voltage of 1.5kV to each of the detectors via the pre-amps. The pre-

amplifiers route the HT voltage to the detectors and receive signal pulses due to the gamma rays. These signal pulses are then amplified and sent to the spectroscopy amplifiers. Here the input pulses are shaped and further amplified before being received by the MCB. The MCB then communicated with the controlling (or capture) PC via the Ethernet network. All the components used were housed in a standard NiM crate, except for the HV generator which had its own separate 220V power supply.

3.3 Software

The software is considered here in separate sections. §3.3.2 covers the design and objectives of the software. §3.3.3 discusses the actual implementation of the design in §3.3.2 and the reasons for deviating from these objectives. A functional description of the actual software can be found in the appendices, along with screenshots of the user interface.

3.3.1 Requirements

There are several major requirements for the completed system. One of these is the need to automate the core measurement process. Initially almost all components were controlled manually using third party software. Cores were also measured in this manner, which was tedious and time-consuming. In-house software allowing for the required automation was therefore required.

The software needed to fulfil several requirements. It needed to control the movement of the core through the platform. This required information concerning the current status of data acquisition, i.e. was the system capturing data or had it finished measuring this core-slice? Using this information the software must determine when to start measuring, when to stop and then when to move the core to the next step. This therefore further required information concerning the position of the core which was used to move it to the next position. Furthermore, concerning the data acquisition, the software needed to exhibit informed decision making capabilities in terms of measuring times. Automation and improved resolution are not the only goals of the system. Another desirable property was the ability to measure cores much

quicker than conventional methods. By allowing the program the ability to intelligently determine the time needed to measure a single slice, based on the current level of statistics, the overall processing speed of a single core could be optimised.

3.3.2 Software design

The currently implemented software was essentially a batch process that handled several consecutive tasks repeatedly until any particular core measurement (or *run*) was complete. A run was considered complete once every section of the core had been analysed.

This process could be considered in several distinct steps.

- Step 1: Initialisation

Hardware and software parameters are initialised. The user is required to input any information needed to run the program (such as core name, core length, etc.). The time limit for the measurements can be specified, and there are also several parameters concerning the batch processes that need to be maintained. For example, several parts of the process are handled by external programs (or processes) that are spawned by the batch. The interaction between the PHAROS software and these processes needs to be carefully monitored.

At this point the PHAROS software also creates a data file that will be used to store the spectral data from each step in the core analysis. This data file is stored in a synchronised data file (sdf) format, which can be read and analysed by the Medusa Post Analysis (MPA) software. Note that once the file has been created it will be used to store all the data for the remainder of the run.

- Step 2: Acquire spectra

The program first checks the integrity of all the input variables, and having satisfied this criterion begins the process. The program then executes the Ortec GammaVision32 software, which runs automatically with a batch file and controls the data acquisition for a fixed length of time. The GammaVision32 software provides the interface and control of the acquisition hardware. A batch file is passed

to the software as a parameter, wherein the parameters of the capture are specified. Once the capture is complete, GammaVision32 saves the spectra to disk and exits, returning control to the PHAROS software.

- Step 3: Save data

At this point the PHAROS software saves the currently collected spectral data into the sdf-file created in Step 1. This is done by extracting the channel data from the spectra saved by GammaVision32, and converting the channel data into a format that is recognised by MPA. The converted data is then written into the sdf-file and saved to disk. Each detector has its own array of entries in the file which can later be separately analysed. Combining all detector spectra into a single file makes data control neater, and each loop in the acquisition process is saved as another entry into the same data file. Furthermore, this prevents complete data loss should the system crash during an acquisition.

- Step 4: Move to next slice

This is the final repeatable step in the loop. At this stage the software can now activate the stepper-motor and move the core to its next measuring position. The communication takes place at the PC interface via a National Instruments Digital Acquisition Card (NI-DAQ 6024E). This card sends digital TTL pulses to the external PC card that drives the stepper motor, where each pulse will result in one step of the motor. From here the execution returns to Step 2 and the process repeats until the entire core has been acquired.

Note that at this point in development the actual data analysis was still handled manually through the use of the MPA software. The PHAROS software produces a data file with the acquired spectra for analysis. An operator (or user) is then required to manually run the analysis on that file, producing the results and printing them. Note also that while third party software (GammaVision 32) is still included in the overall process, one of the goals of future development will be to integrate this functionality within the PHAROS software through use of the UMCB Programmers Toolkit which interfaces with the EG&G Ortec hardware device.

3.3.3 Implementation

The preceding section outlines the planned functionality of the program (as well as explaining the steps in a typical core-acquisition). This section has excluded the implementation of the software, hence avoiding an explanation of the problems encountered and not clarifying all the decisions made.

Firstly, note that the system requirements detailed in §3.3.1 are the objectives of the system and do not necessarily represent the current level of functionality. Software development can be unpredictable and it is not always possible to achieve the desired goals, and this section will explain the deviations from the required system and explain the function of the actual system. Detailed troubleshooting should be left for a more complete and more specific description of the software alone.

The system makes extensive use of third-party software in the form of the EG&G Ortec software GammaVision32. This package is specifically for use with EG&G hardware and is used to control the acquisition of spectral data. There are many features of the hardware related to spectral analysis which are of no interest in this project since they are aimed at a calibrated, high energy resolution system and generally refer to HPGe detectors. This sort of analysis is unsuitable for a BGO detector because of the poor energy resolution of the detectors, and the temperature dependent gain drift of the BGO signals made it very difficult to obtain a fixed energy resolution [1] – which is something the automated analysis relies heavily on. As a result, the GammaVision32 software is used purely for data capture. All communication with the device is handled by GammaVision32 and is transparent to the PHAROS software. This has some advantages. It means that PHAROS needs no knowledge of the acquisition hardware and doesn't need to worry about capturing the spectra. The major disadvantage of this set up is the use of the third party software, and the very fact that PHAROS has no control over the actual spectral acquisition. Removing this control from PHAROS means changing settings (such as measuring time, no. of detectors) is a cumbersome process and requires fairly extensive knowledge of the software. The use of the GammaVision software is the result of a trade-off between ease of use and ease of programmability. Initially it was hoped that

hardware control would be completely handled by the PHAROS program, which would remove the need for any third party software. This was to be done using the EG&G function library, the UMCB Programmer's Toolkit, which makes available to the software developer an array of functions that provide access to the MCB hardware. The system was originally designed and implemented around this library, but initial alpha versions of the PHAROS software were not stable and frequently caused the operating system to crash when calling the UMCB functions. The reason for these system crashes could not be determined, and with the pressing need for software that could automate PHAROS, it was decided to use the third party GammaVision32 to get a working model. The design and implementation of the software should then allow for future modifications to the program should the problem with the UMCB library be resolved.

3.3.4 Changing acquisition settings

The PHAROS software allows the user to adjust many of the settings used in the overall capture process. Most of these are environmental in nature (file paths, etc) or are related to the control of the stepper-motor. Acquisition is handled outside the control of the PHAROS program though, and as a result so too are the acquisition settings, the most important of these being the live time. Note here that PHAROS does allow for the user to set the measuring time and while it does not actually affect the measuring time in the GammaVision32 software, it is important to update this value when changing the external settings.

The operation of GammaVision32 is directed through the use of a .job file, which is passed to the gv32.exe file when it is executed by the PHAROS software. This .job file contains the information needed for the acquisition, directing the hardware and telling it for how long it needed measure. This also controls the for-loop that produces the separate spectra produced that are used for the MPA gain stabilisation [4]. Setting up the .job file is a fairly straightforward process, and the reader is referred to Chapter 9 of the EG&G Ortec GammaVision32 user manual, which contains a detailed explanation of the commands used in .job files. The skeleton of the .job file used for the PHAROS acquisition is fairly simple, and the structure of the file is shown in Listing 3.3-1.

```
SET_DETECTOR x
SET_PRESET_CLEAR
SET_PRESET_LIVE 1800

LOOP 4

REM ** CLEAR AND START EACH DETECTOR

SET_DETECTOR x
CLEAR
START

REM ** SET BACK TO FIRST DETECTOR AND WAIT FOR
FINISH
REM ** WHEN IT FINISHES SAVE THE SPECTRUM AND
EXPORT IT

SET_DETECTOR x
WAIT
SAVE "D:\somepath\spec_A_$(Loop1).spc"
EXPORT "D:\somepath\spec_A_$(Loop1).txt"

END_LOOP

QUIT
```

Listing 3.3-1: Outline of the source code of the JOB file used to run the PHAROS acquisition.

This shows the acquisition cycle for a single detector, and is easily expanded by replicating the code operating the detector and substituting different detector numbers in place of the variable *x*. The JOB begins by selecting the detector and clearing its current Preset Live Time (LT) setting. It then sets the new Preset Live Time and this

is the variable the user will need to change to adjust the measuring time of the acquisition phase. Note in the example above the Live Time is set to 1800 *seconds*, and this is looped four times to give a total measuring time of two hours. Once the LT's of all the detectors are set the loop begins, with the first action inside the loop being to clear the current spectrum of each detector, and then beginning the acquisition. Once each detector has begun to capture data the JOB file returns focus to the first detector and waits for it to finish.

Once the LT has been reached, the detector will stop acquiring data and control is passed back to the JOB file. This then saves the spectrum to the hard drive, with the path given being the location the PHAROS software will look for the saved spectra, and also exports the spectrum to text format. This process then repeats 4 times until the loop ends. Once the loop ends, the JOB file terminates the current session of GammaVision32.

Note that in a smooth run with one detector, the above process will produce 8 files, 4 half-hour spectra and 4 text files. The PHAROS software will look for these files in a specific location, and pauses execution of the acquisition loop until all the files exist. Once they are there the PHAROS software then picks up these files and moves them to the folder specified in the PHAROS settings by the user for the storage of the spectra, renaming them at the same time to reflect the name of the core being measured (Appendix VI Description of PHAROS Software).

When editing this JOB file the user must be careful to calculate the Live Times correctly, as well as properly specifying the save path of the measured spectra. Note that this path is not the same path shown in the Settings screen (in Appendix VI Description of PHAROS Software), and is hard-coded into the PHAROS program. This path is typically given by *$AppPath\Temp Spectra* where $AppPath represents the path of the pharos.exe file.

3.4 Stepper-motor control

As mentioned previously (§3.2.3) the control of the stepper-motor was handled via a PC interface card produced by National Instruments. The use of the PC card coupled

with visual interface software libraries allowed straightforward programmatic control of the stepper-motor from within a visual environment such as Delphi 4.0/5.0.

3.4.1 The stepper-motor interface

The NI-DAQ card is discussed in greater detail in §3.2.4 and this section will only include a general overview to demonstrate the relationship between all the components involved. This card is a Digital Acquisition card with a number of analogue and digital I/O lines as well as several control lines. The card has an on-board signal converter for converting both analogue and digital signals, as well as producing several timing outputs, two of which are used to drive the stepper-motor. The two outputs are digital (0V or 5V) and are used in conjunction to drive the motor. Sending a +5V signal on one line and a 0V signal on the other will drive the motor in one direction, and reversing the signals will drive it in the opposite direction.

The NI-DAQ card outputs TTL pulses to the stepper-motor control card. This interface/control card is connected to the GPCTR0_OUT and GPCTR1_OUT outputs of the NI-DAQ PC card, and to the stepper-motor via 3 output pins. The interface card is powered by a 24V/1.8A power supply and controls the stepper-motor via its 3 connections. The circuit diagram for the card is shown in Figure 3-6. There are a number of pins available on the card which allows for several configurations in terms of timing signals and external/internal impulse driving. Figure 3-6 below shows the configuration used for the PHAROS set up.

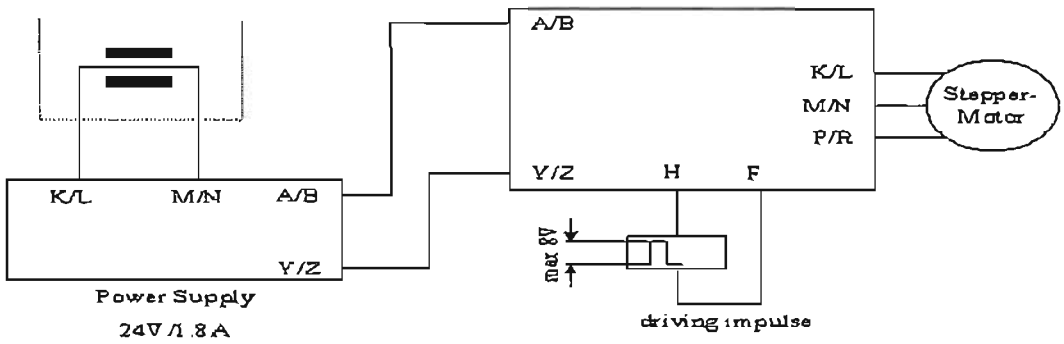

Figure 3-6: Stepper-motor and controller card configuration with external impulse control

The stepper-motor has three inputs that are connected to the K/L, M/N and P/R pins of the controlling card. These inputs are driven by the external impulse on the pins H and F. In the PHAROS instance, this external impulse is provided by the NI-DAQ PC card (pins 2 and 40) mentioned previously. As shown in Figure 3-7, the NI-DAQ card is seated in on of the PC's free PCI slots and it communicates with the outside world via its connector card.

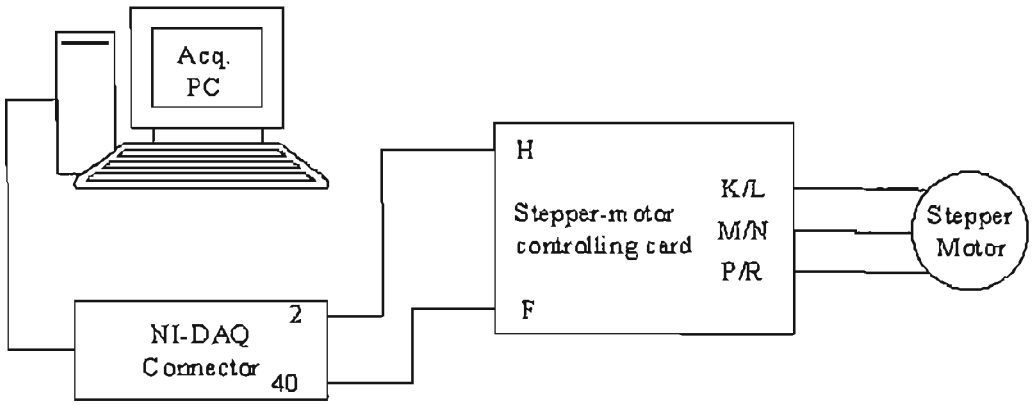

Figure 3-7: The control-chain for the PHAROS set up with the stepper-motor and its controller card

The connector card pins are shown in Table 3-1. As shown in Figure 3-7, pins 2 and 40 are used to connect to the stepper-motor controller card. These pins correspond to GCPTR0_OUT and GCPTR1_OUT respectively. The NI-DAQ card can be set to output a +5V signal on one of these pins and a 0V signal on the other, and this is the mechanism that drives the impulses and hence the stepper-motor. The timing of these outputs (GCPTR0 and GCPTR1) is controlled by several internal parameters on the NI-DAQ card. The two used primarily in the PHAROS instance are the combinations of Duty Cycle/Pulse Period and Pulse Width/Pulse Delay which control the pulses produced internally by the NI-DAQ card.

3.4.2 Calibration of the stepper-motor

The calibration of the stepper-motor was needed to provide the relationship between the number of steps and the distance travelled. This was essential in this application where the motor was expected to move the core up/down by a fixed distance. Initially, the motor was tested using different values for the Duty Cycle/Pulse Period to optimise the response of the motor at different speeds. It was found that the

stepper-motor seemed to have optimal movement (in terms of smoothness and regularity) for the following settings:

Duty Cycle = 0.09s

Period = 0.05s.

These settings that were used for the initial calibration were obtained by driving the stepper motor upward by a number of steps and measuring the distance travelled.

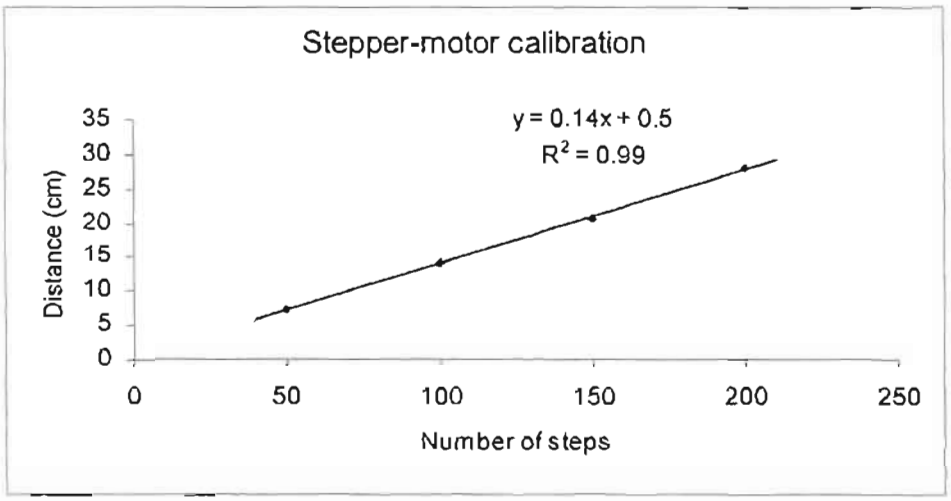

Figure 3-8: The plot of the data for the stepper-motor calibration. Included on the graph is the result of a linear regression on the data.

Figure 3-8 shows the calibration plot obtained for the stepper-motor. The plot only has 4 points, but the regressions indicates good confidence. The regression formula yields a value of 0.14cm ~ 1 step, or 1cm ~ 7.14 steps. This shows that the required slice thickness of 2cm does not correspond to an integral number of steps.

3.4.3 Repeatability tests

Having calibrated the core movement, it is important to test the repeatability and reliability of the calibration. This is done by repeatedly by commanding the motor to move 100 steps and then measuring the distance through with the core travelled. The results are shown in Table 3-2.

Table 3-2: Measurements to determine the repeatability of the stepper-motor movement

Average distance / 100 steps (cm)	14.0
Standard deviation (σ) (cm)	0.2

No. of Steps	Distance (cm)
100	13.6
100	14.1
100	14.2
100	14.1
100	13.8
100	14.1
100	14.3
100	13.9

Table 3-2 above shows that the core does not consistently move through the same distance of 14cm. From the calibration it is seen that 100 steps should be approximately 14cm, which is the average of the results in the above table.

3.4.4 Discussion of results

§3.4.2 and §3.4.3 describe the calibration and testing of the stepper-motor. One of the important requirements of the stepper-motor is to provide consistent, accurate movement of the core sample. The repeatability measurements in Table 3-2 indicate an uncertainty of 8%, it is worrying that this error is so large. The uncertainty should be ±1 step, i.e. 1%.

The calibration data shown in Figure 3-8 seems to be accurate and the regression coefficient R^2 demonstrates a strong confidence in the linearity of the relationship. However, there are only 4 points in the calibration and for these measurements a short (light) core was used and no frictional interference from the frame was experienced. Early tests showed that the rubber flanges retard the movement of the core, and that this does affect the overall motion, possibly because there is not enough tension on the hoisting cable when the core is moving down, or because the stepper-motor does not have enough torque when the core is moving up. Repeat

measurements with a longer core that crossed this flange boundary showed the distance moved was not consistent and the position of the core needed to be manually corrected when capturing data. To investigate this problem further, the repeatability test was done whilst alternating the direction of motion. The core was first moved up (through one of the flanges) by 200 steps (about 28cm) and then lowered by the same number and the initial and final positions compared. Table 3-3 shows the results. The initial position was taken as the 0cm reference point and the final position it was between 0.3 and 0.8 cm above it.

Table 3-3: Differences between initial and final positions of core when moving (~28cm) up and down to the same position.

Initial position (cm)	Final position (cm)
0	0.3
0	0.7
0	0.8

This test was also repeated but beginning with the core above the hole and moving it down and then up again, with results shown in Table 3-4.

Table 3-4: Differences between initial and final positions of core when moving down by 200 steps (~28cm) through the rubber flange and then back up again the same number of steps.

Initial position (cm)	Final position (cm)
0	-0.4
0	-0.5
0	-0.7

Comparing Table 3-3 and Table 3-4 it is interesting to note that the errors appear to be systematic in the sense that in each case the final position is either consistently above or consistently below the starting position. However, the limited data set makes it very difficult to draw any conclusions from this.

As mentioned above, the variability in the core position could be caused by a number of sources such as the insufficient tension in the cable or the limited torque of the motor. The stepper-motor could simply be missing steps when the flanges retard the

core movement. Further, there may also be a problem with *ramp-up* and *ramp-down* (acceleration and deceleration of the stepper-motor). Ideally, when started or stopped the stepper motor should be accelerated and decelerated in a gradual manner to relieve strain on the motor due to inertia of the transported object. This was not allowed for in the current PHAROS configuration when the stepper motor pulses were generated.

There does seem to be some difficulty in reliably moving the core from position to position. The solution to this problem is not clear and there are a number of possible design improvements which could be implemented.

(1) Another stepper motor with more torque could be installed.
(2) If it is confirmed that the rubber flanges are retarding the motion of the core, they could be replaced with rotating rubber rollers.
(3) A counter weight could be used (Figure 3-9). The translational force provided by the stepper motor would only be required to overcome the friction on the pulleys and not the weight of the core as well.

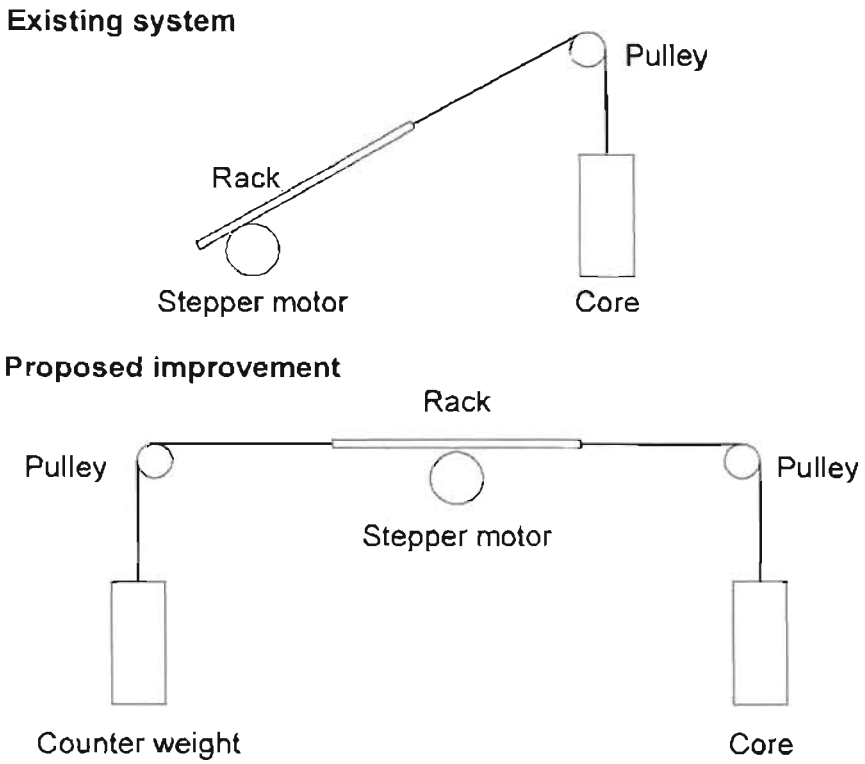

Figure 3-9: Proposed improvement to core transportation design.

(4) The stepper motor could be geared down. This would slow down the motion of the core, and care would need to be taken to avoid backlash.

(5) Alternatively, the actual position could be measured and assumed to be relative to the previous position of the core. An absolute position encoder (or shaft encoder) could be attached to the stepper-motor (or the core itself) and read into the PC system. This encoder would then provide accurate information regarding the actual distance stepped by the motor, allowing intelligent software to adjust the position as necessary. Assuming that the contact between the motor and the rack doesn't fail and that the rack moves constantly with the motor's steps, this could solve many of the problems. Moreover, the addition of a position encoder could in theory also compensate for any retardation in moving through the guiding flanges. The difficulties with the stepper-motor stem from the fact that the absolute position of the core is not known once it has been moved from its initial position. So it is possible that all these problems could be reduced (or even solved) through the use of a position encoder that could return the current absolute position of the core itself.

3.5 Conclusion

The previous method of radiometric analysis of cores involved manually cutting the core into slices (each having a thickness equal to the required resolution), and then measuring each section separately. This process is time consuming, labour intensive and furthermore results in the destruction of the sample core.

PHAROS aims to automate this process. This requires scanning of the full core by incrementally moving it through 2cm steps and at each step acquiring a spectrum. In its current configuration PHAROS has removed some of the tedium of manual analysis, but is not yet at the point of complete automation. There are some functions that PHAROS can handle, but it is still unable to automatically analyse and produce results such as ^{137}Cs profiles. At this point data acquired by PHAROS still needs to be processed off-line using the Medusa Post Analysis software.

PHAROS does, however, allow for the automatic acquisition of the required data. It can move the core without user intervention and acquire data (in MPA format) for each step. While the goal of complete automation has not yet been achieved, current

implementation certainly helps to reduce the time required to analyse a single core. The user can analyse data concurrently with data acquisition and leave the core intact. At this stage there are still problems with the current configuration. These difficulties lie with the software and the use of the stepper-motor. Firstly the PHAROS software is not yet complete. It uses third party software, which allows for some functionality at the expense of ease of use. This problem is primarily due to the failure to utilise the available UMCB Programmer's Toolkit that was provided by EG&G Ortec for controlling the hardware. Integrating this toolkit into the software is a primary goal for any future development of the software. Use of the third party software is also problematic in the sense that it introduces a higher likelihood of errors occurring. PHAROS cannot compensate for any errors caused by software outside of its control, and this compromises the overall stability of the system.

Furthermore, there are problems with position control of the core through use of the stepper-motor (§3.4). Movement is not consistent and problems have arisen that may be related to the overall mechanical design (e.g. possibly needing to redesign the guidance mechanism). A possible solution to this will be to implement a position encoder on the stepper-motor shaft. Currently movement and position readout forms an open-loop control system. All control decisions are made with no feedback as to the current state of the system. Implementing a position encoder would provide the necessary feedback to correct for any position errors.

A further goal of the system was to allow for a sub-centimetre spatial resolution. Unfortunately this has not been possible due to the nature of the sources and the low count rates. Currently the system achieves a spatial resolution of 3 - 4cm, which is still an improvement on existing core-logging systems. It is possible that more complex and advanced analysis techniques may allow for reduction of this resolution in the future.

In conclusion – PHAROS has progressed since its inception, but more development is required. Problems have been encountered, and where they have not been explicitly solved, analysis of the problems has led to the proposal of several possible solutions.

Chapter 4 :
Multiple detectors - BGO & CsI

4.1 Introduction

The first chapter on the progress of the development of PHAROS covered, in detail, the work done with a Caesium Iodide (CsI) scintillation detector [1]. This detector was studied extensively and used in conjunction with a point-like ^{137}Cs source to test the spatial resolution of slits built into the wall of the detector's lead castle. The primary objective was to test the feasibility of the spatial resolution requirement - i.e. to analyse a soil-core with a resolution of ~1cm. Results from that study showed this to be feasible under ideal conditions, and further testing remained to determine the effect of less desirable conditions. Moreover, the study with the CsI detector included an examination of the background contribution to the system as one of the determining factors for the initial configuration of the lead castle. The lead castle was constructed using an array of bricks (10cm×20cm×5cm and 10cm×10cm×5cm) and the effect on the background of varying the thickness of the castle walls was examined. Results from this lead to the implementation of a 10cm thick lead castle, but also raised some questions concerning the exact contributing factors with regards to the background spectra. The chapter was concluded without a definite explanation of the anomalies found in some of the results.

The data analysis and interpretation is only one part of the system development. Concurrent with the analysis a parallel development concerned the mechanical configuration of the system. The system construction was an ongoing evolving process, which was documented in the second part of the PHAROS reports, namely PHAROS – Part II [2] (Chapter 3 in this document). Chapter 3 showed that although the separate components worked in isolation from the others, the overall system automation was still incomplete. The software and the core movement were problematic, both related in part to control of the stepper-motor. The software also contained references to third-party applications, which reduced the stability of the automation, as well as creating a dependence on external systems. The stepper-motor

provided no way to accurately determine the position of the core at any given time, and this created all manner of problems during an automatic scan. Apart from re-engineering the software and removing the reference to third-party applications, use of a position readout device would go a long way to alleviating a lot of the problems. This could be implemented by placing an absolute position encoder on the core-logger, and it was hoped that this would solve the majority of the core transportation problems.

As mentioned previously, the final PHAROS system envisions using four detectors. The objective of the detector studies was to determine which type of detector would best suit the system configuration. The next step was then to install a MEDUSA-type detector, study it in a similar fashion to the CsI and compare them. For this purpose two Bismuth Germanate (BGO) detectors (one with an 18cm crystal and the other with a 15cm crystal) were installed in the setup and examined. For the most part, work done with one detector was repeated with the other. In this chapter reference will normally be made to a single detector, and unless otherwise specified the reader can assume the work was repeated for the other.

Once the BGO detectors were installed, it was possible to start looking at analysis techniques and data capture for the system as a whole. The MEDUSA Post Analysis (MPA) software was specifically designed for use with BGO detectors and, in addition to energy calibration, included automatic gain stabilisation routines. Although these factors were separately examined, use of the MPA software means that ultimately they will be accounted for during data capture and not the analysis stages. This then allowed for analysis of real data, and these initial results are presented at the end of this chapter.

4.2 Qualitative examination of BGO detector

As previously documented in Chapter 2, initial work in this project was undertaken using a Caesium Iodide (CsI) inorganic scintillation detector. The CsI was originally chosen for several reasons – not least of which was its ready availability. Moreover, the CsI represented a relatively cheap detector with similarly desirable properties to

the industry standard Sodium Iodide (NaI) detector. With a good energy resolution and reasonable efficiency it provided a good starting point for the PHAROS project.

Having established some familiarity with the system and its function, the next step would be to implement other detectors and to expand the detector array used. Further to this purpose, two Bismuth Germanate detectors were built into the set up. BGO detectors were selected because of their high efficiency (a desirable property in systems which monitor low-activity sources) and because of their close relationship with MEDUSA technology, on which the PHAROS system is based. The usefulness of this relationship will become more evident when the gain stabilisation and full spectrum analysis is discussed.

4.2.1 Experimental setup

The two BGO detectors were taken from MEDUSA systems. The cylindrical crystals were roughly 5cm in diameter, 18cm and 15cm in length, with similar functional principles to that of the CsI. Acquisition was done using an EG&G Ortec Multi-Channel Buffer (MCB) 920E. This particular device was accessed via a 10Base-2 network interface, and for these experiments third party acquisition software by EG&G (GammaVision 32) controlled the hardware.

The crystal was coupled to a photo multiplier tube (PMT), the output of which was amplified before being connected to the acquisition hardware. As can be seen from Figure 4-1 below, the pre-amp included an HV source which provided the required voltage for the crystal. The output signal of the PMT is fed back via the pre-amp to the spec-amp where it is amplified (to fit the 0V - 10V input range) and shaped. From the spec-amp the signal goes to an external multiplexing adapter. This adapter holds 6 BnC (or coaxial) inputs allowing for a maximum of 6 detector inputs, despite the MCB allowing for a total of 16 possible inputs. This external adapter contained no additional hardware and acts only as a connection converter, for which it was decided that initially only 6 inputs would be sufficient.

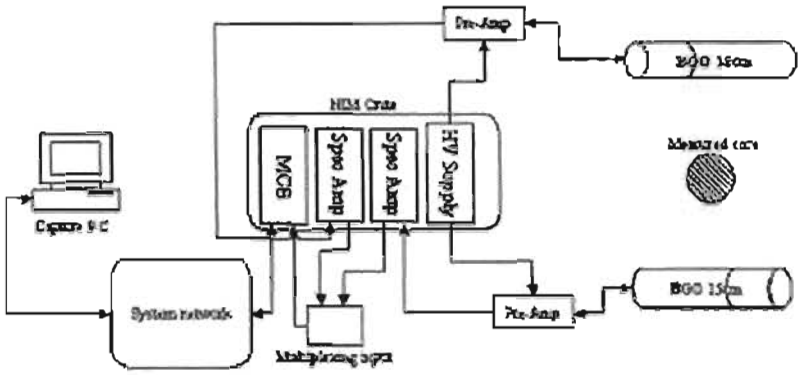

Figure 4-1: Schematic diagram of hardware set-up

The detectors were mounted on the frame opposite one another and at right angles to the CsI detector. Lead castles are constructed in a similar fashion to that of the caesium detector, with slits in the walls allowing unhindered penetration of the radiation originating from the central core.

4.2.2 Energy calibration

The energy calibration established the relationship between the amplitude of the analog pulses and the corresponding gamma ray energies. The detector output was an analog waveform, which was shaped and amplified and eventually converted to a digital pulse by an analogue-digital signal converter (ADC) that was integrated into the MCB. This digital pulse was proportional to the energy released by the incident photon in the crystal that caused it. This conversion factor correlates the pulse amplitude with the energy of the incident photons. For example, this implies that if the gain is calibrated such that channel 512 corresponds to 3.5MeV, then 1 channel represents an energy range of approximately 6.84keV. In general, the channel – energy relationship is unknown and a number of known energies need to be used.

To determine an accurate calibration curve, several sources with well-known and well-defined peaks were independently measured. The energies of the peaks in these spectra were then used as reference points for a regression analysis that yielded a general calibration formula for the detector. In principal the process is

straightforward given good sources and detectors with good energy resolution. In practise, however, this was not so straightforward, as is shown with this system.

An initial calibration using ^{238}U, ^{137}Cs and ^{232}Th gave seemingly good results. The low activity of the sources required measuring times of around two hours per source. For a more permanent calibration longer measuring times are required for better statistics, but for the initial purposes this was sufficient. The spectra used for the calibration can be found in Appendix IV.

4.2.3 Gain drift

The first calibration of the detector gives good results with all the spectra obtained for the calibration. The peaks from the sources were identified and located with a 1% uncertainty. The sources used were a ^{137}Cs source (with a single peak at 662keV), a ^{88}Y (Yttrium) source (with two peaks, at 898keV and 1836keV), and monazite, which contains ^{232}Th (with peaks at 583keV, 911keV and 2614keV).

Table 4-1: Calibration energies and channel numbers for the BGO 18cm detector calibration.

Source	Peak energy E (keV)	Channel #
^{137}Cs	661	370
^{88}Y	898	492
	1836	1016
^{232}Th	583	313
	911	515
	2614	1455

Table 4-1 above shows the calibration data obtained for the BGO 18cm using the aforementioned sources and the EG&G Ortec software (GammaVision32) to control the hardware and capture the data. The same software was used to perform the calibration, and provided a second order polynomial regression analysis to yield a calibration formula:

$$E(keV) = 1.06 \times 10^{-5} * channel^2 + 1.78 * channel + 12.2. \qquad (4.1)$$

The calibration was then tested against the spectra used for the calibration and their energies were calculated with an average error of 1%.

Table 4-2: Comparison between actual peak energies and energies found by analysing the calibration spectra with the resultant calibration data.

Source	Peak energy (keV)	Calibrated energy (keV)	% error
^{137}Cs	661.62	663.32	0.26
^{88}Y	898.02	898.84	0.09
	1836.01	1837.41	0.08
^{232}Th	583.14	584.90	0.3
	911.07	911.34	0.03
	2614.47	2615.55	0.04

Table 4-2 shows the comparison between the actual peak energies and those given by the calibration curve (eqn 4.1). As can be seen from the table the results are all very close to the actual values, with a % error of <1% in all cases..

The calibration was then used with several background spectra. At this point it was found that in fact the calibration did not work as well as expected. Some peaks were identified erroneously and others were identified with a greater than 10% error in the channel position. At first it was believed that there may have been an error during the calibration procedure. Calibrations were then repeated several times, with different sources and more identifiable peaks. Again, seemingly good results were obtained, but when trying to analyse other spectra the errors were unacceptably large. It was then suspected that the temperature dependent gain drift of the BGO detector was causing difficulties in the measurement.

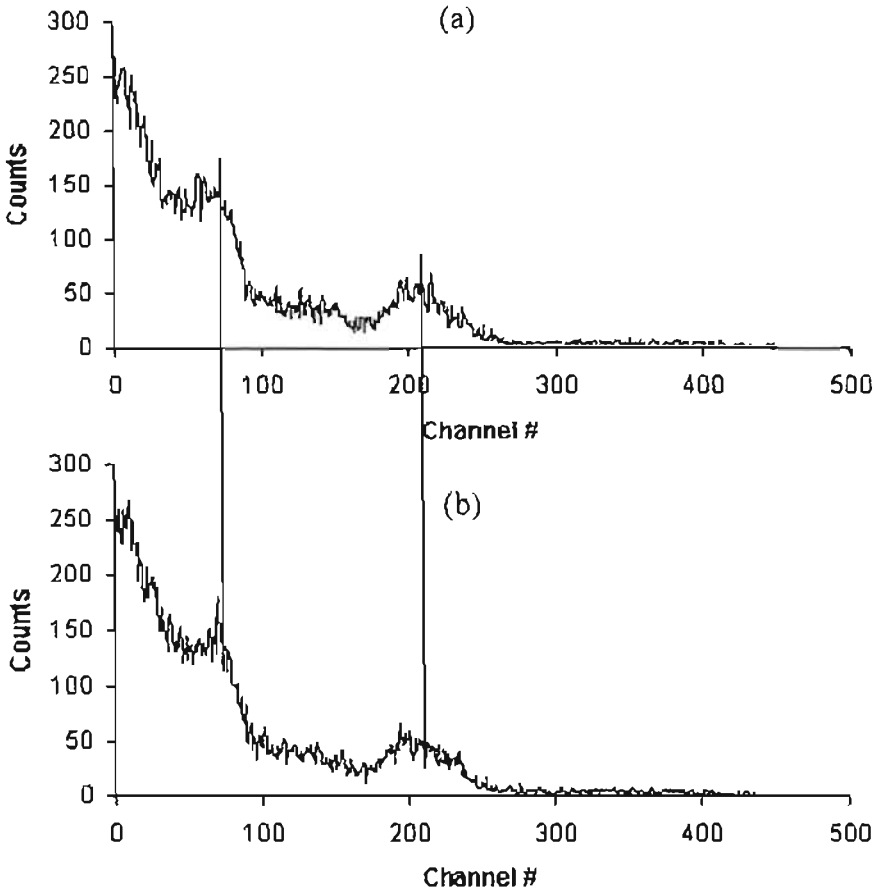

Figure 4-2: Spectrum of ^{137}Cs core measured using BGO 18cm detector. The spectra were both measured on the same day, 14/04/2000 within 7 hours.

Figure 4-2 illustrates the gain drift of the BGO detector. These spectra were measured using a ^{137}Cs source core on the BGO 18cm detector at different times on the same day. There is clearly a discrepancy in the peak position(s) shown. The sum peak at channel #210 in Figure 4-2(a) is positioned at channel # 200 in Figure 4-2(b). This drift is suspected to be a result of temperature effects, but in the past has also been attributed to PMT fatigue [7]. This effect was minimised by using the on-line gain stabilisation routine outlined below.

4.2.4 Gain stabilisation

This drift demonstrated in Figure 4-2 when using a fixed calibration curve would make the identification of the peaks extremely difficult. To correct for this it was necessary to introduce a gain stabilisation routine that will allow compensation. The

standard Medusa Post Analysis software included an on-line gain stabilisation routine that was specifically designed for use with BGO detectors [4].

The gain stabilisation works by using standard spectra to calculate activity concentrations and expected peak positions. These standard spectra are created using the routine outlined in §4, and for this application were not re-measured, but were taken from a previous BGO calibration in a bore-hole geometry [4]. A particular set of standard spectra gives a fixed relationship between the channel number and energy for a particular BGO detector, whereas in general, measured spectra will have an energy/channel relationship that varies with time (this is seen from the spectra above).

The stabilisation procedure makes use of a mapping function, $i = m(j)$ to correlate the channels j of the measured spectrum S with the channels i of the stabilised spectrum S^*. The contents of a channel of the measured spectrum S_j can then be distributed over a range of channels i determined using eqn. (4.5) and the mapping function m.

The mapping function $m(j)$ is not fixed and needs to be adjusted over time as the drift changes. As long as the gain changes are small enough these adjustments can be calculated from the differences between the current stabilised spectrum S^* and a model spectrum P. The model spectrum is determined by calculating the activity concentrations from S^* using the detector's standard spectra. These concentrations are then used with the standard spectra to calculate the model spectrum P which is then compared to S^*. The naturally occurring peaks in each spectrum will be slightly offset from each other. Figure 4-3 shows the difference between a stabilised spectrum S^* and the model spectrum P. The energy displacement r_i at channel i is given by

$$r_i = \frac{S_i^* - P_i}{P_{i+1} - P_i} \tag{4.2}$$

which can be seen in Figure 4-3. Now if the gain drift is linear with energy, then the shifts r_i will be linear with channel number i. The overall shift s between the stabilised spectrum and the model spectrum can then be taken as the weighted average

$$s = \frac{\sum_i w_i r_i / i}{\sum_i w_i} \tag{4.3}$$

where the best choice for the weighting factor w_i is given by

$$w_i = \frac{1}{\sigma^2(r_i / i)} \approx \frac{i^2 (P_{i+1} - P_i)^2}{P_i}. \tag{4.4}$$

With the shift s calculated, the function $m(j)$ can be adjusted and then applied to the next measured spectrum. In this manner the gain drift can be compensated, as long as the change between spectra is not too rapid.

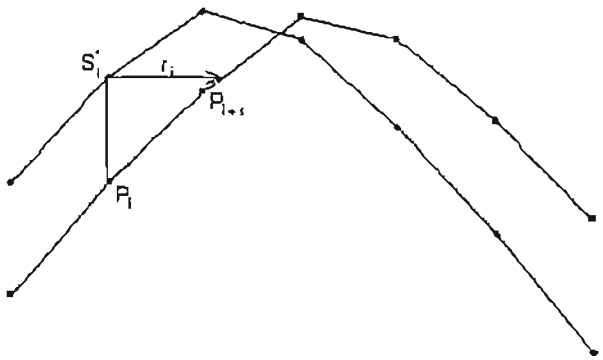

Figure 4-3: Calculation of energy shift r_i at channel i between stabilised spectrum S and model spectrum P [4].

Having determined a mapping function m, the contents of the channels of the measured spectrum S can then be redistributed over the channels of the stabilised spectrum S^* using [4]

$$S_i^* = \sum_{m(j+1)>i}^{m(j)<i+1} \frac{\min(i+1, m(j+1)) - \max(i, m)j))}{m(j+1) - m(j)} S_j. \tag{4.5}$$

This works by first mapping the channel positions j for measured spectrum S to the corresponding positions i of stabilised spectrum S^*. The contents of S_j are then distributed over a range of channels i to determine the stabilised spectrum. One direct consequence of this method is the loss of resolution in the mapping, the maximum of which will be half the channel width of either spectrum. It is therefore necessary then to use as large a number of channels as possible to make this loss of resolution small enough relative to the resolution of the detector.

Note that use of the automatic gain stabilisation routine as outlined above requires certain system information, such as activity concentrations, which in a classical windows analysis would call for an accurate detector calibration. At first glance this

seems to be a rather convoluted cycle with no independent parts making it almost impossible to determine the calibration, and hence analyse spectra. In reality, this process takes several iterative steps (some of which are outlined later in this document) and sub-steps which are all related and at each stage further refine the quality of the results. The use of the MPA software with the on-line gain stabilisation and spectrum analysis removes the need for determining a traditional detector calibration. Instead, it relies on determining standard spectra for each detector (see §4.4) and then uses the standard spectra to stabilise incremental BGO spectra and calculate activity concentrations. It is therefore possible to disregard the problem of explicitly determining an accurate energy calibration. As long as the standard spectra are well-defined and accurate they will already contain the information required to determine the peak-energy relationship.

4.3 The background problem

As in all experiments concerning radiation detection and spectrum analysis, determining the contribution to the spectrum due to extraneous sources is an important part of the process. Background radiation can be defined as being the response of the detector when there is no source present. In this core logger application the background has an especially important role since the low levels of radiation in the core sample are comparable to that of the background. As previously reported (Chapter 2) some time was spent in an effort to determine the exact composition of the background [1] for the CsI resolution measurements, and a similar investigation was carried out here.

4.3.1 Background measurements

Initial background measurements were taken over single, long time intervals. This approach, while yielding good statistics in terms of count rates, did not provide useful information for analysis. The gain drift of the detectors, especially overnight when there was a more substantial drop in temperature, made the measured spectra inappropriate for use in any analysis. As described in section §4.2.3 this drift made it very difficult to establish a reliable calibration for either of the detectors and steps had to be taken to counteract its effect.

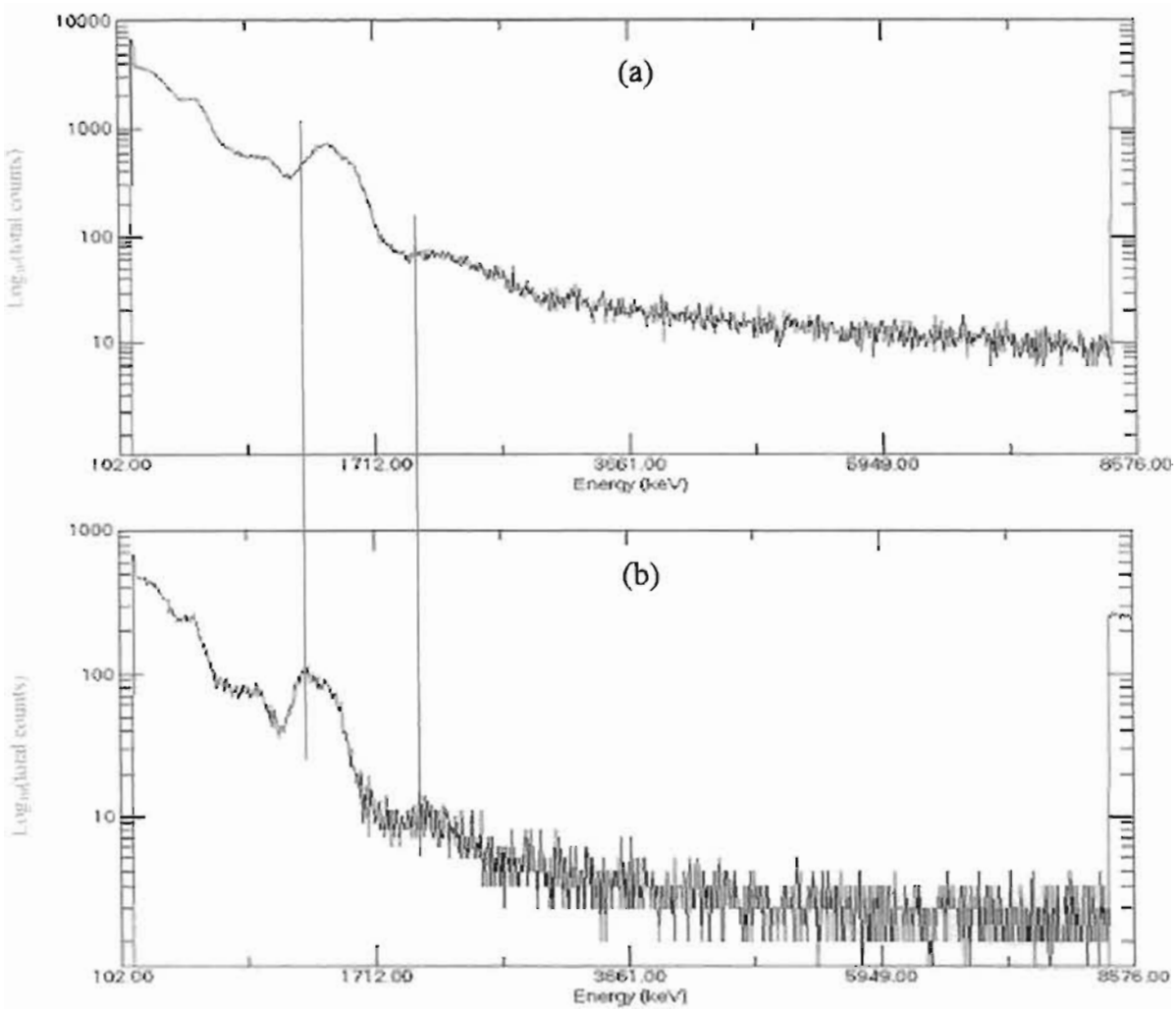

Figure 4-4: Background plots as illustrating the effect of the gain drift.

(a) The background measured with the BGO 18cm detector on 28-01-2001.

(b) The background measured on the same detector on 01-02-2001.

Figure 4-4 illustrate the effect of the gain drift on the recorded background spectra. These were recorded with the same detector, 4 days apart and both represent fairly long measuring times, of ~38hrs and ~4.7hrs, respectively. The spectra have the same energy calibration and clearly it can be seen that the background peaks do not correlate. For example, the peak shown in Figure 4-4(a) at ~1600keV is shown at ~1500keV in Figure 4-4(b).

After identifying the problem of the gain drift it was decided to compensate by measuring the background contribution in half-hour intervals. A half-hour interval

was selected because in the laboratory environment the temperature could be assumed to be approximately constant over these periods of time. These spectra were then used as input to the Medusa Post Analysis (MPA) software. These analysis tools were used for analysing the spectra using Full-Spectrum analysis techniques (see §4.4.2) and, more importantly in this case, they integrate an on-line detector gain stabilisation.

4.3.2 Self-radiation of BGO

To understand the background structure, it was important to consider each of the possible contributing factors. What affects the background measurement and where does it come from? Further to this, it was also important to bear in mind the general definition of background radiation: the response of the detector (or the signal measured) when there is no source present.

The first, most obvious possible contribution to the background is cosmic radiation. Cosmic rays contribute to the background in several ways [7]:

1. Prompt background pulses which are time coincident with primary cosmic particles. These high-energy charged particles increase the continuum background at all energies by Compton scattering.
2. Neutron background pulses, which are generated by induced reactions in high Z material (eg. Pb and Bi) and generate discrete γ rays.
3. Cosmic brehmsstrahlung arises when showers of secondary particles (protons, electrons and positrons) which are produced mainly in the detector's shielding and contribute to the lower energy regions of the background.

The effect of cosmic radiation was not looked at in detail in the work done for this chapter, but a more detailed description is given in further work described in [6].

There are further other possible sources of background radiation external to the lead shielding and detector. In general, here we consider contributions from elements such as ^{40}K, ^{137}Cs, etc. These are relatively low in energy, and should for the greater part be shielded by the 10cm of lead that makes up the detector castles.

Another possibility for consideration is a contribution from the lead bricks themselves. Radioactive impurities in the metal may produce detectable radiation, one example being the radioisotope ^{210}Pb which emits β^--particles and introduces *Brehmsstrahlung*. (Brehmsstrahlung is the process whereby decelerating/accelerating particles emit radiation. As the particle's velocity changes it will emit the lost energy in the form of γ-radiation.) This emitted β^- has an energy of 0.064MeV (and hence falls below the minimum energy level of interest) and the daughter nucleus is ^{210}Bi. This in turn has a half-life of 5 days and has a β^- decay with energy 1.163MeV, which may very well produce a noticeable effect in the considered energy range. The easiest way of determining the contribution by the lead was to measure a brick in isolation. To this end a single brick was placed in the lead castle of an HPGe detector and measured for approximately 24 hours. The result of this showed that the lead brick contributed very little to the background measured (< 0.5 counts per second) [6].

There is another source of background radiation that needs to be considered – and that is the fact that the detector itself may be contributing to its own background spectrum. Again this is determined by measuring each of the detectors separately in the HPGe detector.

Table 4-3: Activities in BGO detectors from HPGe measurements [6].

	^{40}K (Bq/kg)	^{207}Bi (Bq/kg)	^{214}Bi (Bq/kg)	^{214}Pb (Bq/kg)	^{232}Th (Bq/kg)
BGO 15cm	1.31 ± 0.17	0.026 ± 0.005	0.049 ± 0.014	0.039 ± 0.012	Below detection level
BGO 18cm	1.34 ± 0.11	0.200 ± 0.014	0.110 ± 0.003	0.17 ± 0.06	Below detection level

Table 4-3 shows the major activity contributions from the HPGe spectra. The ^{40}K comes from the photosensitive layer of the photo-cathode in the PMT (from literature on the Scionix website [9]), which accounts for the presence of the ^{40}K. The results also show that a substantial part of the background of the BGO 18cm crystal comes from the crystal itself in the form of ^{207}Bi (569.1keV and 1063.1keV and the sum peak 1632.2keV), ^{214}Bi (609.3keV and 1120.3keV) and ^{214}Pb (295.2keV). This self-

radiation contribution was not as strong in the BGO 15cm crystal but was also present.

Figure 4-5 shows the contributing peaks listed above in the BGO 18cm background spectrum. This spectrum was taken with the detector completely enclosed in its lead castle.

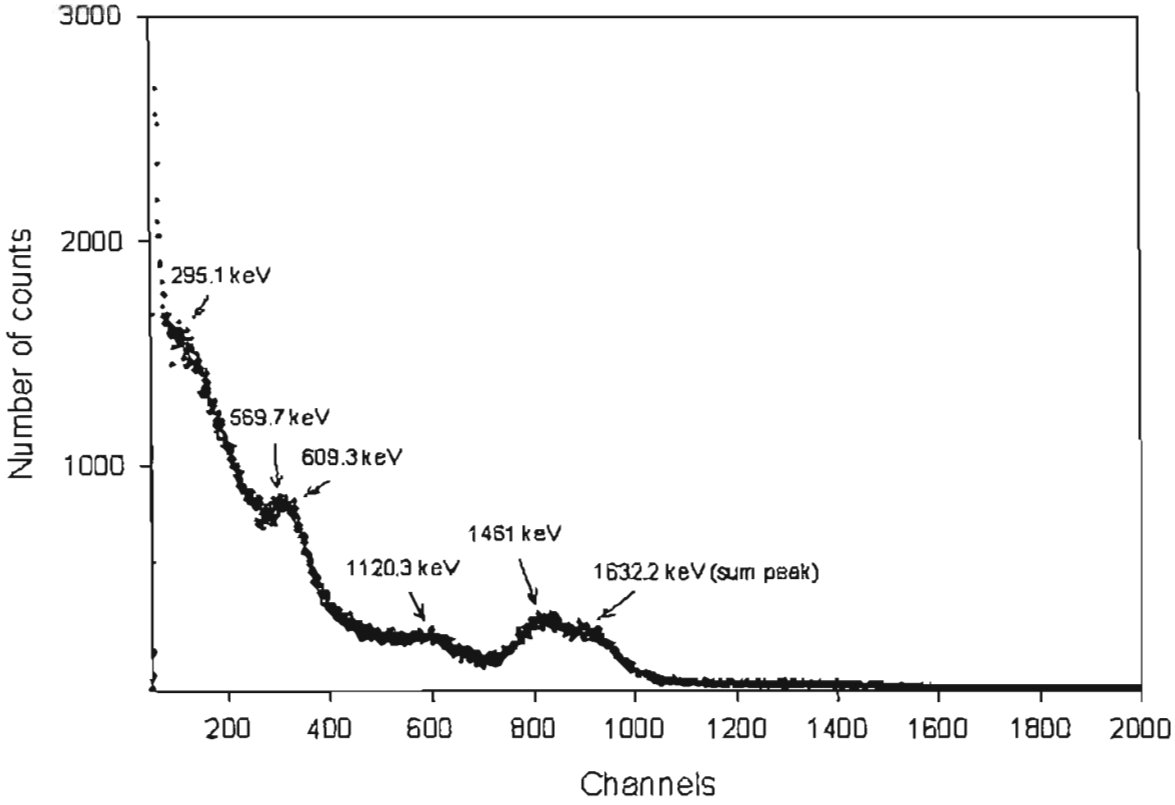

Figure 4-5: Peaks identified in the BGO 18cm enclosed background spectrum. (Figure taken from [6]).

4.3.3 MEDUSA vs. PHAROS

In the typical MEDUSA situation this self-radiation and background has negligible effect. The most common configuration (detector towed along the ocean floor) results in the detector seeing a large quantity of material (the floor below it) and comparatively little background (due to the low concentrations of K, Th and U in sea water and the shielding from cosmic radiation by the volume of water). Even in low activity cases this still results in a good signal-to-noise ratio, which in turn implies that the measured spectra are readily analysable and result in well-defined

concentrations. The Medusa Post Analysis software deals easily with this case in an automated fashion needing very little user intervention.

In the case of PHAROS this doesn't work quite as well. The major problem stems from the role reversal of the background and the signal to be analysed . Scanning a 10cm diameter core with a resolution of 1cm or 2cm means the detector sees much less material, and hence a very small signal. More particularly, when dealing with low activity sources, the signal is almost comparable to the background itself. This causes measurement problems, and makes resolving the background more important.

The results from the previous section showed that the greater part of the measured background comes from the detector itself, and as such cannot be reduced or excluded, thus limiting the gain achieved by trying to reduce the background. Previously the strategy involved improving the analysis by reducing the background – but this has proven impossible, hence a broader view is required to help solve the problem. One solution offers itself if the problem is viewed in terms of the desirable signal-to-noise ratio, i.e. high signal and low noise. If the noise cannot be reduced then an attempt to improve the signal must be made. The activity level of the material cannot be raised, so it is necessary to increase the volume of material the detector can see and hence widen the slit in the lead castle.

4.3.4 Discussion

In previous chapters, the importance of the background was described at length. The work done with the BGO has made this more evident and a direct consequence of this difficulty is that the slit needed to be widened. Measuring with a 6mm or even 10mm slit gave count rates only 50% - 70% above the recorded background making it very difficult to analyse the data. In addition this meant that measuring times would be very much longer than desired. With no way to reduce the background the only logical step was to increase the size of the slit and hence the volume of core material detected. Before beginning with the standard spectra (see §4) it was decided to open the slit to 20mm. This gave an acceptable count rate when measuring low activity sands (~12 counts per second for Ankersmit sand) while increasing the background by very little. Furthermore, while the 6mm slit provided a good spatial resolution

(approx. on average 9mm [1]), the 20mm slit could provide a resolution of ~ 30mm, which is still an improvement on most current systems.

4.4 Standard cores and standard spectra

The objective of the spectrum analysis in PHAROS is to determine activity concentrations of Uranium (^{238}U), Thorium (^{232}Th), Potassium (^{40}K) and Caesium (^{137}Cs). There are, in practise, two methods used for analysing spectra: peak (or window) analysis and full spectrum analysis (FSA).

Window analysis works by considering the net count in windows around peaks of interest. This is useful for analysing spectra obtained with the HPGe detector because of its excellent energy resolution. However, it must be noted that as a result of windows being used, only part of the information in the spectrum is actually used. Furthermore, because part of the spectrum is subtracted, the uncertainty in the results is also increased.

Full Spectrum Analysis takes the shape of the entire spectrum into account and attempts to resolve it into its radionuclide components (the standard spectra) and a background contribution. The energy resolution of the BGO is much worse than that of HPGe detectors, and hence its spectra are better suited to analysis using FSA.

4.4.1 Windows analysis

For windows analysis, activity concentrations are determined from the net content of the window around individual peaks. The concentrations of ^{40}K, ^{238}U and ^{232}Th are given by the following equations [5]

$$C_K = (n_K - \beta n_{Th} - \gamma(n_U - \alpha n_{Th}))/s_K, \tag{4.6a}$$

$$C_U = (n_U - \alpha n_{Th})/s_U, \tag{4.6b}$$

$$C_{Th} = n_{Th}/s_{Th}. \tag{4.6c}$$

In these equations the numbers n_K, n_{Th}, and n_U represent the counts for K, Th and U respectively. These numbers are taken from the respective peak windows and are detector and cosmic background corrected. Typically the counts within these

windows are measured and the background contribution subtracted. This will then yield the required concentration values to be used in the formulas in (4.6) above. Equations 4.6 also show that the C_K concentration contains contributions from both the ^{232}Th and ^{238}U spectrum. This occurs because the energy window of the ^{40}K spectrum sits at 1460keV, which is at a lower energy than the maximum ^{232}Th line at 2614keV. Similarly for the ^{238}U spectrum. Hence C_K contains the terms n_U and n_{Th}, and similarly C_U contains the term n_{Th}.

When considering low activity sources the background subtraction introduces large uncertainties since the background comprises a large fraction of the measured signal. In addition the uncertainty arising from the subtraction will compound the relative uncertainties. Further, it must be remembered that the windows analysis improves in accuracy for detectors with good peak resolution. An inferior peak resolution can have one of two consequences – either a wider window is used (which increases the uncertainty in the above equations) or a smaller signal is processed (resulting in a larger error in the background subtraction). The BGO detectors used have a poor resolution, which makes the use of windows analysis unacceptable, in particular when taking into consideration the low activity levels of the natural radiation sources in the core.

4.4.2 Full spectrum analysis

For Full Spectrum Analysis [5] the full energy spectrum is considered. From eqn. (4.7), the measured spectrum Y can be described as the sum of the (unit) standard spectra Xj multiplied by the activity concentrations for the individual radionuclides Cj. Y will also include a contribution from a background spectrum (BG). In principle the standard spectra are accurately determined and well-known, and the background is constant.

$$\chi^2 = \frac{1}{N-M}\sum_{i=1}^{N}\left[Y(i) - \sum_j C_j X_j - BG(i)\right]^2 / w(i) \qquad (4.7)$$

Equation (4.7) represents the least-squares approach to finding the optimal activity concentrations. In the equation, i represents the channel number (up to N channels), $w(i)$ is a weighting factor, the number of standard spectra used is given by M and the

value of χ^2 is an indication of the quality of the fit. The selection of weighting factors *w(i)* pose an interesting problem. In principle any set of factors should give a valid result (meaning the calculated concentrations yield the correct values) as long as they are sufficiently independent of the measured data. As a standard procedure weighting factors given by

$$w_i = \frac{1}{\sigma^2(Y_i)}, \tag{4.8}$$

are used (where the variances $\sigma^2(Y_i)$ are not known). Reliable weighting factors can be calculated in an iterative process by first replacing $\sigma^2(Y_i)$ in eqn. (4.8) above by the channel contents Y_i. These weighting factors are then used in eqn. (4.7) to obtain concentration values C_j^*. From these values, spectrum S^* is constructed,

$$S^* = \sum_j X_j C_j^* + BG, \tag{4.9}$$

which will have the correct ratios and can be used to determine the weighting factors given by eqn. (4.8). These w_i can then be used in eqn. (4.7) to obtain better estimates of the activity concentrations.

Standard cores are constructed (see §4.4.3 below) and from them the standard spectra (see §4.4.4 below) are calculated. A model spectrum is constructed by multiplying the standard spectra by the estimated activity concentrations. The model spectrum is compared to the measured spectrum, and the fit is tested using 2nd order polynomial regression. It is possible for the user to optimise the fit by adjusting the fitting parameters (a_0, a_1 and a_2) of the polynomial. These fitting parameters are the quadratic coefficients in the energy scale calibration. The resultant calculation is then compared to the physically measured spectrum, with the χ^2 value indicating the quality of the fit.

With an acceptable fit the expectation value $\langle \chi^2 \rangle = 1$. Acceptable values for χ^2 depend on the number of degrees of freedom and on the validity that all uncertainties are of a statistical nature. Therefore, $\chi^2 \approx 0.5 - 2$ should indicate an acceptable fit and the activity concentrations of the measured spectrum are then given by the concentrations of the model spectrum.

4.4.3 The standard cores

The method given in §4.4.2 works well given a well-determined set of standard spectra. These spectra are determined by calibrating the detector(s) in a specific geometry using materials containing natural radioactive components. The FSA analysis requires a standard spectrum for each of the nuclides of interest, ^{40}K, ^{232}Th, ^{238}U and ^{137}Cs. Four standard cores were constructed, each containing a dominant concentration of its respective radionuclide and each having approximately the same density.

Table 4-4 shows the materials used for each of the required nuclides. Note that for optimal results each standard sample should be completely orthogonal to the others as far as radiometric composition is concerned. In practice this does not happen, since each of the materials used contain some concentrations of the other nuclides. Each of the source material components were mixed with ankersmit sand (a grain-size classified, low activity sand from the eastern part of the Netherlands, purchased from Ankersmit), and a fifth core of pure ankersmit sand was constructed for use as a background core.

Table 4-4: Material (and masses) used for construction of the standard cores.

Radionuclide	Source material	Mass of material used (g)	Mass of Ankersmit sand used (g)
^{40}K	Potassium chloride (KCl)	398.8	4613.0
^{232}Th	Monazite	10.9	4990.0
^{238}U	Zircon	161.10	5015.0
^{137}Cs	Caesium-rich sand (originating from the beaches of the Irish sea north of Sellafield).		

The standard cores reflect the geometry of the final set up, and were created as cores with a length of 30cm and a diameter of 10cm. The contents of each core were chosen such that the concentration of a specific nuclide would be maximised per core, and the contributions from the other nuclides minimised. Their activities are determined by measuring representative samples from each core on an HPGe detector. The results are listed in Table 4-5 below.

Table 4-5: Activity concentrations (in Bq/kg) of the standard cores used to create the standard spectra for the core-logger.

	^{40}K (Bq/kg)	^{232}Th (Bq/kg)	^{238}U (Bq/kg)	^{137}Cs (Bq/kg)
Ankersmit sand + KCl	1310 ± 7	2.90 ± 0.10	3.04 ± 0.08	< 1.5
Ankersmit sand + monazite	105 ± 10	501 ± 7	84.0 ± 1.0	< 1.5
Ankersmit sand + zircon	89 ± 6	103.4 ± 1.6	377 ± 3	< 1.1
Caesium sand	329 ± 20	14.0 ± 0.4	18.0 ± 0.3	124.0 ± 1.9
Ankersmit sand	104 ± 6	2.90 ± 0.08	3.42 ± 0.06	< 0.11

Table 4-5 lists the activity concentrations of the radionuclides of interest for each of the standard cores constructed. These activities were obtained by taking equal samples from each of the mixed cores and measuring them in an HPGe detector. From this table it can be seen, for example, that for the KCl core, the ^{40}K concentration is ~ 1300 Bq/kg (in the decay of ^{40}K ~10% branches via γ-ray emission), whereas the ^{232}Th, ^{238}U and ^{137}Cs concentrations are all < 5 Bq/kg. This indicates that the concentration of ^{40}K will dominate the measured spectrum for this core. This can be similarly seen for the other cores and their dominant radionuclides.

4.4.4 The standard spectra

The activity concentrations shown in Table 4-5 were used to set up a 5×5 total concentration matrix *A*. This is a square matrix containing the concentrations of the nuclides per core and an extra column and row for background values.

$$A = \begin{pmatrix} 1310 & 2.9 & 3.04 & <1.5 & 1 \\ 89 & 103.4 & 377 & <1.1 & 1 \\ 105 & 501 & 84 & <1.5 & 1 \\ 329 & 14 & 18 & 124 & 1 \\ 0 & 0 & 0 & 0 & 1 \end{pmatrix} \qquad (4.10)$$

In the matrix (4.10) the top row is the concentration values for each nuclide for the KCl core (as in Table 4-5), the second row for the zircon core, the third for the

monazite core and the fourth row for the caesium-rich sand core. The final column and final row represent the background contributions in the cores.

Given this matrix, the standard spectra can then be obtained from the following equation:

$$[\ CS\ ] = [A][\ X\ ] \tag{4.11}$$

Equation (4.11) shows the calibration spectra *CS* as the product of the total concentration matrix *A* and the standard spectra *X*. The calibration spectra are obtained by measuring each of the standard cores compiled and is the response of the detector *per second* to the known activity concentrations. The standard spectra (*X*), which represent the detector response to an activity concentration of 1 Bq/kg, were then calculated by a matrix inversion.

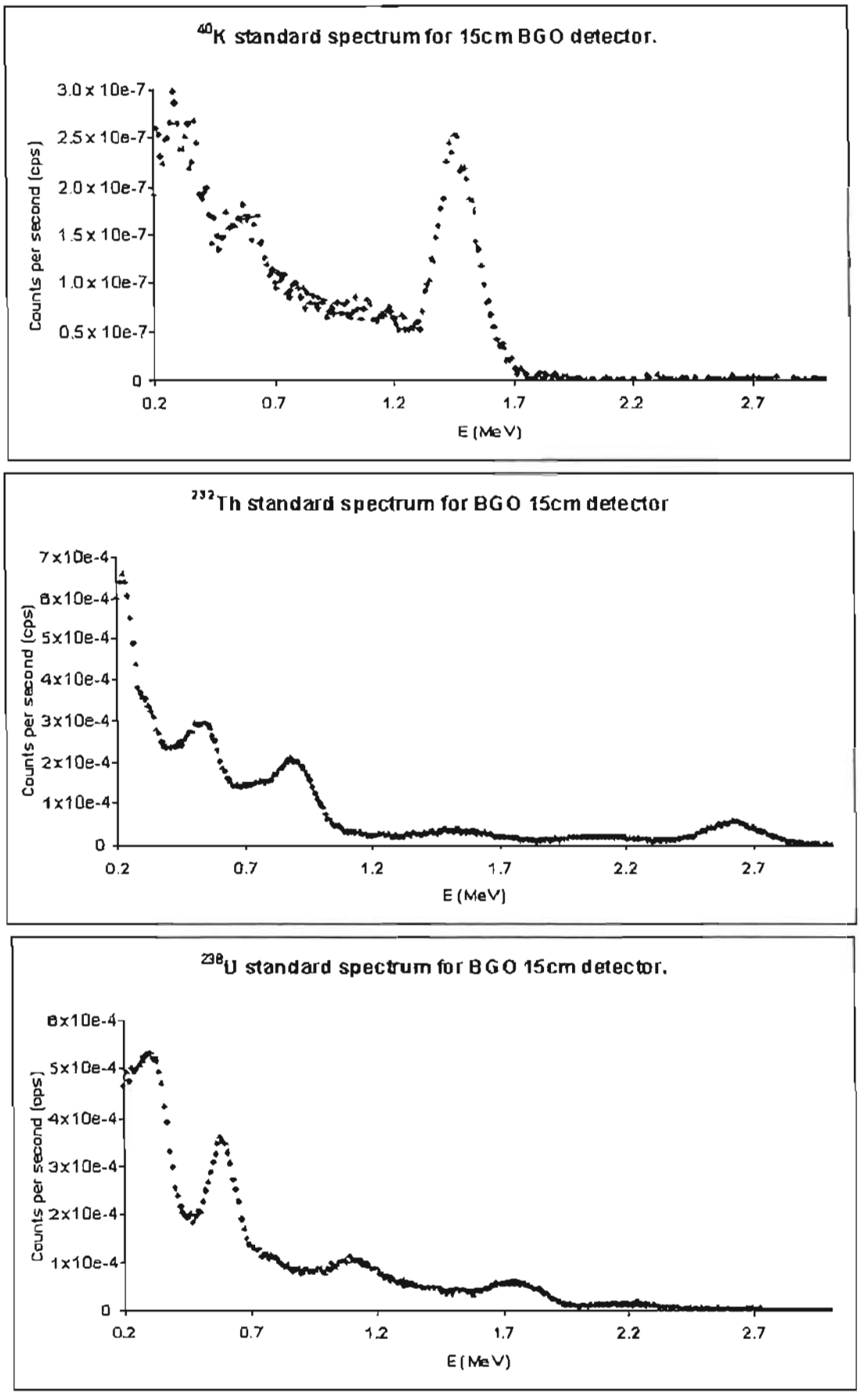

Figure 4-6: ^{40}K, ^{232}Th and ^{238}U standard spectra for the BGO 15cm detector.

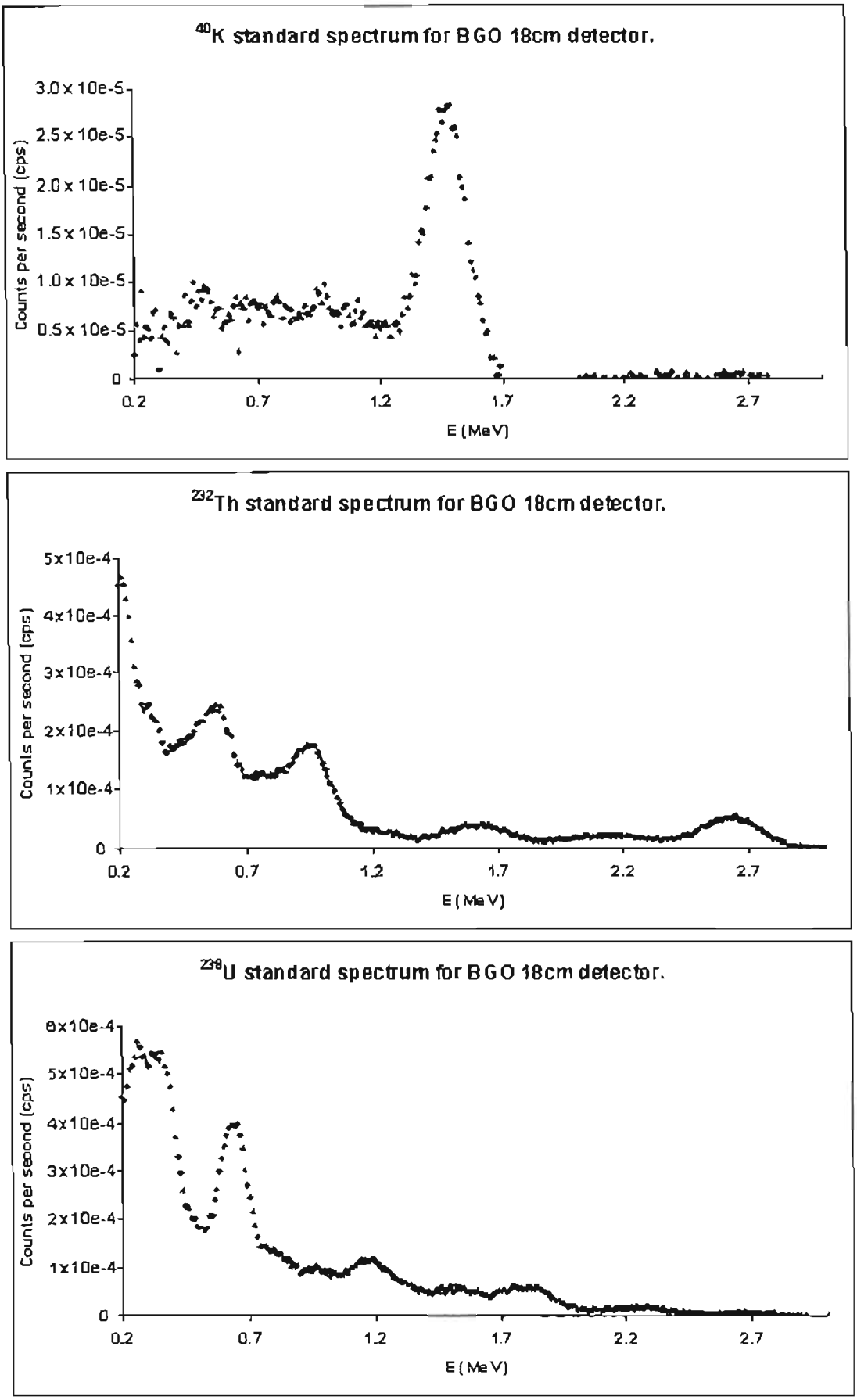

Figure 4-7: ^{40}K, ^{232}Th and ^{238}U standard spectra for the BGO 18cm detector.

The spectra in Figure 4-6 and Figure 4-7 show the calculated standard spectra for both the BGO 18cm detector and 15cm detector. The first set were calculated from spectra that were stabilised using older sets of standard spectra for the respective detectors, taken in a barrel geometry [4]. The resultant standard spectra were then further refined by recalculating new spectra based on the initial spectra, which were then produced in the same final geometry as the required spectra.

Once the standard spectra had been determined FSA data analysis became possible. Spectra were acquired in half-hour batches, and then stabilised and summed before analysis. Analysis involved the determination of the total concentration matrix A shown in equation (4.11) above where the calibration spectra CS were replaced by the measured spectra. A was solved implicitly rather than explicitly, as the parameter C in equation (4.7) with the fitting process outlined in §4.4.2.

4.4.5 Core measurements and profiles

The standard spectra produced were tested first on their own calibration cores, and then on a clay soil-sample taken from the soil near the KVI. This means the standard spectra were calculated, and then used to analyse the spectra measured from the standard cores. This was used as a test of the standard spectra to check the internal consistency and to determine the accuracy of the calculated activity concentrations. The first comparison of the data did not produce good results as can be seen from Table 4-6. Comparing the data for the cores, most specifically for the pure ankersmit-sand core, for most of the nucludes the HPGe detector values obtained are not comparable to those measured with the BGO detectors. This is attributed to the fact that the system is very sensitive to fluctuations in the background contribution (due to changes in cosmic background radiation and radon content of the air). This sensitivity is a consequence of a low activity measurement with a small volume of material resulting in a signal which is predominantly a result of background contribution.

Table 4-6: Activity concentration comparison between BGO 15cm, BGO 18cm and HPGe detectors using initial standard spectra used.

			K ± ΔK	Th ± ΔTh	U ± ΔU
Ankersmit sand + KCl	BGO	(18cm)	1310 ± 13	13.8 ± 1.6	2.8 ± 1.2
	BGO	(15cm)	1240 ± 20	4.9 ± 1.8	1.0 ± 1.2
	HPGe		1310 ± 7	2.90 ± 0.10	3.04 ± 0.08
Ankersmit sand + monazite	BGO	(18cm)	150 ± 15	506 ± 8	103 ± 2
	BGO	(15cm)	130 ± 40	503 ± 3	95 ± 3
	HPGe		105 ± 10	501 ± 7	84.0 ± 1.0
Ankersmit sand + zircon	BGO	(18cm)	20 ± 17	102.0 ± 2.0	360 ± 3
	BGO	(15cm)	170 ± 40	107 ± 2	389 ± 3.03
	HPGe		89 ± 6	103.4 ± 1.6	377 ± 3
Clay core	BGO	(18cm)	402 ± 10	22.4 ± 1.1	2.03 ± 1.61
	BGO	(15cm)	403 ± 20	20.8 ± 1.1	27.2 ± 1.53
	HPGe		440 ± 30	23.0 ± 0.4	15.91 ± 0.19
Ankersmit sand	BGO	(18cm)	180 ± 12	9.8 ± 1.2	6.5 ± 1.6
	BGO	(15cm)	140 ± 20	6.2 ± 1.2	12.4 ± 1.7
	HPGe		104 ± 6	2.90 ± 0.08	3.42 ± 0.06

To address this problem, it may be necessary to look more closely into the effect on the measured background due to the addition of a material with a density greater than air. The first background measurements were made by removing the core and letting the detectors measure without material present. The addition of a material with a density greater than that of air, increases the background not only due to its own radioactive content, but also because of scattering of ambient radiation. This effect was tested by mounting an empty PVC tube (with the same dimensions as a typical core) and filling it with water. Background was then measured again and compared with that of an air filled tube. This comparison showed a definite increase in the background count rate of about 30%. In normal applications this may not pose a significant problem, but in this case the core logger is so sensitive to the background contribution that great care needed to be taken to reduce this component.

Using a water-filled core as the background, the standard spectra were then re-calculated, this time allowing the intensity of the background contribution to be a free parameter (instead of setting it to unity in the matrix). The concentrations of the

nuclides in the background were calculated by fitting the spectrum with the previously calculated standard spectra. Creating a new set of spectra in this manner allowed a new analysis of the data, and produced a better set of results, shown in Table 4-7 below. Note that some effort is being made to better determine the effect of the background on the final results, and this may lead to further refined density adjustments based on the density of the currently measured core. While it is possible to make some allowance for the background, it is impossible to predetermine exactly what the magnitude of its effect will be. This will vary based on core density, and on the current level of ambient background radiation. Also the core may absorb radiation that was previously "detected", and (by scattering) cause radiation that was previously "undetected" to be measured.

Table 4-7: Activity concentrations determined from standard spectra for both BGO detectors. Analysis of standard cores and clay core compared with HPGe values.

			K ± ΔK	Th ± ΔTh	U ± ΔU	Cs ± ΔCs
Ankersmit sand + KCl	BGO	(18cm)	1365 ± 17	7 ± 1.0	6 ± 2	< 0.8
	BGO	(15cm)	1321 ± 15	3.5 ± 1.4	4 ± 3	3.7 ± 1.6
	HPGe		1310 ± 7	2.9 ± 0.10	3.04 ± 0.08	< 1.5
Ankersmit sand + monazite	BGO	(18cm)	110 ± 20	500.0 ± 2.0	84 ± 3	1.8 ± 2.0
	BGO	(15cm)	143 ± 17	503 ± 3	86 ± 4	1.7 ± 2.0
	HPGe		105 ± 10	501 ± 7	84 ± 1	< 1.5
Ankersmit sand + zircon	BGO	(18cm)	97 ± 20	103 ± 1.5	373 ± 3	3.0 ± 2.0
	BGO	(15cm)	117 ± 18	106.0 ± 2.0	372 ± 4	0.3 ± 2.0
	HPGe		89 ± 6	103.4 ± 1.6	377 ± 3	< 1.1
Caesium sand	BGO	(18cm)	334 ± 16	14 ± 1.0	16.9 ± 2.0	122.0 ± 1.7
	BGO	(15cm)	383 ± 14	16.6 ± 1.5	20 ± 3	123.0 ± 1.9
	HPGe		329 ± 20	14.0 ± 0.4	18.0 ± 0.3	124.0 ± 1.9
Clay core	BGO	(18cm)	355 ± 20	17.5 ± 2	20 ± 4	2 ± 3
	BGO	(15cm)	400 ± 30	6 ± 5	19 ± 3	4 ± 3
	HPGe		440 ± 30	23.0 ± 0.4	15.91 ± 0.19	3.65 ± 0.12
Ankersmit sand	BGO	(18cm)	130 ± 14	5.1 ± 1.0	3.7 ± 1.8	< 0.4
	BGO	(15cm)	97 ± 13	2.60 ± 1.30	10 ± 3	< 1.0
	HPGe		104 ± 6	2.90 ± 0.08	3.42 ± 0.06	< 0.11

Table 4-7 shows that most of the values agree within experimental uncertainty. For example, for the KCl core, the expected concentrations (based on HPGe analysis) of ^{40}K, ^{232}Th and ^{238}U are 1310 ± 7 Bq/kg, 2.9 ± 0.1 Bq/kg and 3.04 ± 0.08 Bq/kg respectively (for the BGO 15cm detector). The results of the standard spectrum analysis give 1321 ± 15 Bq/kg, 3.5 ± 1.4 Bq/kg and 4 ± 3 Bq/kg respectively, which all lie within the experimental uncertainties. The results from the BGO 18cm detector are more discouraging, but do lie close to the values expected (within experimental uncertainty). There are still differences though, and in some cases very large. Consider the concentrations obtained for the clay core sample, where the HPGe measured 23 Bq/kg for the Th content, and the BGO 15cm measured 6 Bq/kg and the BGO 18cm measured 17.5 Bq/kg. Similarly for the caesium sand core, where the HPGe measured 329 Bq/kg of K content and the BGO 15cm and 18cm detectors measured 383 Bq/kg and 334 Bq/kg respectively.

It is believed that these discrepancies are due to the density dependence of the background contribution. To compensate this future measurements will make use of more than one set of standard spectra. These additional sets will then be constructed using varying densities of materials for their background parameters. An additional suggestion would be to implement the proposed density metre on one of the other core-logger frame platforms to measure the density of the material for each section of the core. This would then allow density-dependent analysis. Currently this is not yet possible, and would require, in addition to several background cores of known densities and an implementation of the density metre, a re-engineering of the MPA software so that the analysis could be handled automatically and not require a manual selection of the standard spectra for each section examined.

4.5 Core comparison with "real" data

With the calculation of standard spectra that produce acceptable results (when samples were measured on an HPGe detector), and a mechanical mechanism that allows cores to be mounted and measured stepwise, it was possible to begin using the system to measure sample cores.

For this process, two cores were obtained by RIZA for measurement. The cores were taken from adjacent locations and for the purposes of this comparison can be considered to be almost identical. One core was sliced into segments and analysed on an HPGe detector, and the other was analysed using PHAROS.

Core profiles are shown for ^{137}Cs (Figure 4-8), ^{232}Th (Figure 4-9) and ^{238}U (Figure 4-10). The results of these measurements show acceptable agreement between the values measured with the 15cm BGO detector and the HPGe-LOAX detector, for example the Cs profiles, but there is a considerable systematic discrepancy in the Th profile.

With the PHAROS BGO spectra were acquired in 2 hours per core step, in contrast to the 6 – 12 hour measuring times on the HPGe detector. Despite having a more favourable geometry and improved measuring times, the HPGe is less sensitive than the BGO so these discrepancies aren't attributed to the difference in measuring times. Uncertainties in the BGO results are influenced by background and the fact that the standard spectra used in the analysis are not completely orthogonal.

Further, it must be remembered that the measurements with the BGO were done with the core still intact, which means that there will be some overlap for each core-step from the regions above and below the selected 2cm slice. The HPGe measurements were performed with the core dissected into the separate pieces and each piece measured individually. This overlap will also affect the calculated concentrations, which can be seen in the almost continuous curve depicted by the BGO detector, and the large changes from step to step in the HPGe measurements.

All three comparisons seem to have reasonable correlation in terms of the shape of the plots. The ^{232}Th shows a distinct systematic offset though, which is not evident in the ^{137}Cs and ^{238}U plots. This offset could be a result of the HPGe-LOAX detector being systematically offset. Similarly it may also be due to the test core having a different density to the calibration cores, and hence the standard spectra are not strictly valid.

The ^{238}U profile (Figure 4-10) shows the strongest correlation between the two data sets. Again, while not all points overlap there is a correlation between overall shapes

of the profiles as a whole. Note that the sudden steps in activity for the BGO measurements from 26cm to 28cm, and from 66cm to 68cm show when the core section was exchanged for the next one. This is because the NITG core measured was not a single 1m long core, but was divided into 3 section (each roughly 30cm long).

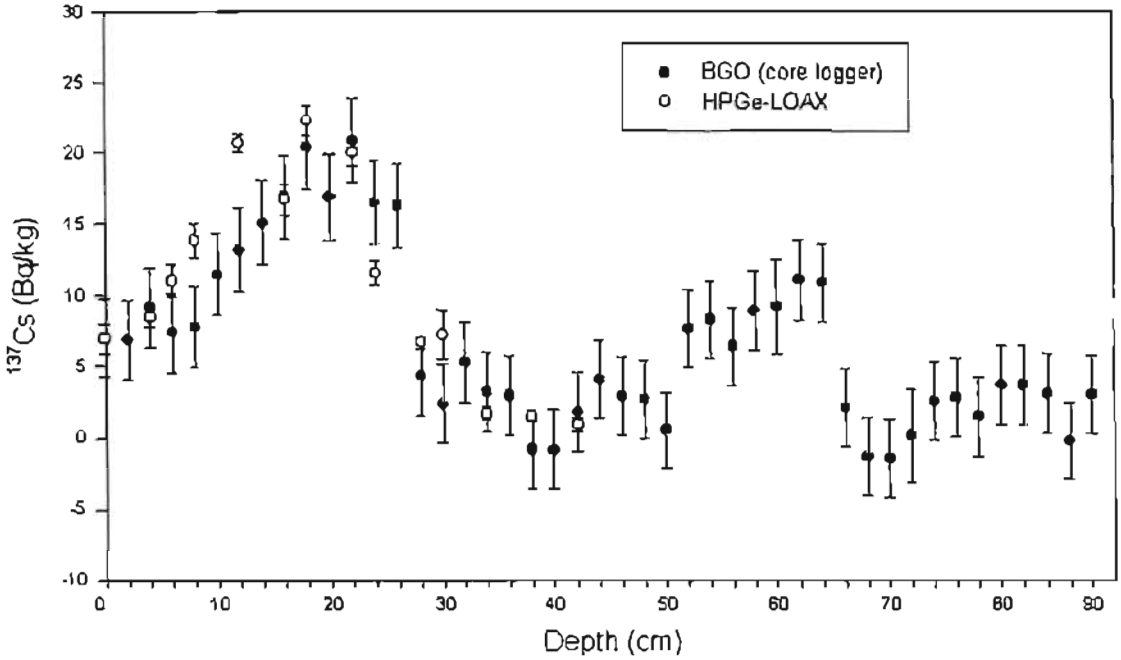

Figure 4-8: ^{137}Cs profile obtained with BGO 15cm detector compared with data from an HPGe-LOAX detector.

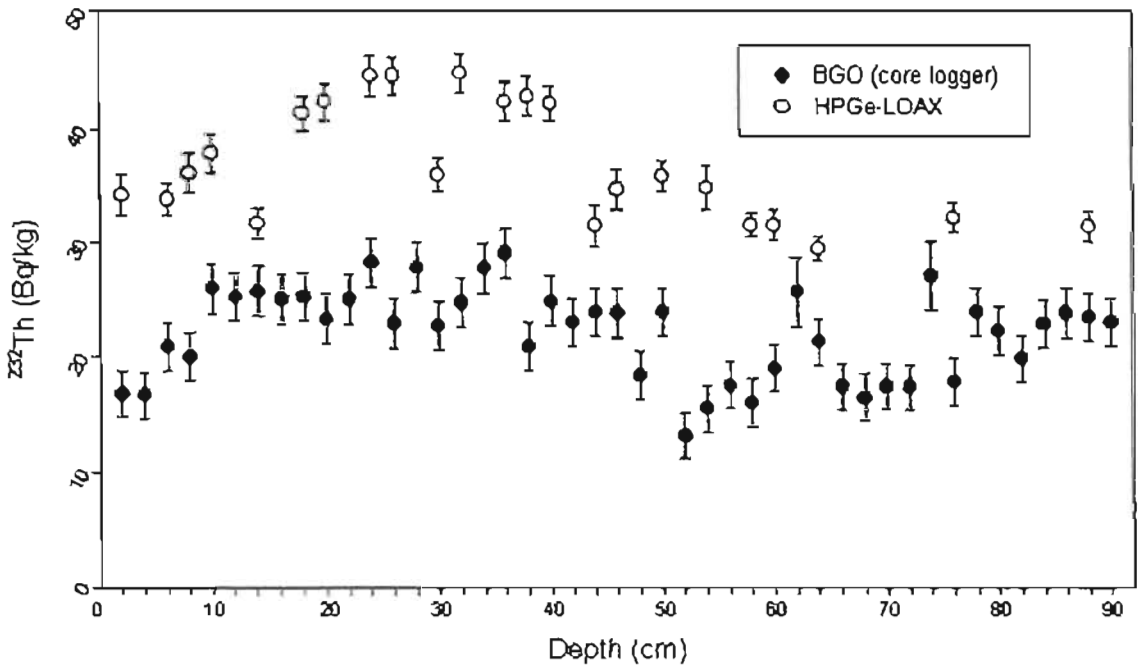

Figure 4-9: ^{232}Th profile obtained with BGO 15cm compared with data from an HPGe-LOAX detector.

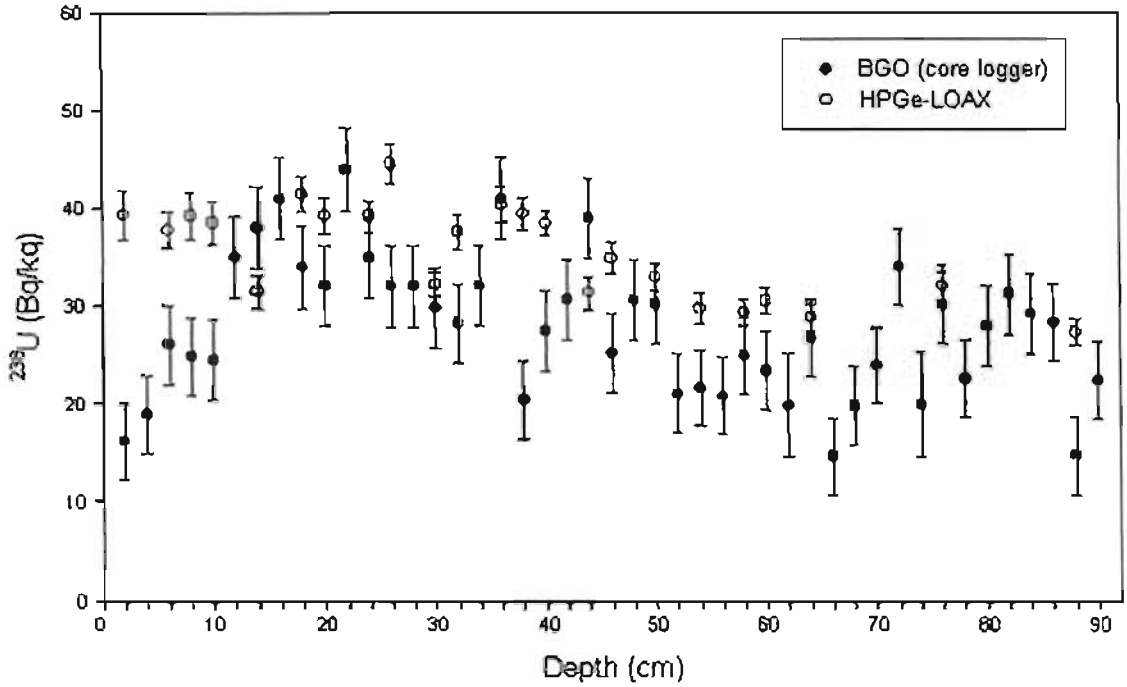

Figure 4-10: ^{238}U profile obtained with BGO 15cm and compared with data from an HPGe-LOAX detector.

4.6 Conclusion

For this phase of the project, the system has expanded from a single to a multi-detector configuration. Part of this process involved examining the properties and operation of the newly installed BGO detectors as had been previously done with the CsI detector. This examination allows a comparison and highlights the advantages and disadvantages of each detector type.

Looking at the overall background signals of the detectors, the CsI has a lower measured total count than the BGO, whose background is primarily self generated. This implies that use of the BGO required a wider slit and hence degradation of the spatial resolution. In defence of the BGO, it must be similarly noted that it also has a higher background because of its greater efficiency – i.e. the CsI has a lower sensitivity and hence will require a longer measuring time to get the same statistics. The CsI was tested primarily under ideal conditions, with an active, point-like source. The use of a 6mm slit with low activity sources, typically producing count

rates only marginally higher than the recorded background, implies however that the slit would need to be widened for the CsI as well as the BGO.

One aspect that was briefly considered for the CsI and not the BGO detector was energy resolution. The CsI does have a better energy resolution than that of the BGO, but this is not really an advantage when considering the analysis technique (FSA). If the spectra were being analysed using the windows method (where the steepness of the peak is a factor) then this might have played a role. Instead, it is not an essential consideration when comparing the two detector types.

Overall, as a stand-alone detector for the core logger application, the BGO represents a better selection. The desired result would be a combination of the advantages of each, through the use of both types of detectors in the core logger, but this would require a way of combining the spectra obtained from each detector, which currently is infeasible.

This section has also described the calculation of the standard spectra as well as some of the theory behind the FSA method. These standard spectra are used with MPA to analyse the BGO spectra measured of a sample RIZA NITG core. The results from this analysis can be compared with the results obtained by measuring the same core (by parts) in an HPGe detector, and are presented in §4.5. While there is some correlation between the measured results, there are still many areas where the two methods did not agree. In particular for the ^{232}Th (Figure 4-9) profile there is a distinct difference between the measured results. However, it must be noted that these differences do appear to be systematic in nature. While the points do not overlap, both profiles have the same general shape. This implies that there may be a systematic offset introduced by the HPGe-LOAX detector (for example) and at any rate suggests that accurate results (meaning the correct concentrations of the measured nuclide are obtained) are possible if this offset can be calibrated into the system. At the same time, it can be seen that this apparent systematic offset does not appear with the ^{137}Cs profile (Figure 4-8) or the ^{238}U (Figure 4-10) profile. These two plots do show a better correlation between the HPGe-LOAX values and the core-logger values. Improvement in these results could be made through a more advanced and detailed analysis of the effect of the background on the overall spectrum analysis. It

was earlier noted that the system seemed to be very sensitive to fluctuations in the measured background, which seems to be dependent on (amongst other factors) the density of the measured core.

Also, as mentioned in §5, there is some interference in the measured spectra between a chosen core slice and its adjacent slices. This is a problem that was briefly considered in [1]. To be able to unfold these spectra, it will be necessary to perform a deconvolution based on the position of the core and the slit width. This signal deconvolution will be looked at Chapter 5.

Chapter 5 :
Profile deconvolution

5.1 Introduction

The development of the PHAROS core-logging system has undergone several stages. In Chapter 2 [1], preliminary investigations were undertaken using a Caesium Iodide detector (CsI) and a point like ^{137}Cs source. An initial hardware setup was used to determine optimal shielding coefficients. The effects of lead shielding thickness were investigated, with comparisons between 5cm, 10cm and 15cm leading to the decision to use a thickness of 10cm. A 10mm slit was then built into one of the side walls of the castle to collimate the soil-core radiation. The spatial resolution of this slit was measured by moving the point-like ^{137}Cs up and down in front of the opening. This gave a FWHM (Full Width Half Maximum) value of roughly 20mm. Since this value was outside the initial system requirement of 10mm the slit was then narrowed to 6cm which yielded an average FWHM of approximately 13mm.

Current core measurements were taken with 1m long soil-cores (divided into 3 segments ~30cm each) moving through the centre of the core-logger frame and measured in 2cm steps over periods of 1-2 hours. Chapter 2, §2.6 examines the slit configuration in great detail. One of the results from this chapter shows that the spatial resolution of the slit varies with the distance between the source and the slit. A slit size of 2cm is expected to have an average resolution of ~3cm. This then implies that there will be an overlap in measured core spectra for core slices of 2cm. It is therefore instructive to investigate this overlap effect in an attempt to determine the minimum possible spatial resolution of the system. Ideally the system should be able to deconvolve the overlapped signals in order to determine a more accurate profile of the core. This chapter looks at a method of deconvolution of the measured signals.

5.2 Theoretical background

There are some mathematical (and physical) concepts that help in understanding the response of a system to an input signal, or in the core-logger case the spatial distribution of a non-homogenous radioactive sample when viewed through a finite aperture.

5.2.1 The convolution of a signal

We first consider the relationship between a time series input signal $f(t)$ and the output $g(t)$ of a system that has an impulse response function $h(t)$. The input signal is modified by the response of the system and the output is given by the convolution formula:

$$g(t) = \int_{-\infty}^{\infty} f(t')h(t-t')dt' \qquad (5.1)$$

If the input function $f(t)$ is equal to the delta function $\delta(t)$ then

$$g(t) = \int \delta(t')h(t-t')dt = h(t)\,. \qquad (5.2)$$

which is the response of the system. Thus the response of an unknown system can be determined by injecting an impulse function and measuring the output.

In practice, the input function is sampled at discrete intervals to give the input series $f_n = f(n\Delta t)$ where n = 0, 1, 2, ... and Δt is the time between samples. The discrete form of Eqn 5.1 (for N samples) is then

$$g_i = \sum_{j=-N/2+1}^{N/2} f_j h_{i-j}\,. \qquad (5.3)$$

The convolution operation is usually denoted by the symbol $\otimes$, and is mathematically commutative, i.e. $f \otimes g \equiv g \otimes f$. The process can be thought of as shifting and multiplying the signals at all common points, and the effect of convolution is to smear the signal $f(t)$ in time according to the recipe provided by the response function $h(t)$ [14].

5.2.2 Deconvolution

Deconvolution can be defined as the process of finding the most likely input to a system, given the known properties and measured outputs of the system, or in other words the process of undoing the smearing in a data set which has occurred under the influence of a known response function [14]. This is defined similarly to equation (5.3), except now g_i is known and $\sum_{j=-N/2+1}^{N/2} f_j h_{i-j}$ is considered to be a set of N linear equations for the unknown quantities f_i.

This is most directly applicable to the case of measured spectra where the output is the convolution of the input signal (i.e. the *actual* spectrum) and the response function of the detector. Therefore for a detector with a well-defined response function it is possible to determine the actual spectrum of an unknown source by deconvolving the output function with the response function. This can be accomplished by doing a calculation in Fourier space and using the convolution theorem (given in Appendix V), which states that $\Im\{f(x) \otimes h(x)\} = F(s) \cdot H(s) = G(s)$. For the purpose of this investigation, we take the symbol $\Im$ to denote the FFT (fast Fourier transform) of the function. Given output function g and response function h, let their FFTs be $\Im(g) = G$ and $\Im(h) = H$ respectively. Then the FFT of the input function is given by F and determined by $F = G / H$. Hence the input function f can be determined by taking the inverse FFT of F.

Thus, given g and h, $G = \Im(g)$ and $H = \Im(h)$ can be calculated. From this $F = G / H$ and taking the inverse FFT, the function f can be calculated as $f = \Im^{-1}(F)$.

In practice, the deconvolution calculation is carried out by taking the FFT of the functions g, h. These should both be functions of equal length n (which is a power of 2). If this is not the case then either one or both functions should be padded with zeros. This yields functions G and H of same length m which makes the element-by-element division G / H valid. Note also that the array H needs to be scanned for

elements with zero values as these would result in a divide by zero error. In practice these values are replaced by a small positive value ≈ 0.

5.3 Application of deconvolution to the core-logger

We will now apply the above treatment to the core logger, when its radioactive profile is sampled through a finite aperture (slit).

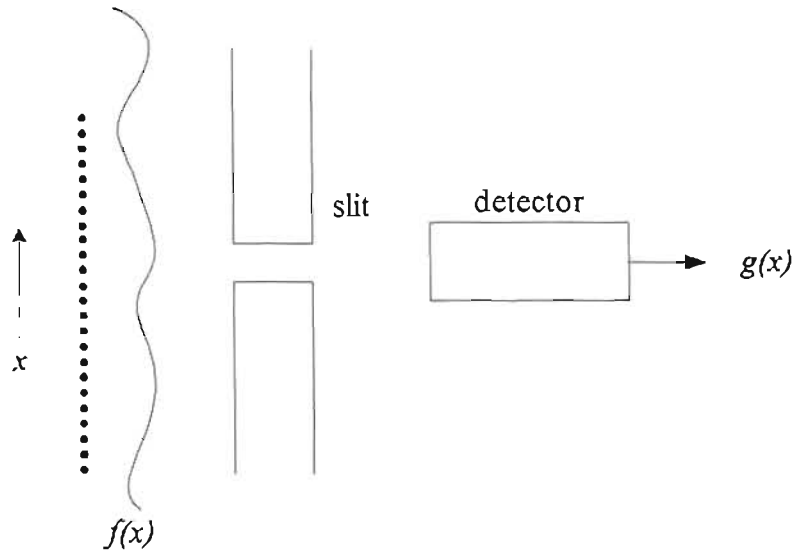

Figure 5-1: This shows the experimental arrangement used to measure a core profile. The core is shown as a distributed line source.

For simplicity, we make a few idealisations to the experimental arrangement shown in Figure 5-1. Firstly we assume the core can be approximated by a one dimensional line of radioactive point sources whose activity varies as $f(x)$, where x is the position along this line. The slit and detector are then placed in front of this line source. We assume that the aperture/detector combination was then moved vertically (in practice it was actually the core that moved) and the output function $g(x)$ is measured for every x position of the slit/detector. For each measurement, the detector will receive radiation from the source at x and the range of sources centred around x. The resolution of the aperture depends on its impulse response function, and will determine the range of contributing sources.

The deconvolution problem can now be re-stated. Given the detector output $g(x)$ and the impulse response $h(x)$ of the slit aperture, can we determine the actual distribution of the sources, i.e. $f(x)$?

The impulse function of the slit has already been measured in Chapter 2 by finding the profile of a point source (the impulse $\delta(x)$) while it was moved vertically past the slit. The core profile $f(x)$ can then be determined from

$$f(x) = \Im^{-1}(G / H). \qquad (5.4)$$

There are two implicit assumptions made in the above treatment:

(1) The impulse function was determined using a ^{137}Cs source, so strictly the deconvolution only holds if the core contains an array of ^{137}Cs sources. Ideally, a different response function needs to be measured for each possible source contained in the core.

(2) The source is not 1-dimensional and has structure in both directions perpendicular to the x-axis shown in Figure 5-1. It has been shown that the slit resolution will vary significantly over a distance of one core diameter from the slit, whereas the response chosen is valid only for a distance of 7.5cm from the slit.

Ideally the effects of both (1) and (2) should be taken into account when performing the deconvolution. In practice, this should only make the detail of the deconvolution process more complex, while the principle will remain the same.

5.4 Experimental investigation

The deconvolution calculation was first checked using artificial data. An input function $f(x)$ and slit function $h(x)$are shown in Figure 5-2.

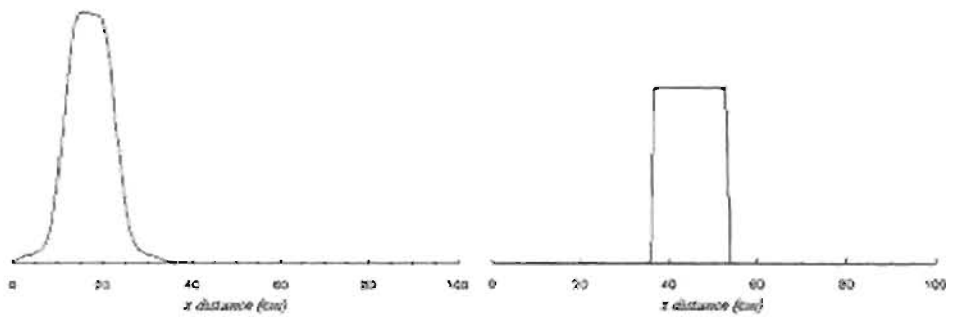

Figure 5-2: This shows the artificial response function f (on the left) and the artificial input function h on the right.

An artificially large width of 20cm has been chosen for the slit to accentuate the smoothing process. The convolution of these functions is shown below in Figure 5-3.

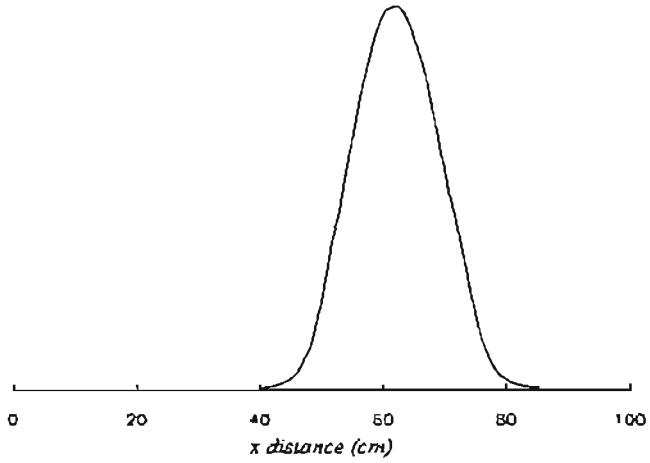

Figure 5-3: The output function *g* resulting from the convolution of *h* and *f* shown in Figure 5-2.

We now have $g(x)$ and $h(x)$ so we can determine $f'(x)$, the estimate of the actual profile $f(x)$, using Eqn 5.4.

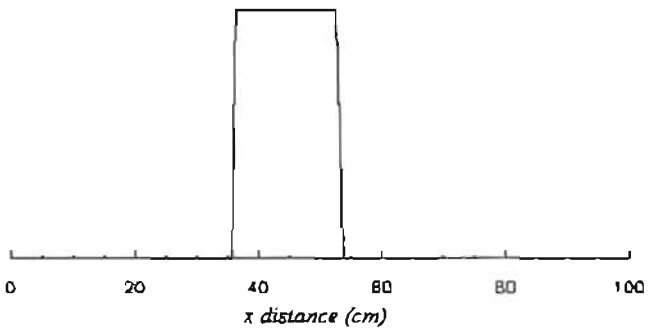

Figure 5-4: The deconvolved input function *f'*, which has the same shape as original input function *f*.

From Figure 5-4 above the deconvolved output function is clearly the same as the input function shown in Figure 5-2, demonstrating the validity of the deconvolution calculation. Now we use the ideal core logger response function given in Figure 5-5 and the ^{232}Th profile shown in Figure 5-6 for the functions $h(x)$ and $f(x)$ respectively.

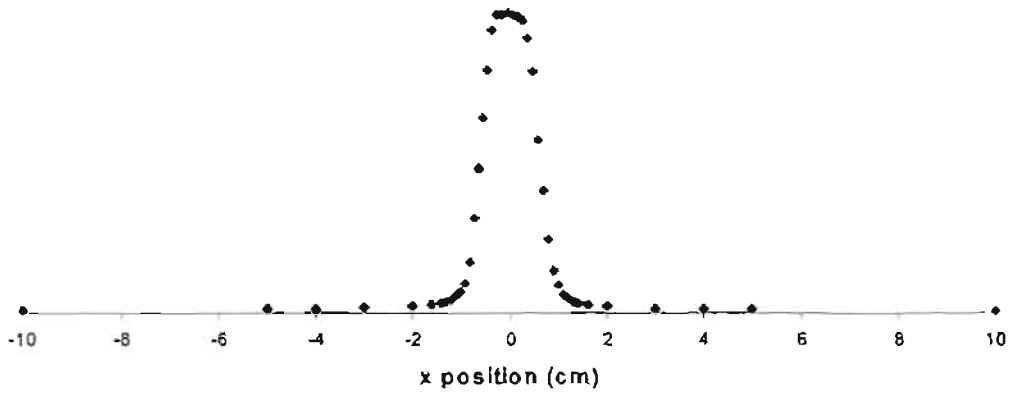

Figure 5-5: Response function *h(x)* obtained using a Cs source for a 6mm slit.

Figure 5-5 shows the response obtained with a ^{137}Cs source at a distance of 7.5cm from the slit. Figure 5-6 shows a measured core profile for ^{232}Th, which will be used as the input function *f*. Strictly, this function should be treated as the output *g* since it is the measured response of the core logger. However, it is used here simply as a more complex test function in the investigation of the deconvolution process.

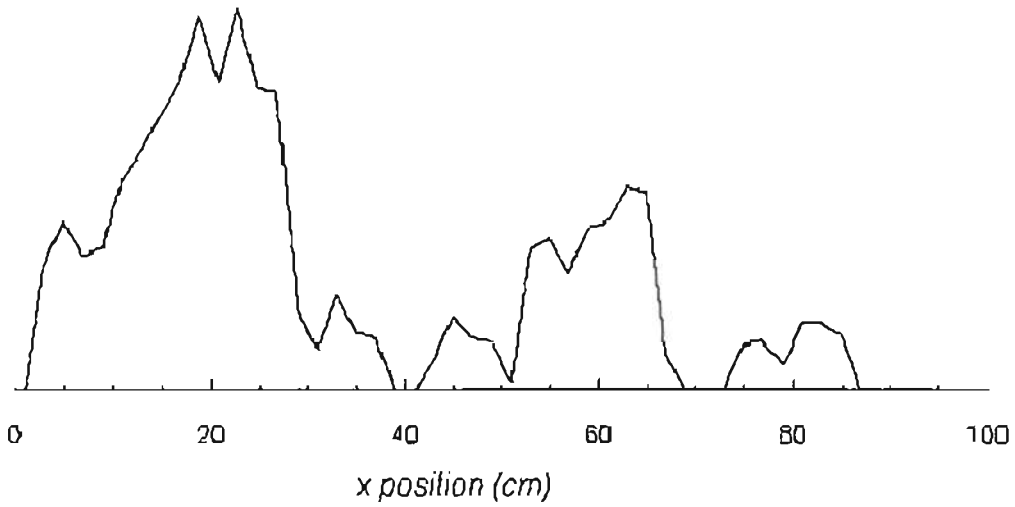

Figure 5-6: The ^{232}Th profile measured with the core logger system, to be used as the input function *f*.

We follow the same process outlined above, first convolving, then deconvolving the functions and comparing the original *f(x)* with the deconvolved *f'(x)*. The convolution is shown in Figure 5-7, and the deconvolved output in Figure 5-8.

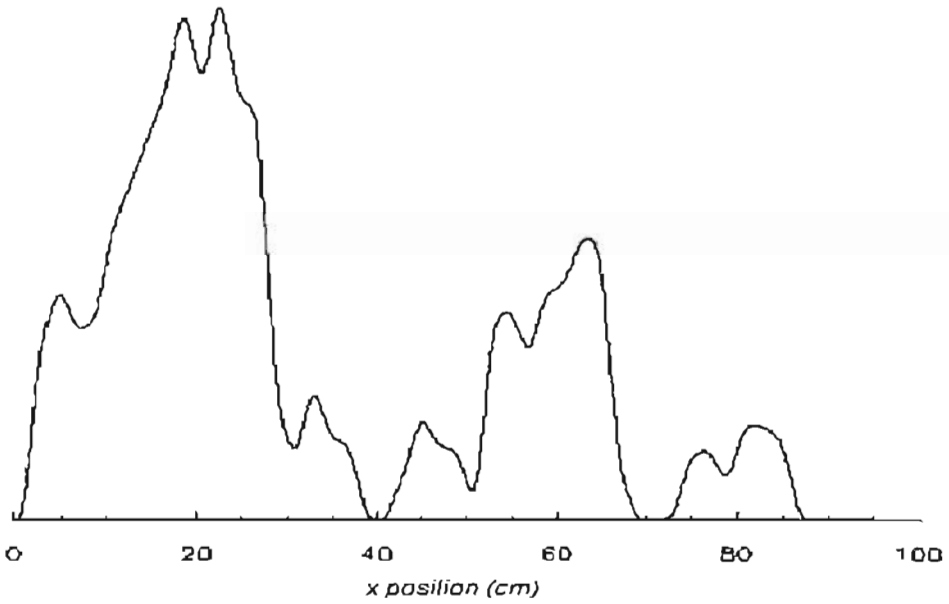

Figure 5-7: The output function *g* for the convolution of functions *h* (Figure 5-5) and *f* (Figure 5-6).

Noticeably, comparing Figure 5-7 to Figure 5-6. it can be immediately seen that some 'smearing' of the signal has occurred. In comparison to the *f* function, the response *h* in Figure 5-5 is comparable to a δ function, hence the similarity between the output and input functions.

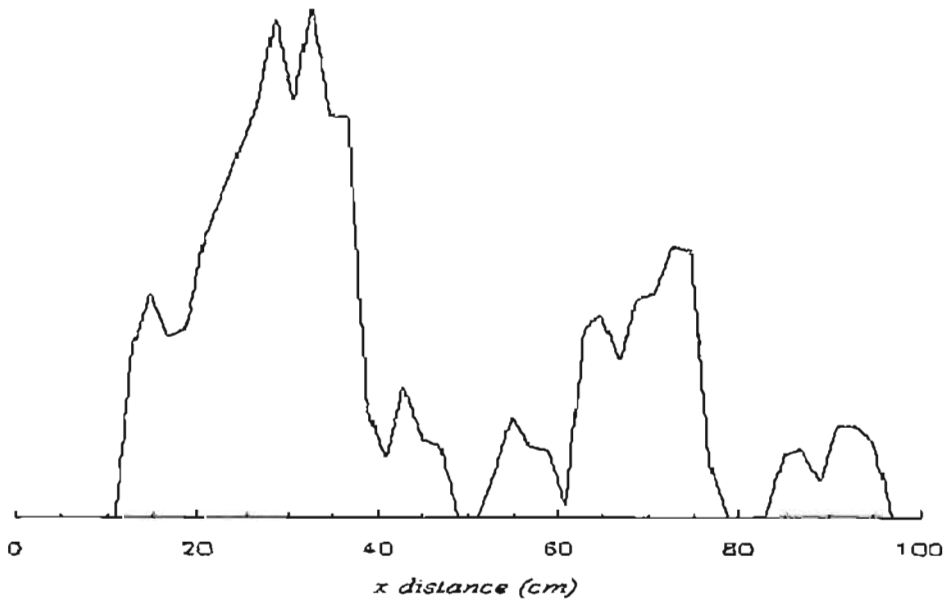

Figure 5-8: The resultant function *f'* of the deconvolution of the output function *g* (Figure 5-7) and the response function *h* (Figure 5-5).

Qualitatively, *f'* shown in Figure 5-8 looks the same as the original *f* shown in Figure 5-6, which indicates that the method of deconvolution was well-behaved.

It should be noted here that the response function obtained using the caesium source is specific to that particular energy spectrum. Ideally, a separate response function should be obtained for each energy source present in the input. For the purpose of this investigation we shall assume that the Cs response function is applicable to all energies, and specifically the ^{232}Th profile that was used here.

The deconvolution should be performed with Figure 5-6 as the output function g and not the input function h, since it is the profile obtained from a core measurement. Unfortunately there is nothing to compare this result to, with no prior knowledge of the actual Th distribution of the measured core. Therefore no comment could be made about the accuracy of the process. Ideally, this could be tested by measuring the profile of a Th sample core having a known distribution, and spatial features that had a size that was less than 1.3cm, i.e. the resolution of the 6mm slit.

5.5 Conclusion

The convolution theorem (Appendix V) gives a method for deconvolving two functions which involves the use of Fast Fourier transforms. An analysis of this deconvolution has resulted in a process that in principle could be used to unfold the core profiles recorded by the core logger. The principle of the process was demonstrated using artificial data and then some idealised core logger sample data. In both cases the deconvolution performed satisfactorily.

It is important to note that this is a brief treatment of the analysis that makes several assumptions:

(1) the core is idealised as a one dimensional line of point sources at a distance of 7.5cm from the slit;
(2) we have assumed the response function obtained using a ^{137}Cs source is applicable to the ^{232}Th energy ranges;
(3) we have ignored the dependence of the slit resolution on the distance of the source from the slit.

Given the limiting nature of these assumptions, it must be asserted that the treatment outlined in this chapter is by no means complete. It will serve to act as a guide in

developing a more detailed convolution which can then be extended to a more real data set.

Chapter 6 :
Conclusion

Each chapter has covered a specific stage of development of a system for the automatic, high-resolution radiometric analysis of soil core samples. As such, each chapter deals with its own specific goals and whether they were met or not. The primary goals of the project include: the automation of the whole soil-core measurement process, from data logging to analysis to reporting; a resolution of 1cm; and a turnaround measurement time in the region of 24 hours.

Presently the core logger has an average resolution of approximately 3cm. This is an unavoidable consequence of the generally low activity of samples measured (10 – 50 Bq/kg). Initial tests with a point-like ^{137}Cs source and the CsI detector indicated that a 1cm resolution was possible using a 0.6cm slit in the lead wall. However, this configuration when used with a more typical low-activity source required longer measuring times to compensate for the poor statistics. The widening of the slit resulted in the detectors seeing more of the source material which helped to reduce this measuring time. It would seem that the slit width can be seen as a trade-off of resolution versus acceptable measuring time. Both the resolution and measuring time requirements can only be met on the extreme ends of this trade-off. It is therefore necessary to compromise on both requirements and find an acceptable concession for both.

The measuring time for a single core is presently estimated as 36 – 50 hours, as opposed to the desired 24 hours. Data was captured using 3 independent detectors. This configuration gives no advantage over a system with only one detector, since the results from each detector are considered separately. The possibility of somehow combining (or summing) the measured spectra from each detector to improve the measuring time is under investigation. In the interim it must be remembered that the system still represents an improvement over the original manual methods employed.

There are several aspects of the automation configuration that are incomplete. At this stage it can be said that PHAROS is capable of scanning a core and logging data with no user intervention. However, analysis is still manual, and the movement of the core is susceptible to inaccuracies introduced by the stepper-motor.

In addition to the work on the mechanical design, investigation of the analysis of the captured data was also undertaken. Calibration cores were constructed for the core-logger geometry. The measurements of these cores were then used to calculate the standard spectra (one for each of the radionuclides of interest) for the system. These spectra represent the response per unit of time of a detector for a particular radionuclide and are used to calculate the activity concentrations. The standard spectra are multiplied and summed to produce a calculated spectrum that is then fitted to the measured spectrum. If an acceptable fit is obtained then the radionuclide concentrations can be taken from the calculated spectrum. In principle it was found that this process works well for PHAROS. Comparisons with known core samples showed good agreement, with some systematic offset present. This offset may be introduced by the HPGe detector used to measure the known sample, and generally the comparison plots all showed the same shape. It was also noted that the system is increasingly showing its sensitivity to the influence of the background signal. Results seem to be influenced by the density of the measured core and it may be necessary to construct different sets of standard spectra for varying density standard cores.

Unfolding of the measured signal can in principle be done using the methods outlined in Chapter 5. This is especially necessary because of the overlap in measured signal which arises because the core is no longer dissected. Traditionally this is not an issue because the core is sliced with each part measured separately. Keeping the core intact means that each measured spectrum will contain interference from the core slices neighbouring the current region. For a higher accuracy it therefore becomes essential to deconvolve these overlapping signals, the process for which is demonstrated successfully.

Future work

At the time of the author's departure development was still in progress. MEDUSA software needs to be re-written to include multiple detectors, and the stepper-motor replaced with an alternative mechanical arrangement such as an absolute position encoder, a counter balanced pulley or an hydraulic lift system. Once a logging and analysis mechanism is in place that can combine the data captured on each detector it may be possible to both reduce measurement time and improve resolution.

Acknowledgements

The author would like to express his gratitude to all the members of the Nuclear Geophysics Group at the Kernfysisch Versneller Instituut for their continual guidance and substantial input to the overall development of the core-logger system.

In particular the author would like to express gratitude to the following individuals: to Dr J Limburg for his help in designing the mechanical aspects of PHAROS and for his guidance in all the initial phases; to Dr RJ de Meijer for his continued input regarding the theoretical aspect of the project, for valuable input regarding the finalised form of this document, for continual textual and factual amendments and corrections; to Dr C Rigollet for her contributions to the textual works and her supervision concerning the standard spectra and measurement of the initial test cores.

The author would also like to thank all the people at the KVI who not only contributed in some way to this work but also helped to make the experience a pleasant and memorable one.

Finally the author would like to express his gratitude to Prof. Mike Alport of the Applied Physics Group, School of Pure and Applied Physics, University of Natal (Durban) for his guidance in the final stages of this document.

References

[1] R Pitout, et al (February 2000), *"PHAROS Part I – Initial measurements and calibration of a CsI detector"*, KVI Internal report Z-101.

[2] R Pitout et al (January 2001), *"PHAROS Part II – Mechanical set up: system design and software"*, KVI internal report Z-110.

[3] R Pitout, C Rigollet (February 2001), *"PHAROS Part III – Multiple detectors - BGO & CsI"*, Nuclear Geophysics Division (NGD), Kernfysisch Versneller Instituut (KVI), KVI Internal Report Z-111.

[4] C Stapel, J Limburg and RJ de Meijer (July 7, 1997), *"Calibration of BGO scintillation detectors in a bore-hole geometry"*, Nuclear Geophysics Division (NGD), Kernfysisch Versneller Instituut (KVI), KVI Internal Report Z-62.

[5] PHGM Hendriks, J Limburg, LB Venema and RJ de Meijer (august 1999), *"Full spectrum analysis of natural gamma-ray spectra"*, Nuclear Geophysics Division (NGD), Kernfysisch Versneller Instituut (KVI).

[6] C Rigollet, *"PHAROS: Pluri-detector, High-resolution Analyzer of Radiometric properties of Soil cores"*, Nuclear Geophysics Division (NGD), Kernfysisch Versneller Instituut (KVI).

[7] Glenn F Knoll (1979), *"Radiation Detection and Measurement"*, John Wiley & Sons.

[8] WR Leo (1987), *"Techniques for Nuclear and Particle Physics Experiments"*, Springer-Verlag, Berlin, Heidelburg.

[9] Scionix (detector manufacturers) website: http://www.scionix.nl.

[10] PW Groen (February 1998), *"Een nieuw, zeer gevoelig detectiesysteem voor de radiometrische dichtheidsmeter van IHC Systems"*, KVI Internal Report.

[11] JH Hubbel and SM Seltzer, Ionizing Radiation Division, Physics Laboratory, National Institute of Standards and Technology, Gaithersburg, MD 20899 http://physics.nist.gov/PhysRefData/XrayMassCoef/.

[12] RJ de Meijer (1998), *"Heavy minerals: from 'Edelstein' to 'Einstein'"*, Journal of Geochemical Exploration 62, pp81-103.

[13] Herbert Taub, Donald Schilling (1986):*"Principles of communication systems"*, McGraw-Hill, International Edition.

[14] William H Press, Brian P Flannery, Saul A Teukolsky, William T Vetterling (November, 1989), *"Numerical recipes in Pascal"*, Cambridge University Press

[15] Emmanuel C. Ifeachor, Barrie W. Jervis, *"Digital Signal Processing – A Practical Approach"*, Addison-Wesley.

[16] R.D. Evans (1955), *"The Atomic Nucleus"*, M^{c}Graw-Hill, New York.

[17] Kenneth S. Krane (1988), *"Introductory Nuclear Physics"*, John Wiley & Sons.

[18] J.C. Davis (1973), *"Statistics and data analysis in Geology"*, Wiley & Sons, New York.

[19] Vladimir Zajíc (1986), *"Instrumental corrections of Peak Areas in Gamma-ray Sum-Peak counting"*, International Journal of Applied Radiation and Isotopes, Vol. 37, No. 12, pp 1225 – 1233.

[20] *"The CRC Handbook of Chemistry and Physics"*, 50th Edition, The Chemical Rubber Company.

[21] K. Debertin & R.G. Helmer (1988), *"Gamma- and X-ray spectrometry with semiconductor detectors"*, North-Holland.

[22] Ortec Application Note AN43 (September 1987), *"Experiments in Nuclear Science"*, http://www.ortec-online.com/application-notes/an34/an34_front.htm.

[23] Ortec GammaVision32 User Manuals

[24] Ortec How-To Guide for GammaVision32 Ver 5.2, http://www.ortec-online.com/application-notes/gv_start.pdf

[25] Richard Lyons (1998), *"Windowing functions improve FFT results, Part I"*, Test & Measurement World, June 1998, pp 37 – 44.

[26] Richard Lyons (1998), *"Windowing functions improve FFT results, Part II"*, Test & Measurement World, September 1998, pp 53 – 60.

Appendices

Appendix I Spectra used for energy calibration of CsI detector.

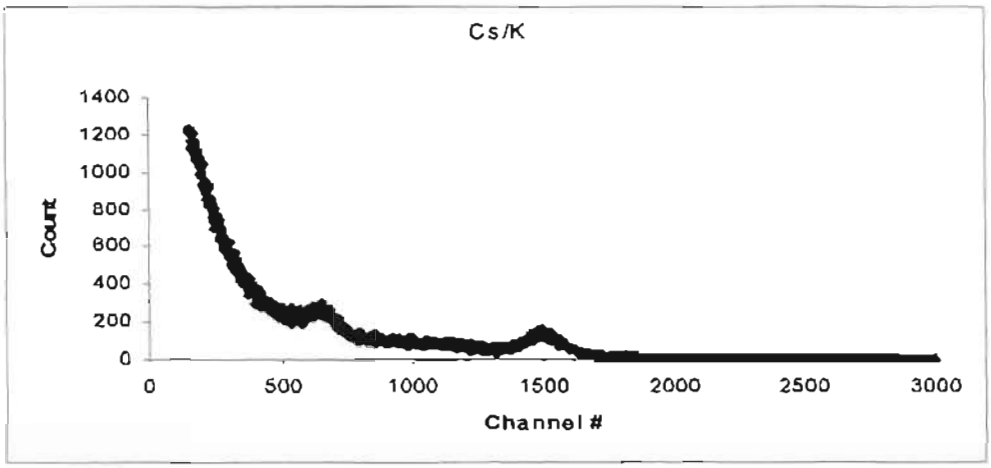

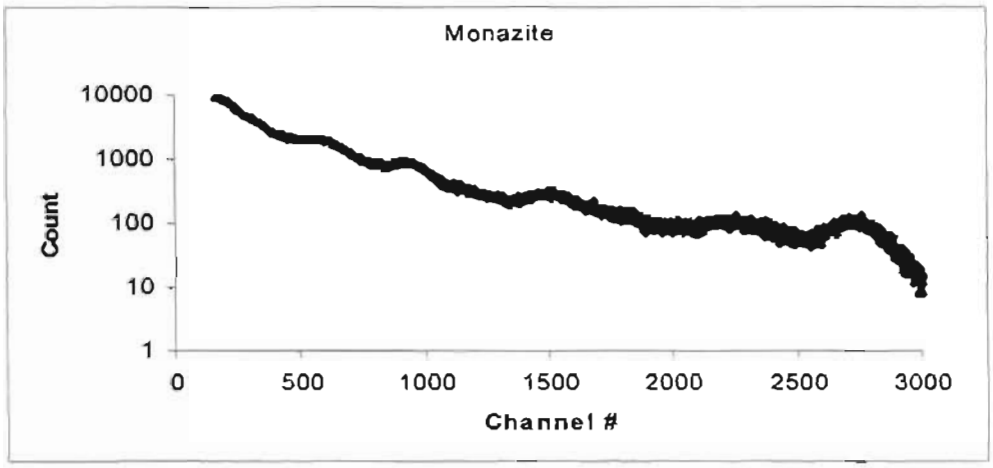

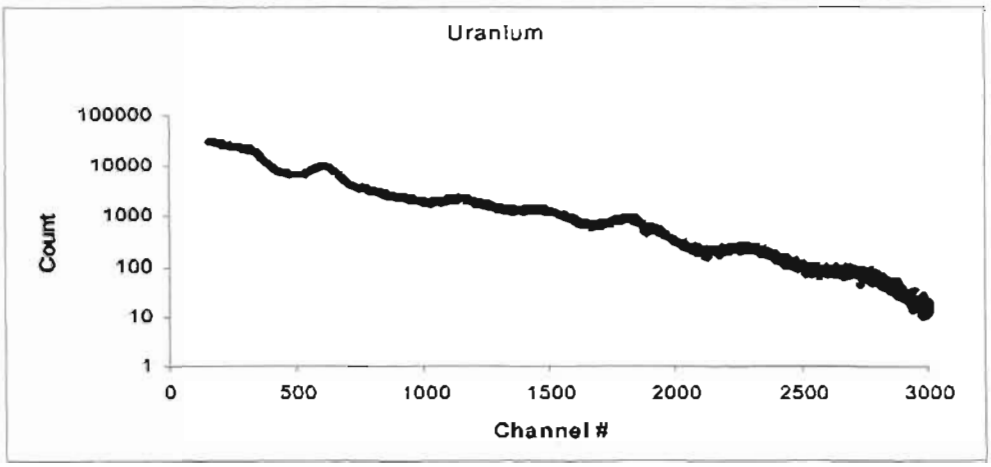

Appendix II Profiles and data tables for 10mm slit measurements.

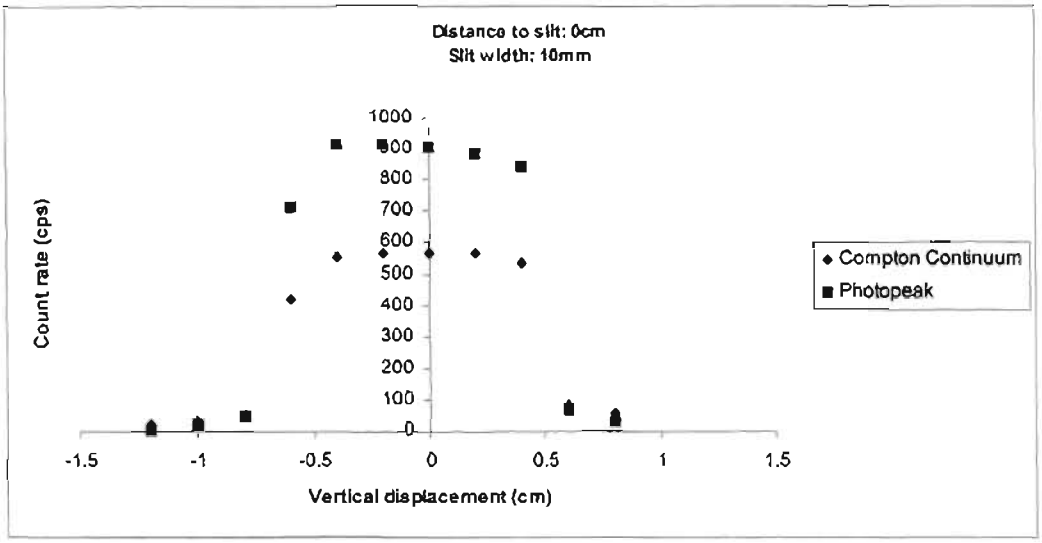

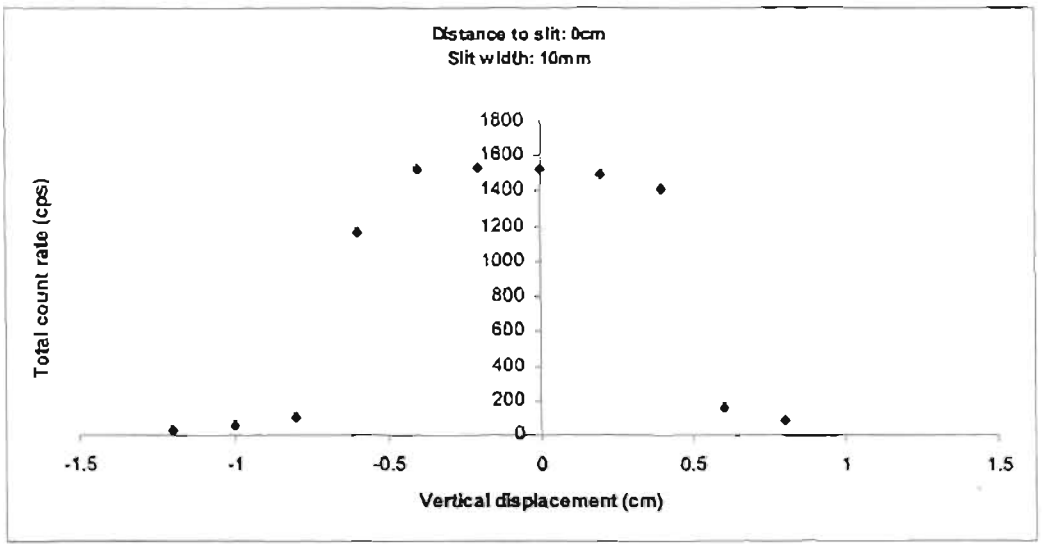

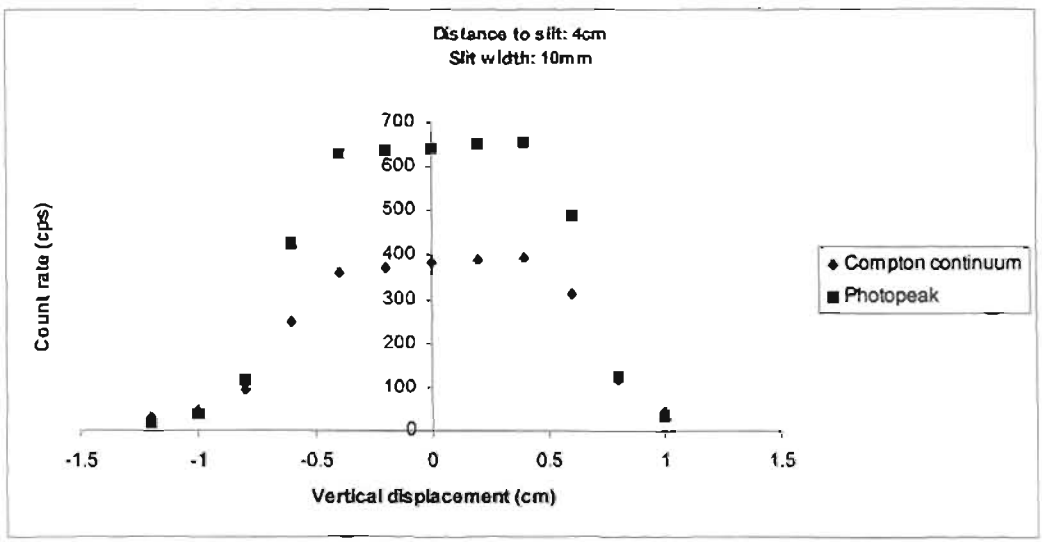

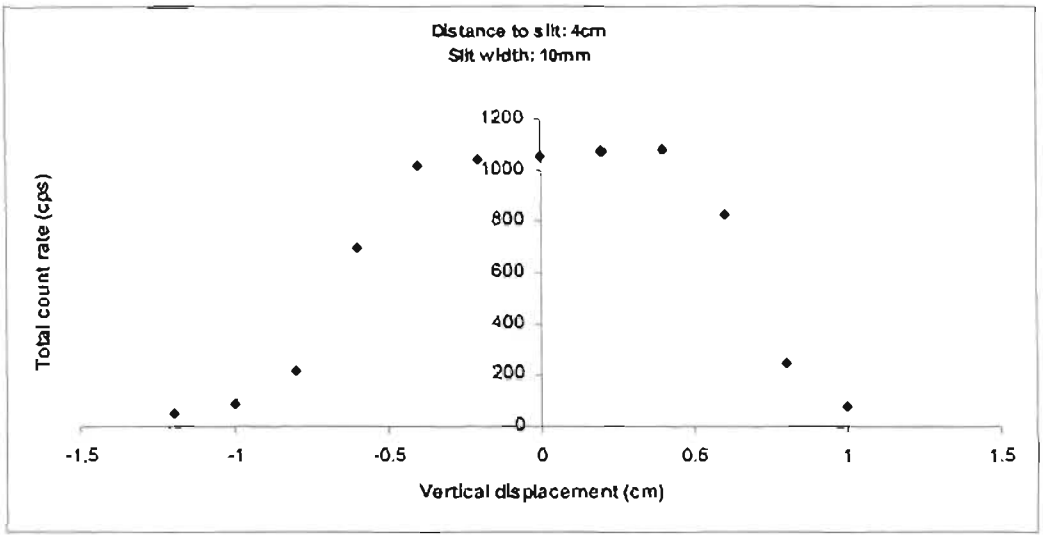
Distance to slit: 4cm
Slit width: 10mm
Total count rate (cps)
1200
1000
800
600
400
200
0
-1.5
-1
-0.5
0
0.5
1
1.5
Vertical displacement (cm)

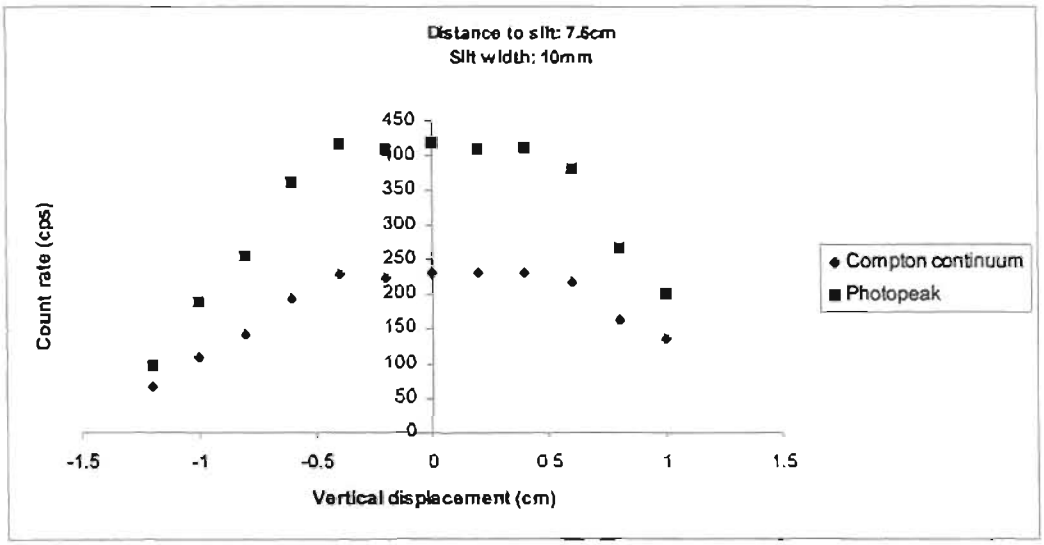
Distance to slit: 7.5cm
Slit width: 10mm
Count rate (cps)
450
400
350
300
250
200
150
100
50
0
-1.5
-1
-0.5
0
0.5
1
1.5
Vertical displacement (cm)
Compton continuum
Photopeak

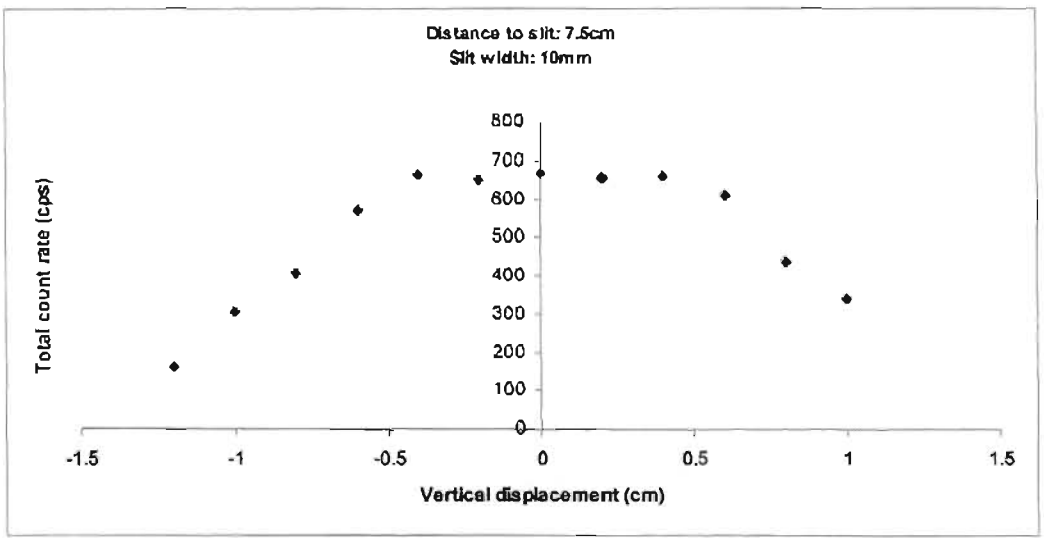
Distance to slit: 7.5cm
Slit width: 10mm
Total count rate (cps)
800
700
600
500
400
300
200
100
0
-1.5
-1
-0.5
0
0.5
1
1.5
Vertical displacement (cm)

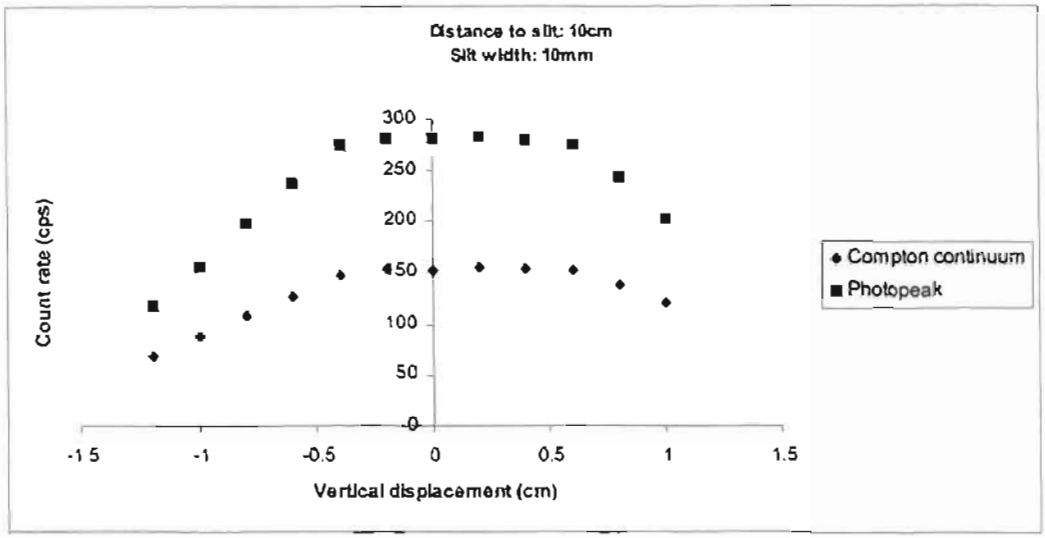
Distance to slit: 10cm
Slit width: 10mm
Count rate (cps)
300
250
200
150
100
50
0
-1.5
-1
-0.5
0
0.5
1
1.5
Vertical displacement (cm)
Compton continuum
Photopeak

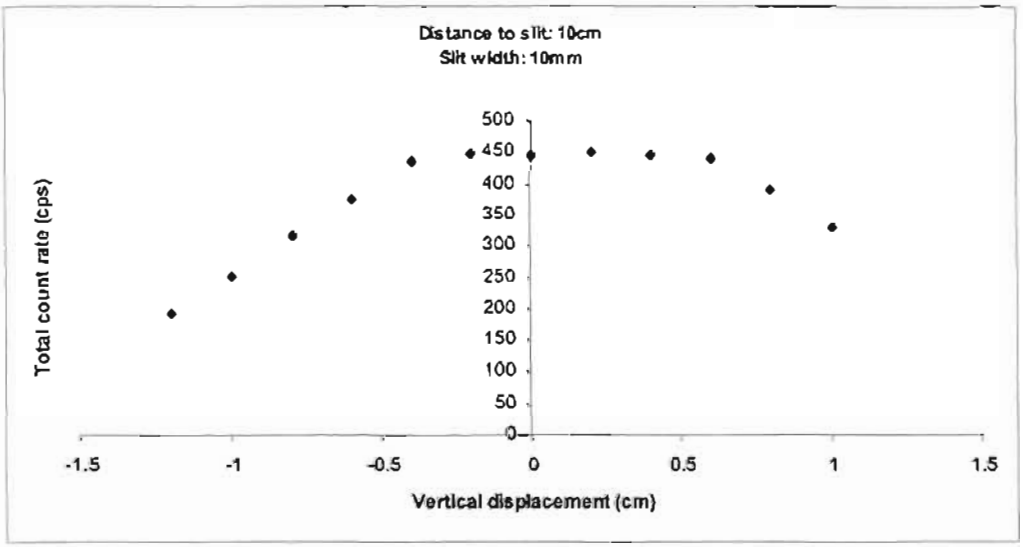
Distance to slit: 10cm
Slit width: 10mm
Total count rate (cps)
500
450
400
350
300
250
200
150
100
50
0
-1.5
-1
-0.5
0
0.5
1
1.5
Vertical displacement (cm)

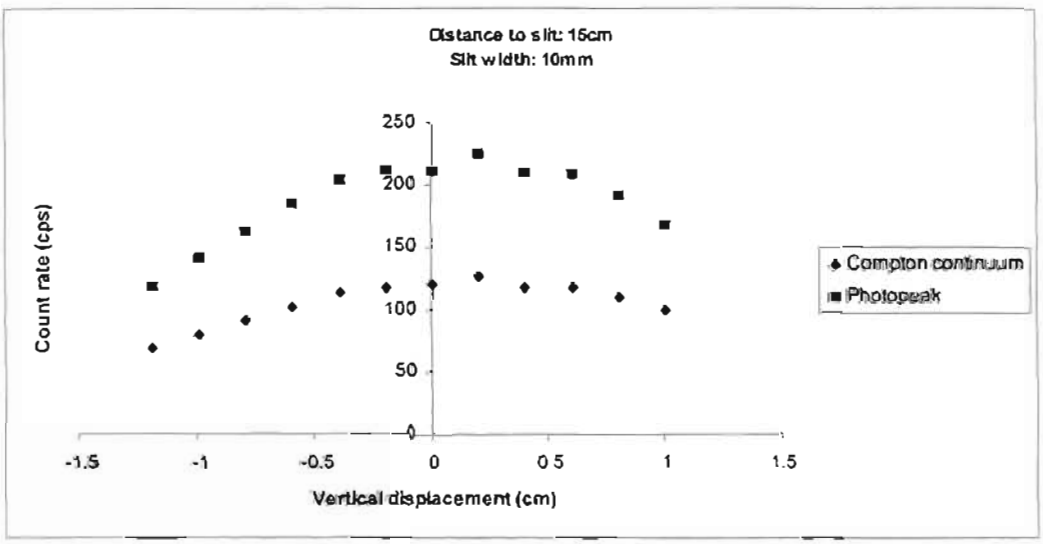
Distance to slit: 15cm
Slit width: 10mm
Count rate (cps)
250
200
150
100
50
0
-1.5
-1
-0.5
0
0.5
1
1.5
Vertical displacement (cm)
Compton continuum
Photopeak

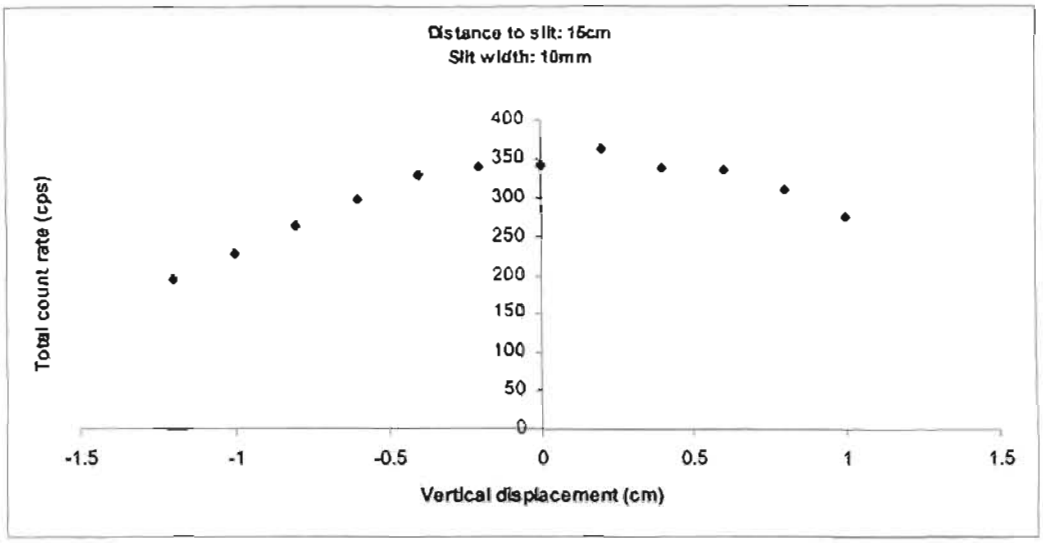

II-1: Distance to slit = 0cm; Slit width = 10mm

Vert. Pos.(cm)	Count rate per E window (cps) Comp. Cont.	Photopeak	N
-1.2	19 ± 5	8 ± 3	27 ± 6
-1	33 ± 6	20 ± 5	54 ± 8
-0.8	55 ± 8	46 ± 7	102 ± 11
-0.6	420 ± 20	710 ± 30	1170 ± 30
-0.4	550 ± 20	920 ± 30	1530 ± 40
-0.2	570 ± 20	910 ± 30	1530 ± 40
0	570 ± 20	910 ± 30	1530 ± 40
0.2	560 ± 20	890 ± 30	1500 ± 40
0.4	530 ± 20	840 ± 30	1420 ± 40
0.6	86 ± 10	70 ± 8	156 ± 13
0.8	56 ± 8	32 ± 6	87 ± 6

II-2: Distance to slit = 4cm; Slit width = 10mm

Vert. Pos.(cm)	Count rate per E window Comp. Cont.	Photopeak	N
-1.2	31 ± 6	19 ± 5	51 ± 8
-1	47 ± 7	39 ± 6	87 ± 10
-0.8	96 ± 10	116 ± 11	216 ± 15
-0.6	249 ± 16	430 ± 20	700 ± 30
-0.4	359 ± 19	630 ± 30	1020 ± 30
-0.2	372 ± 19	640 ± 30	1040 ± 30
0	380 ± 20	640 ± 30	1060 ± 30
0.2	390 ± 20	650 ± 30	1080 ± 30
0.4	390 ± 20	660 ± 30	1080 ± 30
0.6	314 ± 18	490 ± 20	830 ± 30
0.8	119 ± 11	127 ± 11	248 ± 16
1	46 ± 7	33 ± 6	79 ± 9

II-3: Distance to slit = 7.5cm; Slit width = 10mm

Vert. Pos.(cm)	Count rate per E window Comp. Cont.	Photopeak	N
-1.2	65 ± 8	97 ± 10	166 ± 13
-1	109 ± 11	188 ± 14	305 ± 18
-0.8	141 ± 12	254 ± 16	400 ± 20
-0.6	194 ± 14	362 ± 19	570 ± 20
-0.4	228 ± 15	420 ± 20	670 ± 30
-0.2	224 ± 15	410 ± 20	650 ± 30
0	231 ± 15	420 ± 20	670 ± 30
0.2	230 ± 15	410 ± 20	660 ± 30
0.4	231 ± 15	410 ± 20	660 ± 30
0.6	216 ± 15	380 ± 20	610 ± 30
0.8	163 ± 13	267 ± 16	440 ± 20
1	135 ± 12	201 ± 14	342 ± 19

II-4: Distance to slit = 10cm; Slit width = 10mm

Vert. Pos.(cm)	Count rate per E window Comp. Cont.	Photopeak	N
-1.2	68 ± 9	117 ± 11	192 ± 14
-1	87 ± 10	155 ± 13	250 ± 16
-0.8	107 ± 11	197 ± 14	315 ± 18
-0.6	127 ± 12	236 ± 15	380 ± 20
-0.4	147 ± 12	274 ± 17	440 ± 20
-0.2	153 ± 13	281 ± 17	450 ± 20
0	152 ± 13	281 ± 17	450 ± 20
0.2	154 ± 13	283 ± 17	450 ± 20
0.4	153 ± 13	279 ± 17	450 ± 20
0.6	152 ± 13	275 ± 17	440 ± 20
0.8	138 ± 12	244 ± 16	400 ± 20
1	119 ± 11	202 ± 14	329 ± 18

II-5: Distance to slit = 15cm; Slit width = 10mm

Vert. Pos.(cm)	Count rate per E window Comp. Cont.	Photopeak	N
-1.2	69 ± 9	118 ± 11	194 ± 14
-1	80 ± 9	141 ± 12	229 ± 15
-0.8	92 ± 10	162 ± 13	264 ± 17
-0.6	103 ± 10	184 ± 14	297 ± 18
-0.4	115 ± 11	204 ± 14	329 ± 19
-0.2	117 ± 11	212 ± 15	339 ± 19
0	120 ± 11	211 ± 15	342 ± 19
0.2	127 ± 12	225 ± 15	362 ± 19
0.4	118 ± 11	210 ± 15	337 ± 19
0.6	118 ± 11	208 ± 14	335 ± 19
0.8	110 ± 11	192 ± 14	310 ± 18
1	100 ± 10	167 ± 13	274 ± 17

Appendix III Profiles and data tables for 6mm slit measurements.

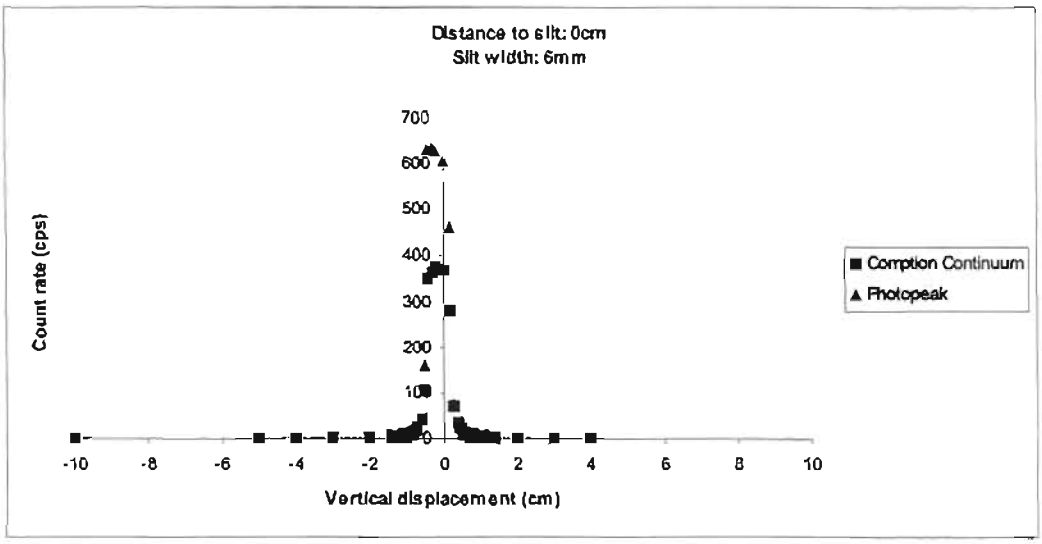

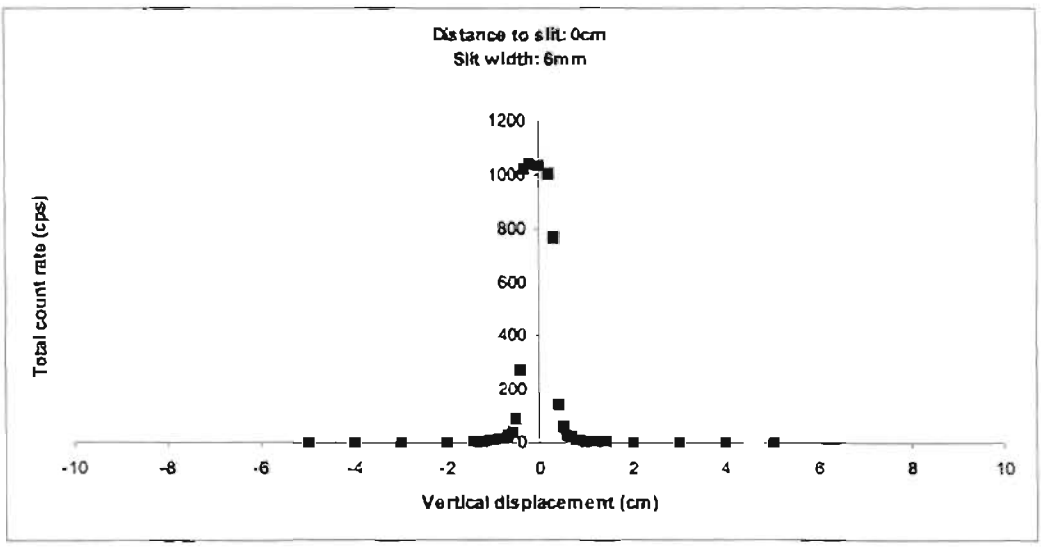

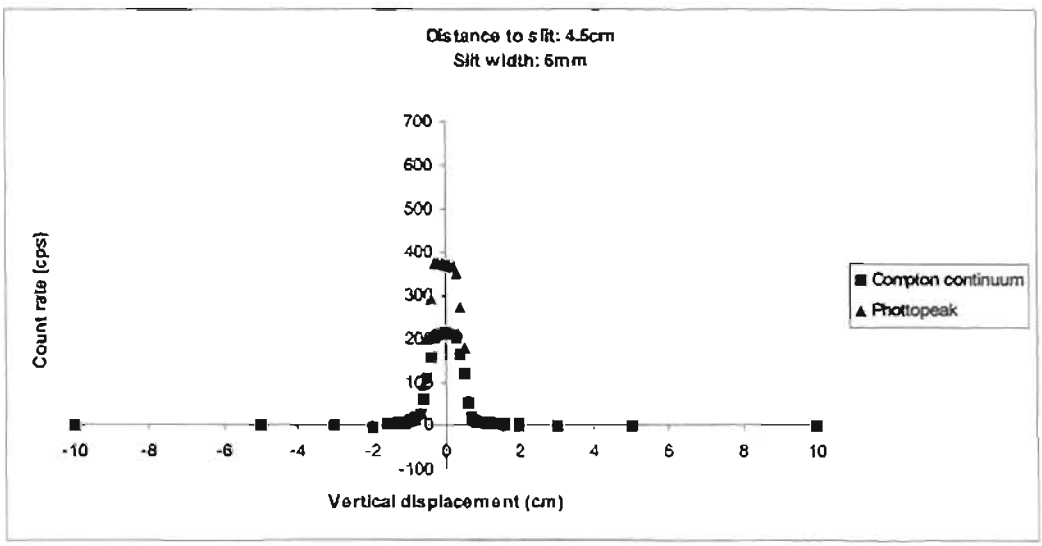

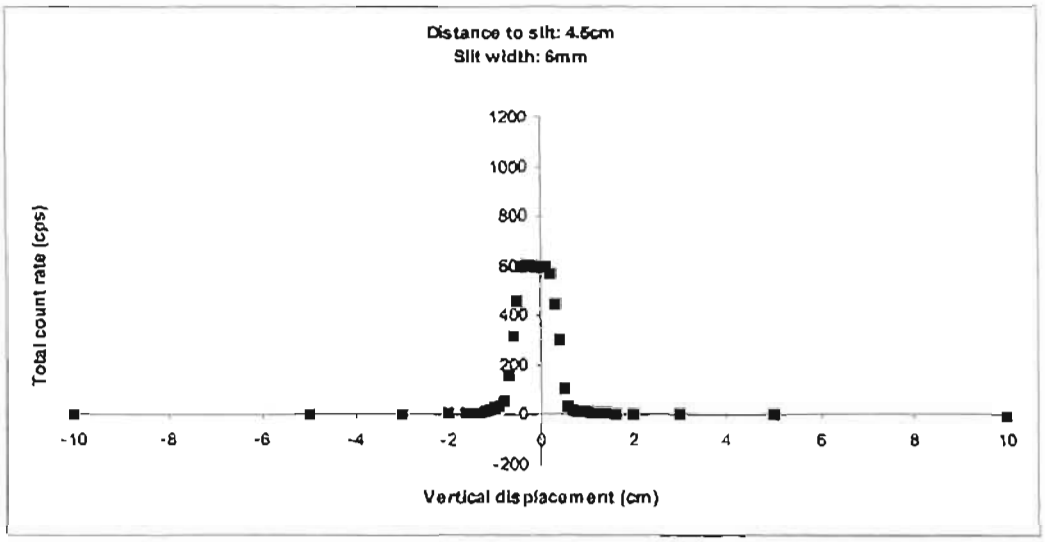
Distance to slit: 4.5cm
Slit width: 6mm
Total count rate (cps)
1200
1000
800
600
400
200
0
-200
-10
-8
-6
-4
-2
0
2
4
6
8
10
Vertical displacement (cm)

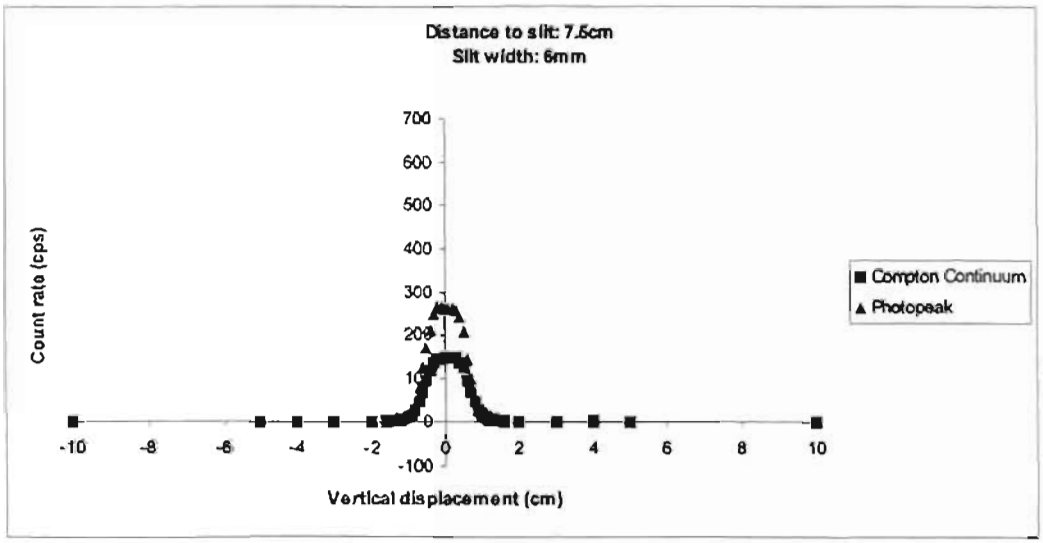
Distance to slit: 7.5cm
Slit width: 6mm
Count rate (cps)
700
600
500
400
300
200
100
0
-100
-10
-8
-6
-4
-2
0
2
4
6
8
10
Vertical displacement (cm)
Compton Continuum
Photopeak

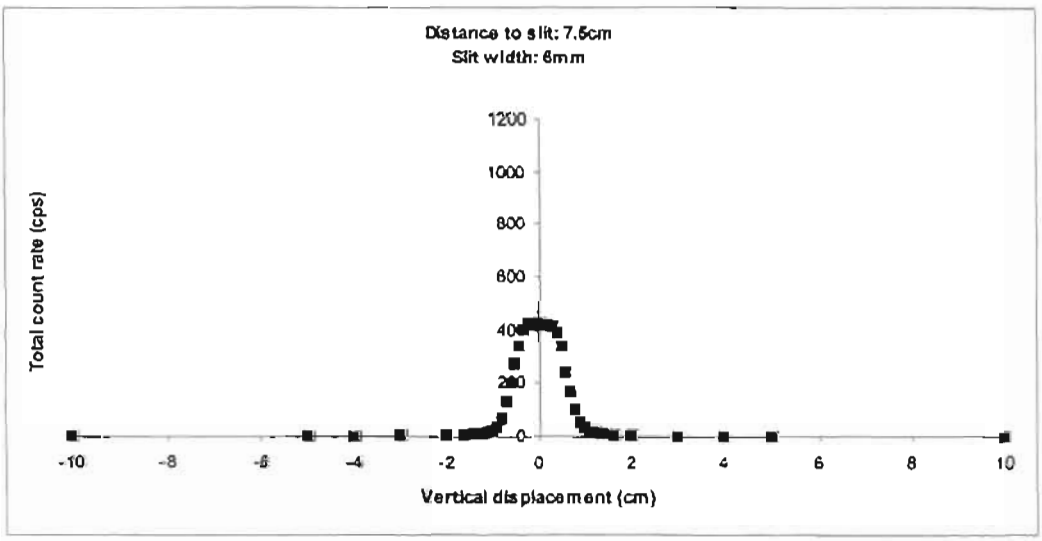
Distance to slit: 7.5cm
Slit width: 6mm
Total count rate (cps)
1200
1000
800
600
400
200
0
-10
-8
-6
-4
-2
0
2
4
6
8
10
Vertical displacement (cm)

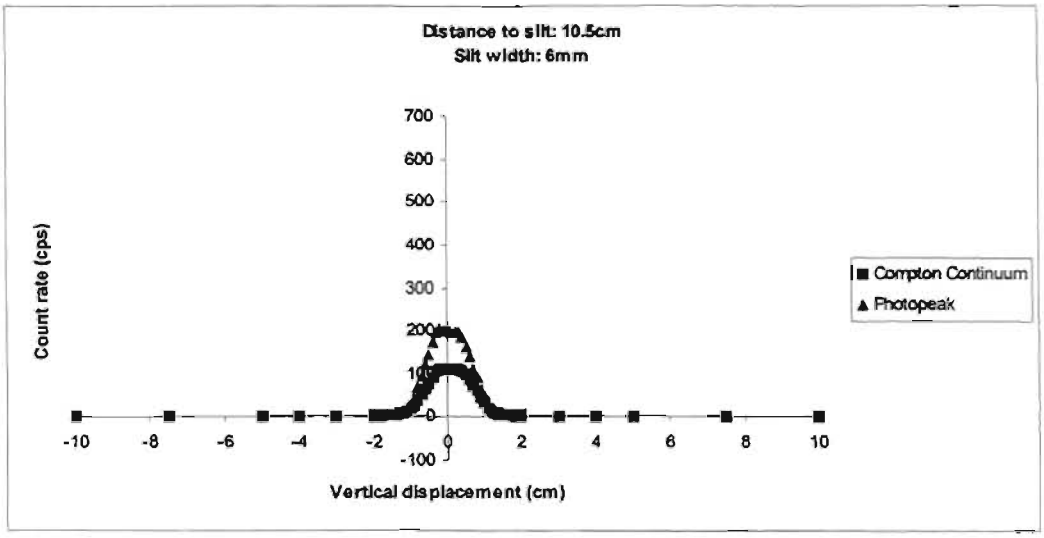
Distance to slit: 10.5cm
Slit width: 6mm
Count rate (cps)
700
600
500
400
300
200
100
0
-100
-10
-8
-6
-4
-2
0
2
4
6
8
10
Vertical displacement (cm)
Compton Continuum
Photopeak

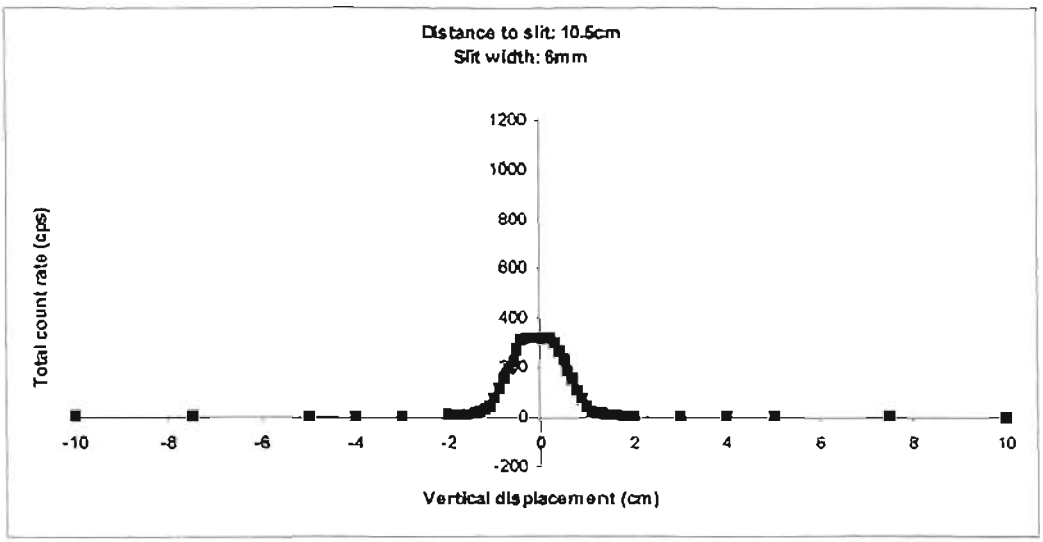
Distance to slit: 10.5cm
Slit width: 6mm
Total count rate (cps)
1200
1000
800
600
400
0
-200
-10
-8
-6
-4
-2
0
2
4
6
8
10
Vertical displacement (cm)

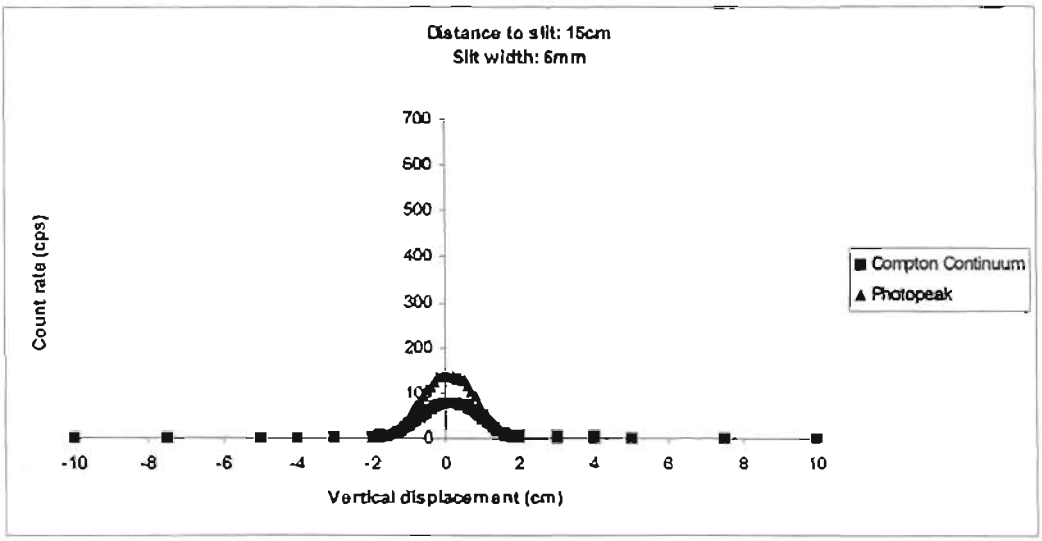
Distance to slit: 15cm
Slit width: 6mm
Count rate (cps)
700
600
500
400
300
200
0
-10
-8
-6
-4
-2
0
2
4
6
8
10
Vertical displacement (cm)
Compton Continuum
Photopeak

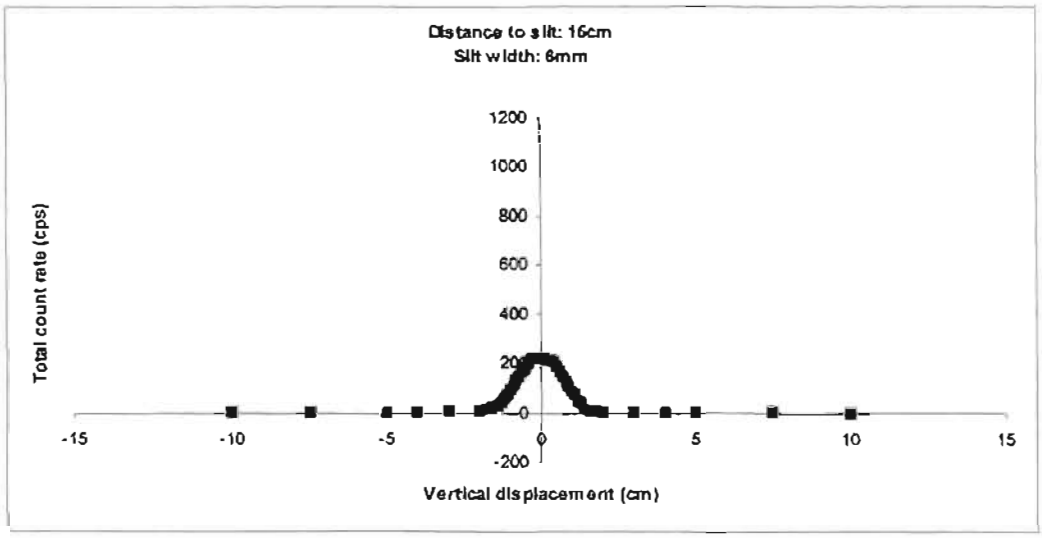

III-1: Distance to slit = 0cm; Slit width = 6mm

Vert. Disp. (cm)	Comp. Cont.	Photopeak	N (cps)	Vert. Disp. (cm)	Comp. Cont.	Photopeak	N (cps)
-5	0.4 ± 2.0	0.0 ± 0.9	1 ± 3	0.2	369 ± 19	608 ± 30	1000 ± 30
-4	0.5 ± 2.0	0.0 ± 0.9	0 ± 3	0.3	280 ± 17	460 ± 20	770 ± 30
-3	0.9 ± 2.0	0.1 ± 1.0	1 ± 3	0.4	71 ± 9	74 ± 7	150 ± 20
-2	2 ± 3	0.4 ± 1.1	3 ± 3	0.5	35 ± 6	24 ± 5	60 ± 8
-1.4	5 ± 3	1.2 ± 1.4	6 ± 4	0.6	21 ± 5	9 ± 3	30 ± 6
-1.2	7 ± 3	1.9 ± 1.6	9 ± 4	0.7	16 ± 5	6 ± 3	22 ± 5
-1.1	8 ± 3	2.5 ± 1.8	10 ± 4	0.8	11 ± 4	3.5 ± 2.0	15 ± 5
-1	10 ± 4	3.4 ± 2.0	13 ± 5	0.9	9 ± 4	2.7 ± 1.9	12 ± 4
-0.9	11 ± 4	4.4 ± 2.0	15 ± 5	1	7 ± 4	1.6 ± 1.6	9 ± 4
-0.8	14 ± 4	6 ± 3	20 ± 5	1.1	7 ± 3	1.5 ± 1.5	8 ± 4
-0.7	17 ± 5	10 ± 3	28 ± 6	1.2	5 ± 3	1.2 ± 1.4	7 ± 4
-0.6	24 ± 5	17 ± 4	42 ± 7	1.4	4 ± 3	0.8 ± 1.3	5 ± 4
-0.5	44 ± 7	44 ± 7	89 ± 10	2	2 ± 3	0.2 ± 1.0	2 ± 3
-0.4	106 ± 11	159 ± 13	272 ± 17	3	0.8 ± 2.0	0.1 ± 1.0	1 ± 3
-0.3	353 ± 19	632 ± 30	1020 ± 30	4	0.4 ± 2.0	0.0 ± 1.0	0 ± 3
-0.2	366 ± 19	638 ± 30	1040 ± 30	5	0.2 ± 2.0	0.0 ± 1.0	0 ± 3
0	376 ± 20	628 ± 30	1040 ± 30				

III-2: Distance to slit = 4.5cm; Slit width = 6mm

Vert. Disp. (cm)	Comp. Cont.	Photopeak	N (cps)	Vert. Disp. (cm)	Comp. Cont.	Photopeak	N (cps)
-10	0 ± 2	0.1 ± 1.0	1 ± 3	0.1	211 ± 15	370 ± 19	600 ± 30
-5	1 ± 2	0.1 ± 1.0	3 ± 3	0.2	212 ± 15	368 ± 19	570 ± 30
-3	2 ± 3	0.6 ± 1.2	6 ± 3	0.3	204 ± 15	351 ± 19	450 ± 20
-2	-2 ± 2	1.8 ± 1.6	8 ± 4	0.4	167 ± 13	273 ± 17	300 ± 20
-1.6	5 ± 3	2.8 ± 1.9	10 ± 4	0.5	120 ± 11	179 ± 13	110 ± 18
-1.4	6 ± 3	4 ± 2	10 ± 4	0.6	52 ± 8	57 ± 8	33 ± 11
-1.3	7 ± 3	4 ± 2	12 ± 4	0.7	18 ± 5	14 ± 4	21 ± 6
-1.2	8 ± 4	4 ± 2	15 ± 5	0.8	13 ± 4	9 ± 3	17 ± 5
-1.1	9 ± 4	6 ± 3	20 ± 5	0.9	10 ± 4	7 ± 3	17 ± 5
-1	11 ± 4	9 ± 3	26 ± 5	1	10 ± 4	7 ± 3	14 ± 5
-0.9	14 ± 4	12 ± 4	36 ± 6	1.1	9 ± 4	5.0 ± 2.0	12 ± 5
-0.8	18 ± 5	17 ± 4	58 ± 7	1.2	7 ± 4	4.4 ± 2.0	10 ± 4
-0.7	27 ± 6	30 ± 6	160 ± 8	1.3	6 ± 3	3.4 ± 2.0	9 ± 4
-0.6	60 ± 8	95 ± 10	319 ± 13	1.4	6 ± 3	2.9 ± 1.9	7 ± 4
-0.5	111 ± 11	200 ± 14	463 ± 18	1.6	5 ± 3	2.5 ± 1.8	4 ± 4
-0.4	157 ± 13	291 ± 17	600 ± 20	2	4 ± 3	1.4 ± 1.5	2 ± 3
-0.3	203 ± 14	374 ± 19	600 ± 25	3	2 ± 3	0.5 ± 1.2	1 ± 3
-0.2	209 ± 15	376 ± 19	600 ± 30	5	1 ± 2	0.1 ± 1.0	0 ± 3
-0.1	211 ± 15	374 ± 19	600 ± 30	10	0 ± 2	-0.0 ± 0.9	-4 ± 3
0	213 ± 15	370 ± 19	600 ± 30				

III-3: Distance to slit = 7.5cm; Slit width = 6mm

Vert. Disp. (cm)	Comp. Cont.	Photopeak	N (cps)	Vert. disp. (cm)	Comp. Cont.	Photopeak	N (cps)
-10	0.6 ± 2.0	-0.01 ± 0.9	1 ± 3	0.1	148 ± 12	262 ± 16	430 ± 20
-5	1 ± 3	0.3 ± 1.1	2 ± 3	0.2	149 ± 12	260 ± 16	420 ± 20
-4	2 ± 3	0.6 ± 1.2	2 ± 3	0.3	147 ± 12	256 ± 16	420 ± 20
-3	2 ± 3	1.0 ± 1.4	3 ± 3	0.4	138 ± 12	240 ± 16	390 ± 20
-2	1 ± 3	2.1 ± 1.7	6 ± 4	0.5	125 ± 11	208 ± 15	343 ± 19
-1.6	5 ± 3	3.1 ± 2.0	8 ± 4	0.6	94 ± 10	143 ± 12	244 ± 16
-1.4	6 ± 3	4.2 ± 2.0	10 ± 4	0.7	70 ± 9	100 ± 10	174 ± 14
-1.3	7 ± 3	5 ± 3	12 ± 5	0.8	45 ± 7	55 ± 8	103 ± 11
-1.2	8 ± 4	6 ± 3	15 ± 5	0.9	28 ± 6	28 ± 5	56 ± 8
-1.1	11 ± 4	10 ± 3	20 ± 5	1	19 ± 5	17 ± 4	36 ± 7
-1	13 ± 4	13 ± 4	27 ± 6	1.1	12 ± 4	9 ± 3	21 ± 5
-0.9	17 ± 5	20 ± 5	38 ± 7	1.2	9 ± 4	7 ± 3	16 ± 5
-0.8	28 ± 6	38 ± 6	69 ± 9	1.3	8 ± 4	5 ± 3	13 ± 5
-0.7	48 ± 7	80 ± 9	134 ± 12	1.4	6 ± 3	4 ± 2	11 ± 4
-0.6	69 ± 9	125 ± 11	203 ± 15	1.6	5 ± 3	3 ± 2	8 ± 4
-0.5	94 ± 10	170 ± 13	276 ± 17	2	3 ± 3	2 ± 2	5 ± 4
-0.4	116 ± 11	213 ± 15	344 ± 19	3	2 ± 3	0.9 ± 1.3	3 ± 3
-0.3	137 ± 12	250 ± 16	400 ± 20	4	4 ± 3	0.4 ± 1.1	2 ± 3
-0.2	146 ± 12	263 ± 16	430 ± 20	5	1 ± 3	0.3 ± 1.1	1 ± 3
-0.1	145.3 ± 12	263 ± 16	430 ± 20	10	0.3 ± 2.0	0.0 ± 0.9	0 ± 3
0	147.7 ± 12	261 ± 16	430 ± 20				

III-4: Distance to slit = 10.5cm; Slit width = 6mm

Vert. Disp. (cm)	Comp. Cont.	Photopeak	N (cps)	Vert. Disp. (cm)	Comp. Cont.	Photopeak	N (cps)
-10	0.7 ± 2.0	-0.0 ± 0.9	1 ± 3	0.1	111 ± 11	198 ± 14	318 ± 18
-7.5	0.9 ± 2.0	0.2 ± 1.0	2 ± 3	0.2	112 ± 11	198 ± 14	316 ± 18
-5	1 ± 3	0.3 ± 1.1	2 ± 3	0.3	112 ± 11	195 ± 14	301 ± 18
-4	2 ± 3	0.8 ± 1.3	3 ± 3	0.4	107 ± 11	186 ± 14	268 ± 18
-3	2 ± 3	1.0 ± 1.4	6 ± 3	0.5	98 ± 10	165 ± 13	234 ± 17
-2	4 ± 3	2.2 ± 1.8	7 ± 4	0.6	87 ± 10	142 ± 12	187 ± 16
-1.8	4 ± 3	3 ± 2.0	9 ± 4	0.7	71 ± 9	112 ± 11	155 ± 14
-1.6	5 ± 3	4 ± 2.0	13 ± 4	0.8	62 ± 8	90 ± 10	111 ± 13
-1.4	7 ± 4	6 ± 3	17 ± 5	0.9	46 ± 7	63 ± 8	76 ± 11
-1.3	9 ± 4	8 ± 3	21 ± 5	1	34 ± 6	42 ± 7	41 ± 9
-1.2	10 ± 4	11 ± 3	31 ± 5	1.1	20 ± 5	20 ± 5	27 ± 7
-1.1	14 ± 5	16 ± 4	46 ± 6	1.2	14 ± 4	12 ± 4	19 ± 6
-1	19 ± 6	25 ± 5	74 ± 7	1.3	11 ± 4	8 ± 3	14 ± 5
-0.9	28 ± 7	44 ± 7	113 ± 9	1.4	8 ± 4	6 ± 3	9 ± 5
-0.8	40 ± 8	70 ± 8	153 ± 11	1.6	5 ± 3	4 ± 2	7 ± 4
-0.7	53 ± 8	95 ± 10	194 ± 13	1.8	4 ± 3	3.0 ± 2.0	6 ± 4
-0.6	66 ± 9	122 ± 11	229 ± 14	2	4 ± 3	2.3 ± 1.8	3 ± 4
-0.5	78 ± 10	144 ± 12	274 ± 15	3	2 ± 3	1.0 ± 1.4	2 ± 3
-0.4	93 ± 11	173 ± 13	312 ± 17	4	1 ± 3	0.8 ± 1.3	1 ± 3
-0.3	106 ± 11	197 ± 14	322 ± 18	5	1 ± 2	0.4 ± 1.1	1 ± 3
-0.2	110 ± 11	203 ± 14	321 ± 18	7.5	1 ± 2	0.1 ± 1.0	1 ± 3
-0.1	112 ± 11	200 ± 14	320 ± 18	10	1 ± 2	0.0 ± 0.9	-4 ± 3
0	112 ± 11	200 ± 14	317 ± 18				

III-5: Distance to slit = 15cm; Slit width = 6mm

Vert. Disp. (cm)	Comp. Cont.	Photopeak	N (cps)	Vert. Disp. (cm)	Comp. Cont.	Photopeak	N (cps)
-10	0.5 ± 2.0	0.0 ± 0.9	1 ± 3	0.1	77 ± 9	136 ± 12	220 ± 15
-7.5	0.7 ± 2.0	0.3 ± 1.1	2 ± 3	0.2	78 ± 9	135 ± 12	216 ± 15
-5	1 ± 3	0.4 ± 1.1	2 ± 3	0.3	77 ± 9	133 ± 12	215 ± 15
-4	2 ± 3	0.7 ± 1.2	4 ± 3	0.4	76 ± 9	133 ± 12	207 ± 15
-3	2 ± 3	1.0 ± 1.4	8 ± 3	0.5	74 ± 9	127 ± 11	191 ± 15
-2	5 ± 3	3.0 ± 2.0	10 ± 4	0.6	69 ± 9	116 ± 11	171 ± 14
-1.8	6 ± 3	4 ± 2	14 ± 4	0.7	62 ± 8	105 ± 10	151 ± 13
-1.6	7 ± 4	6 ± 3	23 ± 5	0.8	57 ± 8	91 ± 10	126 ± 13
-1.4	11 ± 4	11 ± 4	29 ± 6	0.9	49 ± 7	75 ± 9	108 ± 12
-1.3	13 ± 4	15 ± 4	42 ± 6	1	42 ± 7	63 ± 8	91 ± 11
-1.2	18 ± 5	24 ± 5	62 ± 7	1.1	37 ± 7	53 ± 7	73 ± 10
-1.1	24 ± 5	37 ± 6	78 ± 8	1.2	31 ± 6	40 ± 6	52 ± 9
-1	28 ± 6	47 ± 7	97 ± 9	1.3	24 ± 5	28 ± 5	40 ± 8
-0.9	34 ± 6	60 ± 8	114 ± 10	1.4	19 ± 5	20 ± 5	19 ± 7
-0.8	40 ± 7	71 ± 9	132 ± 11	1.6	11 ± 4	8 ± 3	12 ± 5
-0.7	46 ± 7	82 ± 9	151± 12	1.8	8 ± 4	5 ± 2	9 ± 5
-0.6	53 ± 8	93 ± 10	168 ± 13	2	6 ± 3	3.2 ± 2.0	4 ± 4
-0.5	58 ± 8	105 ± 10	182 ± 13	3	3 ± 3	1.3 ± 2.0	3 ± 3
-0.4	64 ± 8	113 ± 11	200 ± 14	4	2 ± 3	0.7 ± 1.3	2 ± 3
-0.3	69 ± 9	125 ± 11	218 ± 14	5	1 ± 3	0.4 ± 1.1	1 ± 3
-0.2	76 ± 9	136 ± 12	219 ± 15	7.5	1 ± 2	0.3 ± 1.1	1 ± 3
-0.1	76 ± 9	136 ± 12	219 ± 15	10	0 ± 2	0.1 ± 1.0	-4 ± 3
0	77 ± 9	135 ± 12	219 ± 15				

III-6: FWHM values of N, Compton continuum and photopeak.

	FWHM (cm)		
Distance (cm)	N (6mm)	Compton Continuum (6mm)	Photopeak (6mm)
0	0.8	0.8	0.7
4.5	1	1	0.9
7.5	1.2	1.3	1.2
10.5	1.5	1.6	1.5
15	1.9	2	1.9

Appendix IV Standard spectra

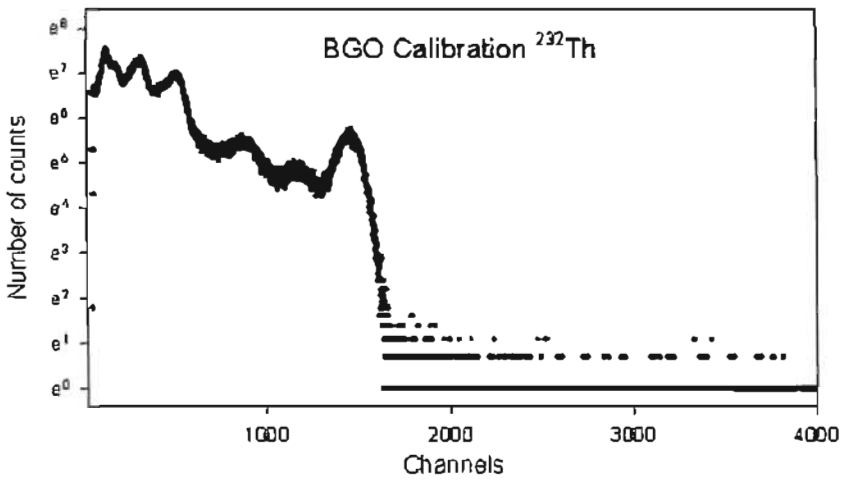

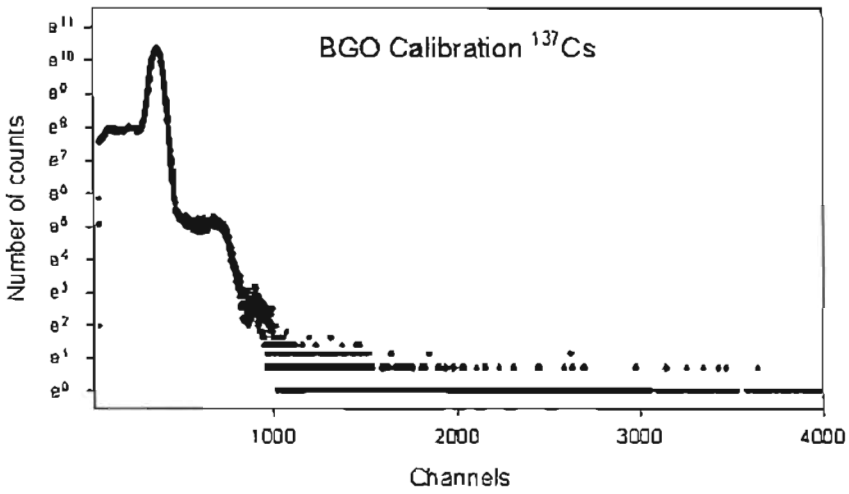

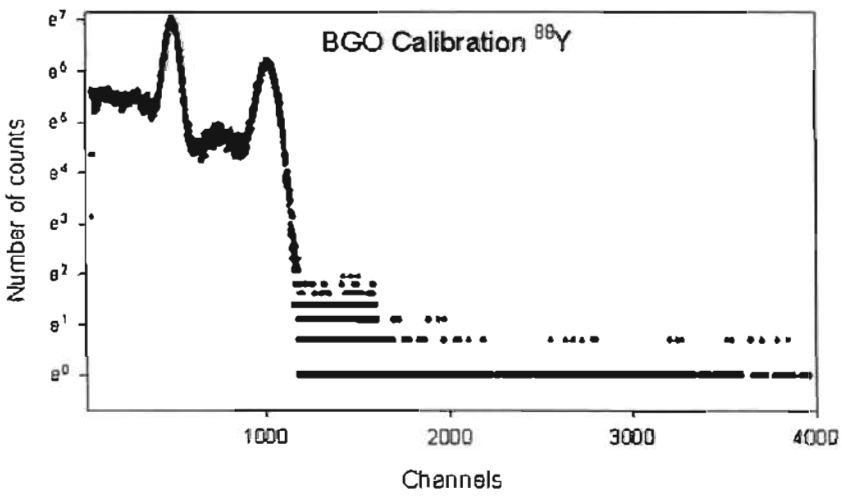

Appendix V Proof of the convolution theorem

Suppose that $g(x) = f(x) \otimes h(x)$. Then, if $\Im\{g(x)\} = G(s)$, $\Im\{f(x)\} = F(s)$ and $\Im\{h(x)\} = H(s)$ where $\Im$ is the operator for the Fourier transform,

$$
\begin{aligned}
G(s) &= \Im\{g(x)\} = \Im\{f(x) \otimes h(x)\} \\
&= \Im\{ \int_{-\infty}^{\infty} f(\beta) h(x-\beta) d\beta \} \\
&= \int_{-\infty}^{\infty} \left[\int_{-\infty}^{\infty} f(\beta) h(x-\beta) d\beta \right] \exp(-i2\pi s x) dx \\
&= \int_{-\infty}^{\infty} f(\beta) \left[\int_{-\infty}^{\infty} h(x-\beta) \exp(-i2sx) dx \right] d\beta \\
&= H(s) \int_{-\infty}^{\infty} f(\beta) \exp(-i2\pi s \beta) d\beta \\
&= F(s) \cdot H(s)
\end{aligned}
$$

Therefore $\Im\{f(x) \otimes h(x)\} = F(s) \cdot H(s)$.

It can be similarly proven that $\Im\{f(x) \cdot h(x)\} = F(s) \otimes H(s)$.

Appendix VI Description of PHAROS Software

PHAROS Main Menu

Figure VI-1 below shows the main menu that the user encounters when executing the PHAROS software. This incorporates several functions (accessed via the command buttons at the top) as well as a Status box where the status of an acquisition run is logged when the system is active.

- **Settings...**

  This brings up the settings screen (seen below in Figure VI-1) where the user can adjust acquisition parameters.

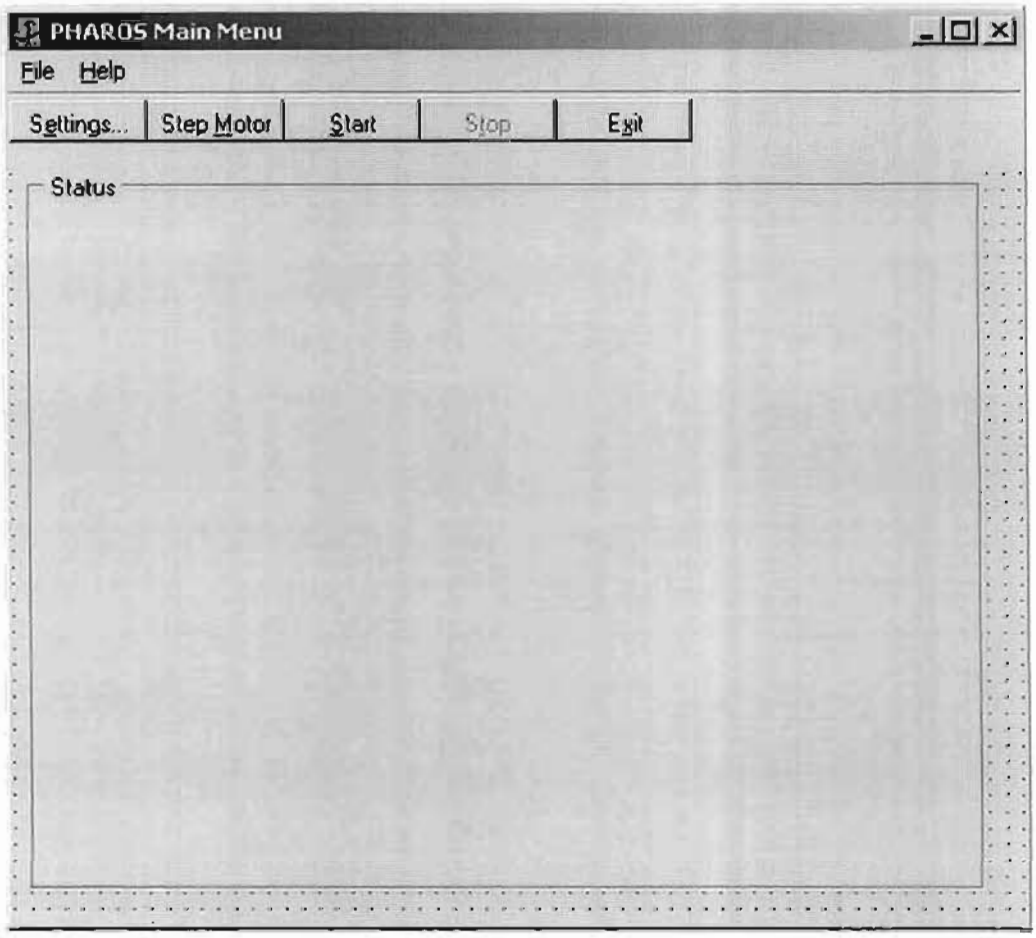

Figure VI-1: This snapshot shows the main menu of the PHAROS software.

- **Step Motor**

  This activates the form used for controlling the stepper motor (Figure 3-3 and gives the user the option of manually controlling the movement if necessary. This is used to calibrate the stepper motor.

- **Start**

  This starts the logging routine. It initiates the loop described above and displays the state of the current run in the Status panel. Once initiated this button becomes disabled and the stop button becomes enabled.

- **Stop**

  This pauses the current data acquisition loop. Note that it does not interrupt the execution of GammaVision, but it will pause once GammaVision returns control. Alternatively, if the user wishes, he/she may terminate GammaVision manually after pausing the program execution.

- **Exit**

  This exits the program. This button is disabled while the system is logging data and the current run must be stopped before exiting the program. Upon exit system variables are saved to the registry, and the current position of the core logged.

Settings Screen

- The core name will by default be given to the .sdf file which is used to store the acquisition data. The "Core Length" (in centimetres) and "Number of Steps" determines the step size (length / steps, also in centimetres) which in turn affects the number of steps made by the stepper motor. The currently recorded position of the core can be set by entering a new value in the field and clicking *"Set Core Position"*.
- *"Save Spectra To..."* sets the path for saving the spectra acquired by GammaVision during acqusition, in addition to the .sdf created by the PHAROS software. Note that the GammaVision software actually saves files to a path specified in the Job File it uses. The PHAROS software then picks up these spectra and copies them to the desired location.

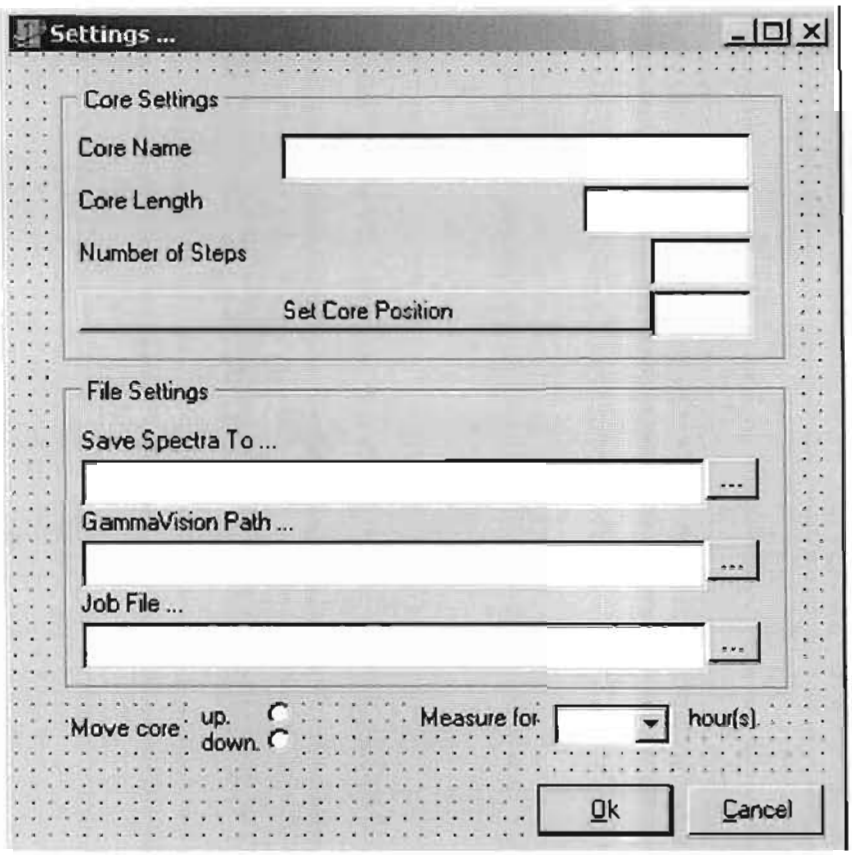

Figure VI-2: Screenshot of the settings menu.

- *"GammaVision Path..."* sets the location of the gv32.exe executable file needed to execute the GammaVision software.
- *"Job File..."* sets the location of the GammaVision batch file (or job file) that is passed as a parameter to the GammaVision software when the program is spawned. This batch file contains some of the acquisition parameters (such as measuring time of a single step, etc).
- The user can also set the direction of motion of the core, choosing to either measure it while lifting the core, or measure while lowering by selecting the "Move core" option.
- The software can be set to measure for a specified time limit. The measurement time can be optionally manually selected instead of automatically. In current versions of the software this automatic determination of the period is not yet implemented. Setting the time limit still needs to be done manually by changing the parameters in the specified Job File.

- **Ok**

  This accepts the current values of the parameters, saves them to the windows registry and closes this window.

- **Cancel**

  Closes the form and loses all changes that are made. No data is saved to the registry when this action is performed.

The Stepper Motor Screen

Figure VI-3 displays the screen the user sees when setting up the stepper motor. Here the user can set variables and also control the motor manually if required.

- Stepper Motor Settings

  These settings refer to the internal settings on the NI-DAQ PC card that interfaces to the stepper motor. They determine the timing of the output signals that drive the motor and set the speed at which the motor will turn. Users are advised not to change these settings from their default.

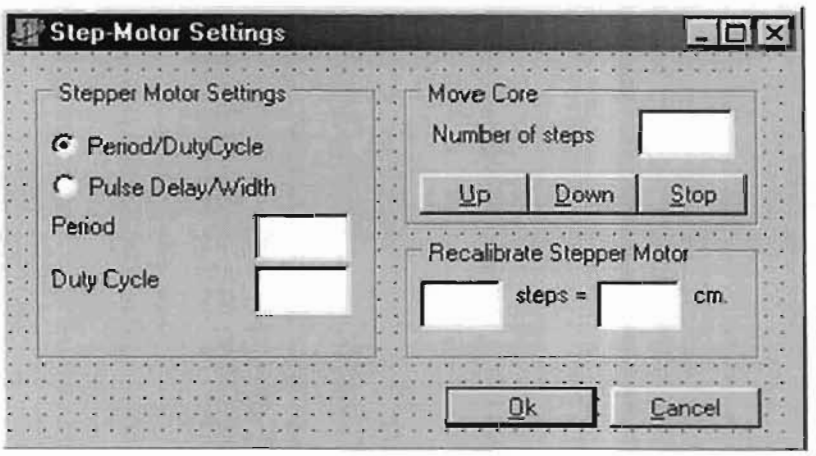

Figure VI-3: Layout of the screen used to control the Stepper Motor.

- Move Core

  This panel holds the controls needed for moving the core manually. The user must enter the required number of steps to move and then press the button corresponding to the required direction of movement. Note that the steps referred to on this form should not be confused with the number of steps when measuring the core. Here a step refers to a single step of the motor, whilst a

core-step refers to the movement of the core by a predefined incremental distance.

- Recalibrate Stepper Motor

  Here the user can set the distance the core travels for a specified number of steps.

- **Ok**

  If the user has entered all the data correctly, this will save the new settings and close the form, returning control to the main program.

- **Cancel**

  This just closes the form and discards all changes the user has made.